



TECHNISCHE
UNIVERSITÄT
WIEN

Diploma Thesis

Electric Arc Furnace Process Modelling and Simulation

Submitted in satisfaction of the requirements for the degree of
Diplom-Ingenieur (Dipl.-Ing. or DI)

at the Faculty of Technical Chemistry TU Wien,
Institute of Chemical, Environmental and Bioscience Engineering

under the supervision of

Ao.Univ.Prof. Dipl.-Ing. Dr.techn. **Michael Harasek**
Assistant Prof. Dipl.-Ing. Dr.techn. **Walter Wukovits**

and

Dipl.-Ing. Dr.techn. **Bernd Weiss**

by

Hermann Völkl, BSc

Vienna, _____

Signature _____



TECHNISCHE
UNIVERSITÄT
WIEN

DIPLOMARBEIT

Modellierung und Prozesssimulation des Elektrolichtbogenofens (EAF)

Ausgeführt am Institut für
Verfahrenstechnik, Umwelttechnik und technische Biowissenschaften
der Technischen Universität Wien

unter der Anleitung von
Ao.Univ.Prof. Dipl.-Ing. Dr.techn. **Michael Harasek**
Assistant Prof. Dipl.-Ing. Dr.techn. **Walter Wukovits**

und
Dipl.-Ing. Dr.techn. **Bernd Weiss**

durch

Hermann Völkl, BSc

Wien, am _____

Unterschrift _____

Acknowledgements

I would like to thank my supervisors Prof. Michael Harasek and Dr. Walter Wukovits for their excellent guidance, constant support and help in organization of this research work.

I acknowledge the generous financial support from Primetals Technologies Austria GmbH and want to especially thank Dr. Bernd Weiss for his adept supervision and scientific support in all areas of this thesis.

A special thanks also to Dipl.-Ing. Stefan Tjaden for his help and many valuable suggestions regarding modelling and data analysis.

Appreciation is extended to the EAF specialists and my co-workers from Primetals Technologies Austria GmbH as well as voestalpine AG for providing the needed metallurgical tools and calculations as well as giving me valuable feedback and support.

I would like to express my gratitude to all my colleagues from the research group "Thermal Process Engineering and Simulation" and especially Patrick Moravcic for their help.

Finally, I want to thank my family and partner Edith for their support and continuous encouragement.



Die approbierte gedruckte Originalversion dieser Diplomarbeit ist an der TU Wien Bibliothek verfügbar
The approved original version of this thesis is available in print at TU Wien Bibliothek.

Abstract

Electric Arc Furnace (EAF) steelmaking accounts for about one third of global crude steel production. Compared to iron ore based process routes, steel scrap recycling in the EAF significantly lowers energy consumption and CO₂ emissions. Rising scrap availability and the steel industry's focus on carbon neutrality further increase the EAF's appeal. Despite rapid improvements in the sector over the past decades, there is still a large potential for innovation. Since plant trials are expensive and potentially dangerous, mathematical modelling and process simulation have become widely used engineering tools to better understand and optimise the EAF process.

This thesis covers the revision, expansion and validation of a mathematical EAF process model from the metallurgical model library of Primetals Technologies Austria GmbH. A major task was the development and implementation of a statistical sub-model for the calculation of the EAF's electrical energy demand based on the process inputs. Plant data from three different steel producers was processed and served as the basis for the development of the statistical sub-model and the model validation. The model expansion also included reworking of the port structure and addition of a case selector for the calculation of species distributions between the steel and slag phase.

To prove the accuracy and stability of the new EAF model, an extensive validation was performed, using results from established metallurgical software tools and plant data. The new EAF process model is part of a large iron and steelmaking simulation platform and has full flowsheeting capabilities. It will be used individually to simulate single equipment, or connected to other models for simulation, optimisation, and comparison of complete steelmaking operations.

Kurzfassung

Die Produktion von Stahl im Elektrolichtbogenofen macht ein Drittel der weltweiten Rohstahlproduktion aus und ist das wichtigste Stahlrecycling Verfahren. Die Verwendung von Stahlschrott im EAF führt im Vergleich zur klassischen Stahlproduktion aus Eisenerz zu einer erheblichen Reduktion der CO₂-Emissionen und des Energiebedarfes. Durch die steigende globale Verfügbarkeit von Stahlschrott und strengere Umweltauflagen in der Stahlindustrie wird der EAF-Prozess zunehmend attraktiver. Obwohl der Prozess in den letzten Jahrzehnten bereits wesentlich verbessert wurde, gibt es noch viel Potential für Innovationen. Da Anlagenversuche mit hohem finanziellem Aufwand und potenziellen Sicherheitsrisiken einhergehen, kommt vermehrt die Prozesssimulation zum Einsatz. Diese nutzt mathematische Modelle, um den EAF-Prozess besser zu verstehen, zu planen und zu optimieren.

Hauptinhalt dieser Arbeit ist die Überarbeitung, Erweiterung und Validierung eines mathematischen EAF-Prozessmodells ausgehend von einem bestehenden Modell für die metallurgische Simulationsplattform von Primetals Technologies Austria GmbH. Ein Kernthema war die Entwicklung und Implementierung eines statistischen Teilmodells zur Abschätzung des elektrischen Energiebedarfes für den EAF-Prozess basierend auf den Einsatzstoffen. Als Grundlage für die Entwicklung des statistischen Teilmodells wurden Industriedaten von drei verschiedenen Stahlproduzenten ausgewertet und aufgearbeitet. Teil der Erweiterung des alten EAF-Modells war auch eine Überarbeitung der Modellstruktur und das Einbauen eines Selektors für die Elementverteilungen zwischen der Stahl- und der Schlackenphase.

Um die Genauigkeit und Stabilität des entwickelten Modells zu garantieren, wurde es einer Reihe von Tests unterzogen und ausführlich validiert. Das neue Modell wird als Teil der umfassenden Modellbibliothek von Primetals für die strategische Produktionsplanung und die Simulation von einzelnen Produktionsschritten sowie von ganzen Stahlwerken eingesetzt.

Table of Contents

1	Introduction	1
1.1	Motivation	1
1.2	Objective	3
2	Theory and Background	4
2.1	EAF Steelmaking.....	4
2.1.1	Equipment.....	4
2.1.2	In- and Output Materials.....	6
2.1.3	Process Steps.....	10
2.1.4	Development and Innovations	12
2.1.5	Mass and Energy Balance	15
2.2	Process Modelling and Flowsheet Simulation	21
2.2.1	gPROMS ModelBuilder®.....	23
2.2.2	HSC Chemistry®.....	27
2.2.3	State of the Art EAF Modelling	28
2.3	Statistics.....	34
2.3.1	Multiple Linear Regression.....	34
2.3.2	Regression Statistics.....	35
2.3.3	Analysis of Variance (ANOVA).....	36
3	Development of the EAF Process Model	38
3.1	Model Structure	39
3.2	Black Box	42
3.3	Cooling Stack.....	51
3.4	Electrical Energy Demand Sub-model.....	52
3.5	Initialisation Procedures	54

3.6	Range and Processing of the Plant Data	55
4	Results and Validation.....	56
4.1	Electrical Energy Demand Sub-model.....	56
4.2	Validation Using Proven Models	67
4.2.1	First Operation Scenario	69
4.2.2	Second Operation Scenario.....	76
4.3	Validation Using Plant Data.....	82
4.3.1	Average Heat	84
4.3.2	Individual Heats	90
5	Summary & Outlook.....	95
6	Literature	97
	List of Figures.....	101
	List of Tables.....	105
	List of Abbreviations and Symbols.....	106

1 Introduction

1.1 Motivation

In the past two decades, the global crude steel production rose from 847 million tons in 2000 to a new all-time high of 1951 million tons in 2021 (Figure 1, left) [1]. This trend is expected to continue, since it is directly linked to the growth in world population and ongoing overall industrialization [2]. The biggest producers are China (53%), the EU (8%), India (6%) and North America (6%) [1, 3].

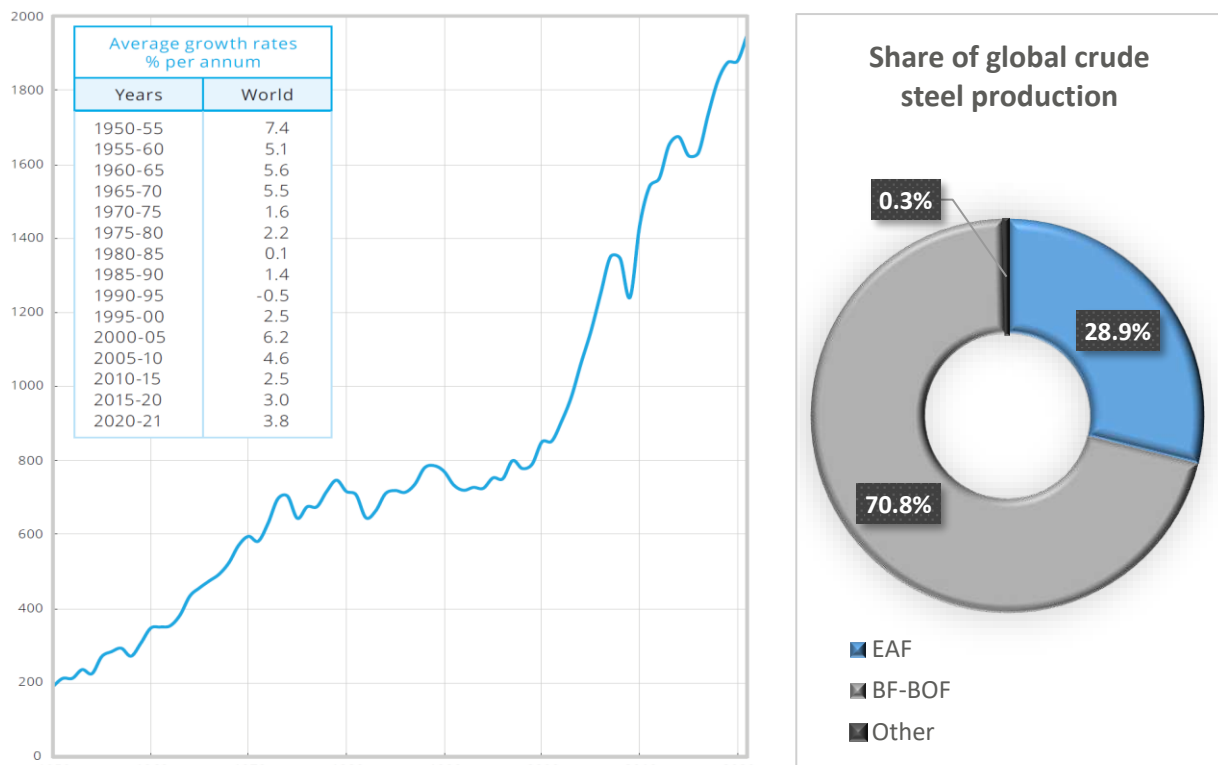


Figure 1: Global crude steel output in million tons (left). Global share of steelmaking routes for crude steel production in 2021 (right)[1].

There are two main process routes for steel production: The primary or integrated route uses the blast furnace (BF) for iron ore reduction and the basic oxygen furnace (BOF) for steelmaking, and the secondary or electric route using steel scrap or other ferrous inputs in the electric arc furnace (EAF). Which method is dominant in a given geographical area depends on factors like energy prices and raw material availability [2, 3]. While the primary steelmaking route still accounts for the majority of global raw steel production, the EAF route is on the rise with 28.9% share worldwide and 43.9% in the EU in 2021 (Figure 1, right) [1].

Like in other sectors, efforts to make steel production more environmentally friendly are ongoing. Iron and steel production uses roughly 7% of the world's energy supply [2] while being estimated to cause 7–9% of global [2] and 12% of Austrian total greenhouse gas emissions [4], making it the biggest source of anthropogenic CO₂ emissions among heavy industries. A decarbonisation of iron and steelmaking has to take place in order to meet climate change mitigation goals like the Paris Agreement's or the EU's 2030 target plan [5].

According to cradle-to-grave life cycle assessments, the use of steel scrap as an input material for steel production instead of virgin material like iron ore can potentially save 1.6 t of CO₂ emissions and 15 MJ of primary energy per ton of steel [6]. This is possible since most of the reduction work has already been done to produce the steel scrap, which already consists of more than 90% metallic iron. Additionally, the mining of 1.4 t of iron ore and 740 kg of coal can be avoided [7], making the recycling route more environmentally friendly overall. Still, EAF steelmaking generally requires a high amount of electricity, and the specific energy consumption is one of the most impactful process parameters.

While the primary steelmaking route can use up to 30% steel scrap input for cooling in the BOF process, the EAF route can use up to 100% scrap as ferrous input material, making it the only true steel recycling route. Other benefits of the EAF are the high flexibility regarding the produced steel grade, use of different raw materials and production volumes [8].

However, the EAF process is still less explored than the BF-BOF route. Since EAF plant trials are restricted or impossible due to their high cost and safety risks, process simulation using mathematical models is widely used to better understand and further optimise EAF steelmaking [9]. In recent years, Primetals Technologies Austria GmbH cooperated with the TU Wien as well as voestalpine AG to create a standardized flowsheeting simulation environment based on a comprehensive metallurgical model library. This library includes process models for all important steps needed to simulate complete integrated and recycling steel plants and enables easy comparison of different steelmaking routes [10-12]. The EAF model included in this library was the basis for the process model developed and validated in this thesis. It has full flowsheeting capabilities and will be used for desktop studies, strategic planning, and solution of optimisation problems as part of a comprehensive metallurgical simulation platform.

1.2 Objective

The aim of this thesis was the improvement of a provided EAF process model for the metallurgical simulation platform of Primetals Technologies Austria GmbH. This included reworking of the model concept, processing of plant data using python scripts and statistical tools, addition of sub-models and a model validation using plant data as well as proven reference models.

A major improvement was the development and implementation of a statistical sub-model for the estimation of the specific electrical energy consumption for the process. In addition, a case selector for new species distributions was implemented, and the model's port structure was renewed. Since the old model was not fully documented, this thesis also includes documentation for all aspects of the model.

The received EAF model from the model library of the metallurgical simulation platform was based on a black box model for a BOF and was only validated for one operation scenario using 100% scrap input based on an MS Excel tool without the use of plant data. After reworking and expansion, the new process model was validated using different steelmaking scenarios from reference models as well as the processed plant data.

Background information on EAF technologies and the calculation of mass and energy balances for the process as well as the statistical methods used in this work can be found in chapter 2. It also includes an introduction to process simulation, a comprehensive review of modelling approaches from scientific literature and a description of the used software tools.

Chapter 3 describes the developed process model as well as the most important sub-models and their functions.

The model validation is discussed in chapter 4. The first part is based on the results of proven metallurgical models while the second part covers the validation using plant data. This chapter also includes the results of the multiple linear regression approaches used to determine the regression parameters for the statistical sub-model based on plant data from 3 different EAF's.

A summary of this work and an outlook including suggestions for future improvements of the model are provided in chapter 5.

2 Theory and Background

2.1 EAF Steelmaking

An electric arc furnace melts material by converting electrical energy into heat via an electric arc. Modern industrial EAF's are used to convert steel scrap and other iron-bearing material into liquid crude steel, using a combination of electricity supplied by a high voltage system and chemical energy from fuel like coal, natural gas and oxygen. While oxygen is injected into the melt during the EAF process and some refining takes place, it is today mostly used as a "melting machine", producing crude steel, an intermediate which is then fed into secondary ladle metallurgy equipment for end refining [13-16].

While BOF steelmaking uses mainly hot metal produced by the blast furnace as input and is self-sufficient in energy, the EAF uses mainly steel scrap and electrical energy is needed for melting. Because of its higher flexibility and smaller capacities, the EAF is preferred in the production of stainless and high alloyed special steels. Another major field of use for the EAF is the recycling of steel scrap into structural steel grades. [13-16].

2.1.1 Equipment

While the high variance in ferrous inputs and produced steel grades has led to the development of many different EAF types, most EAF's use the same basic equipment. The typical components of a conventional EAF can be seen in Figure 2.

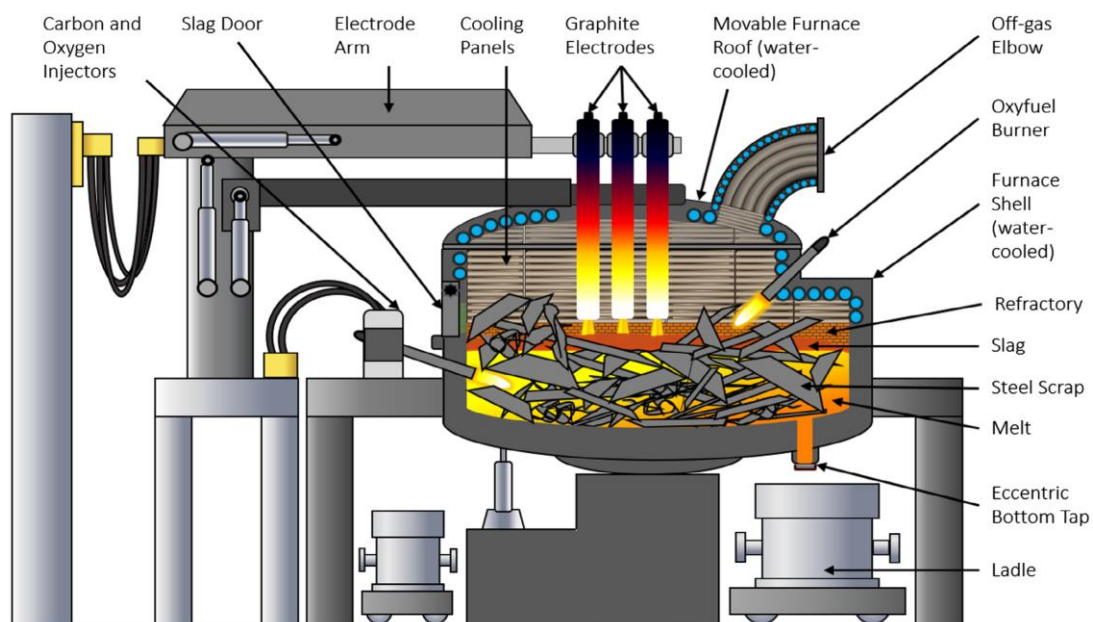


Figure 2: Schematic illustration of a conventional EAF [9].

The furnace shell is the load-bearing component of the EAF and sits on the tilt-able tapping bay. Together with the roof, it forms the furnace vessel. Both the roof and the side of the shell have water **cooling panels** to protect them from heat. The lower shell, also called furnace hearth is lined with **refractory bricks** to withstand the extreme mechanical and thermal loading during operation [9, 15].

The roof can be opened to feed scrap or other inputs into the vessel. This can be done using baskets or continuously through a designated opening, called the “5th hole”. There are also three openings in the roof for the electrodes and one for gas evacuation, called the “4th hole” or **off-gas elbow**. One gap is located in between the roof and the shell, and another one between the end of the off-gas elbow and the dedusting system (not shown in Figure 2). The gaps allow for air ingress during the process [9, 15].

Graphite electrodes are held by the electrode arm and conduct the electricity needed to generate the electric arc inside the vessel. EAF’s can be powered by alternating (AC) or direct current (DC). While AC EAFs use three electrodes, with the arcs being created between the electrodes and the metal bath, DC furnaces have one electrode, creating the arc between a central and a bottom electrode. While DC EAF’s have lower electrode consumption, their power systems are more complex and expensive. Since over 90% of the currently operating EAF’s are AC-powered, this thesis will only cover AC-EAF’s [9, 15].

Oxy-fuel burners assist in the melting process and facilitate an even heat distribution inside the furnace. The burners usually use natural gas as fuel, but the use of oil is also possible. In addition to the fuel, highly concentrated oxygen is injected to facilitate a complete combustion with little flue gas [9, 15].

Oxygen injectors are used to blow oxygen directly into the melt. The resulting oxidation reactions remove impurities from the melt as oxides, leading to slag formation and serve as a major energy source for the process, typically generating up to 30% of the total energy supply for the process. **Carbon injectors** blow fine coke or coal grains into the slag and melt and are needed for slag foaming, a practice that creates an isolating layer of foamy slag above the metal bath [9, 13-16].

The slag door is used to remove slag during the process, and the produced raw steel is tapped into a ladle via an **eccentric tap hole** at the bottom [9].

2.1.2 In- and Output Materials

Input materials

The common inputs of the EAF process can be divided into groups as seen in Tab. 1.

Tab. 1: EAF process input materials.

Ferrous materials	Slag-formers	Fuel and Gases	Other
Steel scrap	Lime	Oxygen, Air	Refractory Lining
Sponge iron (DRI/HBI)	Dolomite	Natural gas	Electrodes
Crude iron (GPI)		Coal	
Hot metal		Oil	
Ferroalloys		Argon and Nitrogen	

Steel scrap is left-over metal from product manufacturing or consumption and represents the main input for the EAF. The scrap is usually crushed, shredded, and sorted by type before it is used as feedstock for steel production. It can be grouped into internal scrap, which is reject metal from within the steel plant, prompt scrap, which is waste generated during product manufacturing, and obsolete scrap, which is recovered from industrial and consumer items after the end of their lifespan. It can further be divided depending on its form, dimensions, density, degree of alloying, degree of corrosion, and degree of preparation. For the EAF process, scrap is also often characterised by its melting temperature [7, 15, 16].

Sponge iron, usually in the form of direct reduced iron (DRI) or hot briquetted iron (HBI) can be used as a substitute or addition to scrap. This is mainly done since the global scrap availability is too low to satisfy the total crude steel demand. It can also be used to dilute impure scrap when producing high quality steels. Sponge iron is formed by the reduction of iron ores without melting them using a reducing gas (usually consisting of H₂ and CO) in rotary- or shaft furnaces or in fluidized bed reactors. It is available in lump, granulated, briquetted, or powdered form in various degrees of metallization. Some studies indicate, that the use of DRI and HBI can reduce the energy demand and increase the productivity of the EAF process. [15-17].

Crude iron produced in the blast furnace process can also be used as an iron-bearing input material. In its solid form, it comes as granulated pig iron (GPI) which consists of small iron ingots called “pigs”. The composition of the GPI, especially regarding tramp

elements and impurities is crucial. While silicon and manganese undergo exothermic oxidation reactions, lowering the EAF's electrical energy demand, they also increase the amount of slag and the amount of lime required to ensure a proper slag basicity. The slag basicity has a big impact on the lifespan of the refractory lining as well as on the slags foaming capabilities. Since phosphorus and sulphur are detrimental to the quality of the steel and are hard to remove in the EAF, minimal content of these impurities in the GPI is a requirement. In addition, the carbon content shouldn't exceed 4.5%, as the EAF has lower decarbonisation capacities than a BOF [15].

Hot metal is another form in which crude iron from a blast furnace can be introduced into the EAF. In integrated steel plants, it can be fed directly into the EAF. The use of hot metal can save large amounts of electrical energy, since the material is already heated. However, since a blast furnace is needed this is often not economically feasible and the environmental benefit of using the EAF route is lost [15].

Ferrous alloys consist of alloying elements and iron. Usually, they are added at the end of the EAF process or after tapping into the ladle. Addition of ferrous alloys often represents the cheapest and most practical option to introduce the needed alloying elements to the crude steel. Ferrous alloys including elements with high oxygen affinity are also used as deoxidizing agents (e.g. Ferrosilicon) [15].

Slag-forming materials are needed to form an adequate amount of slag and to control its chemical composition. Slag is a by-product of the extraction and refining processes inside the EAF. The most commonly used slag former in the EAF process is lime, which acts as the main CaO carrier with a CaO content of up to 94%. Dolomitic lime, also called dolomite, has a higher MgO content of 20-50% and is frequently used to control the slags MgO content. The slag composition has a major impact on slag foaming and refractory wear, as a more acidic slag will erode the bricks faster [15].

Coal is used as the main carrier of carbon, and it serves multiple purposes in the EAF process. It is an alloying steel component, a source of thermal energy via its oxidation, and a slag foaming agent especially important for the foamy slag practice. It can be introduced in the form of lumps with the ferrous charge or as carbon powder which is injected directly into the melt as a foaming agent [15].

Graphite electrodes are used to conduct the electricity from the high-power system into the EAF and must therefore have high temperature resistance, a high electrical

conductivity and small thermal conductivity. During the process, the arcs burn away part of the electrodes. While the electrode wear has a small impact on the overall mass balance, it is an important economical factor, because of their high price [15].

Oxygen is the most important process gas and one of the main energy sources for the EAF. The needed oxygen for the refining process is injected into the metal bath using consumable pipes or water-cooled lances. Additional oxygen for fuel combustion and post combustion of CO is introduced by oxy-fuel burners or by ingress air from gaps [15].

Argon and nitrogen are injected into the melt from the bottom for stirring, as slow mixing of the metal bath is often a limiting kinetic factor for the occurring reactions [16].

Output materials

The outputs of the EAF are liquid crude steel of varying quality, slag, dust and off-gases.

Steel produced in the EAF can be classified in 3 major groups:

Structural carbon or low-alloy steel grades, which are made of low-alloy scrap by melting the charge to produce crude steel for further refinement in the secondary metallurgy [15].

Medium and high-alloy steel grades are produced from high alloy scrap. The process is performed with a limited or without an oxidizing period. This enables the recovery of valuable alloying elements from the scrap, which would otherwise be oxidised and removed as slag. The end refining of the crude steel takes place in secondary metallurgy equipment [15, 16].

High-chromium steel grades, often with 15% to 30% chromium content and 0.02%–0.08% carbon are made by processing of high-chromium scrap. The challenge faced in this process is to remove carbon by oxidation without simultaneous oxidizing the valuable chromium. This can be realised by conducting the process at high temperatures of 1750 to 1850 °C) or by using vacuum oxygen decarburization (VOD), where the carbon is oxidized under vacuum by placing a ladle in a vacuum chamber. By lowering the CO-partial pressure, carbon oxidation is possible at a lower oxygen partial pressure, while chrome oxidation remains almost unaffected [15, 16].

Slag is the main by-product of the EAF process with about 100–200 kg per ton of crude steel produced [18] (for structural grade steels). The EAF slag serves several purposes: Its main function is to absorb the deoxidation products and impurities from the molten

steel. It also protects the electrodes and refractories in the furnace from thermal radiation as well as the molten steel against re-oxidation. In addition, it insulates the melt, preventing thermal losses to the surroundings. The main components of the slag are oxides of iron, calcium, silicon, magnesium, manganese and aluminium oxides. Minor components are lead, phosphorus, fluoride and other trace elements. EAF slag can be divided into slag from carbon steel production, which is considered mostly unproblematic for deposition, and slag from high alloy steel production, which requires further processing before deposition. EAF slag can be applied as coarse aggregate in asphalt mixes and concrete, or used as a partial replacement of cement [3, 16, 19, 20].

Off-Gas & Dust

Toxic off-gases and dust emissions are the biggest environmental threat of EAF steelmaking. Complex off-gas capturing and treatment systems are used to collect dust and off-gases directly from the freeboard via the off-gas elbow as well as emission occurring outside of the EAF while tapping. These systems include fans, filters, post combustion chambers and chimneys. They capture off-gases from inside the furnace through the off-gas elbow and from above the furnace by fume hoods. Most of the off-gas is created by the oxidation of carbon during oxygen blowing, during the post combustion processes in the freeboard zone, and during charging, when impurities in the scrap like oil, plastics, paint and parts of the charged coal are burned and moisture evaporates. While the amount and composition of the off-gas varies highly during the process, a typical composition found in the scientific literature for gas exiting the freeboard (vol%) would be 10 to 15% CO₂, 5 to 15% O₂, 5 to 25% CO, 5 to 10% H₂ and 50 to 70% N₂ for dry gases [13]. The off-gas temperature varies between 400 to 600 °C at the beginning of the melting and 1500–1600 °C during oxygen blowing [13]. When CO post-combustion occurs, even higher temperatures can occur in the freeboard zone. One of the most dangerous pollutants are dioxins. They can be generated from organic impurities of the scrap, especially when scrap preheated systems, which cool down the off-gas, are used. At off-gas temperatures above 1000 °C, dioxins are almost entirely decomposed, but they can be de novo synthesized together with other organic pollutants if the off-gas temperature drops to a range between 300 and 800 °C. To avoid this range, the off gas is rapidly cooled in quenching towers from roughly 1300 to 250 °C [9, 13-16, 21].

EAF dust is mainly generated by metal evaporation, steel and slag spitting and subsequent oxidation of the particles. The specific dust output is usually around 20 kg/t steel. The

dust consists of fine, highly dispersed particles, with most of the particles having a size under $2\ \mu\text{m}$. The composition depends on the used ferrous inputs, but the main components are usually iron and zinc oxides. EAF dust contains lead, cadmium and other heavy metals, as well as chlorides from scrap impurities, and is considered hazardous in many countries. The dust can be treated using hydrometallurgical or pyrometallurgical methods to extract non-ferrous metals like zinc or lead. It can then be recycled in the steel, cement or construction industry. While pyrometallurgical methods require high temperatures, hydrometallurgical leaching, for example using sulphuric acid, happens at lower temperatures and saves energy [9, 13-16, 22].

2.1.3 Process Steps

The EAF process is conducted in batches called “heats” or “tap-to-tap cycles”. One batch can be divided into four main steps: Charging, melting (consisting of ignition, boring and main melting phase), refining or flat batch phase, and tapping. A visual representation of the steps is depicted below in Figure 3 [23].

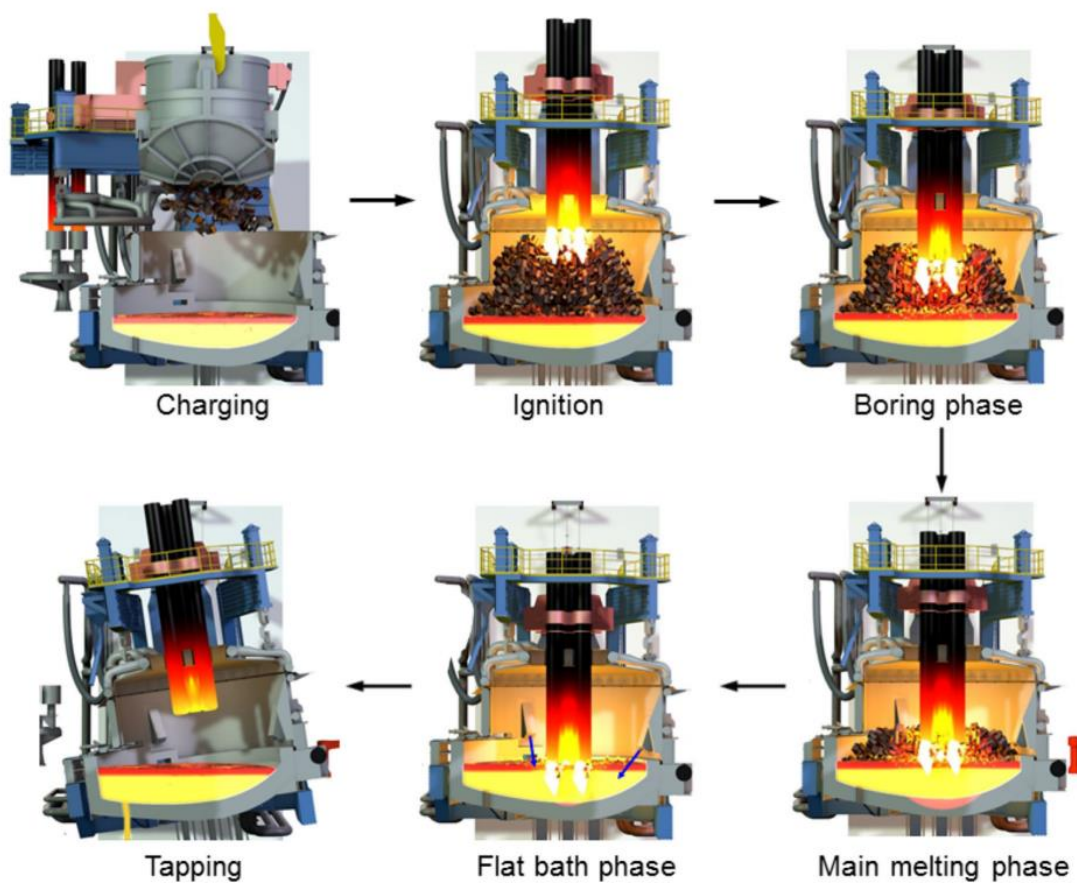


Figure 3: Stages of the EAF batch process [23].

Charging: Since most EAF use the hot heel practice, the shell already includes some residual melt from the last heat before charging, to work as a heat reservoir and accelerate the meltdown. Scrap is charged using one, two or three scrap buckets after swinging out the furnace roof or through openings in the furnace roof. The use of a single bucket saves energy because of the shorter loading time. The scrap mix already includes some carbon to minimize iron loss during melting. The addition of lime as well as dolomite throughout the charging phase helps to control the slag amount and composition [9, 23, 24].

Melting: The melting phase can further be divided into ignition, boring and the main melting phase. After closing the roof, the graphite electrodes are moved down into the vessel before the electric arcs between the electrodes and the scrap are ignited. During the boring phase the electrodes are above the scrap and since the scrap does not yet isolate the walls and roof from the thermal radiation, the arc is kept short. To speed up the boring, fast melting scrap is put on top of the scrap charge. When the electrodes have entered the scrap pile, the arc can be lengthened by increasing the voltage and the main melting period begins. Oxy-fuel burner speed up the melting and help with heat distribution. In most cases oxygen is already injected into the metal bath during the melting and the resulting oxidation reactions serve as another energy source. The charged carbon dissolves and the slag begins to form [9, 23, 24].

Refining: The refining or flat bath phase begins once all the scrap is molten. Since there is no solid scrap to shield the furnace walls from heat, the arc length is decreased again to prevent hot spot formation and refractory wear. Additionally, a foamy slag layer should already be in place to isolate the bath. During the refining, more Oxygen is injected into the melt. The most important occurring oxidation reactions are the oxidation of carbon as well as silicon, manganese, iron and phosphorous. The escaping gaseous CO also produces a “carbon boil” in the melt, facilitating heat transfer by stirring the bath, removing retained oxides as slag, and aiding in the removal of H₂ and N₂. The formed slag is continuously removed through the slag door. In the refining phase, the bath is also superheated in preparation for the secondary metallurgy. Deoxidation takes place before tapping or right after tapping into the ladle. Oxygen is removed from the melt by addition of ferroalloys with a high oxygen affinity like ferro-silicon or aluminum [9, 15, 23, 24].

Tapping: After the molten crude steel reaches the target composition and temperature, it is poured into a pre-heated ladle through an eccentric bottom tapping hole by tilting the EAF [9, 23, 24].

2.1.4 Development and Innovations

The first laboratory-scale EAF was designed by Carl Wilhelm Siemens in 1878 and the first industrial EAF prototype was invented by Paul Héroult in 1889. While electric steelmaking started out as a niche process used in the production of special steels with high melting temperature, EAF's are nowadays widely used in recycling as well as integrated steel plants, and they can produce a wide variety of steel grades from many different ferrous input materials. In the last decades an impressive number of innovations has significantly improved many key performance parameters of the EAF process, as illustrated in Figure 4 [13-16].

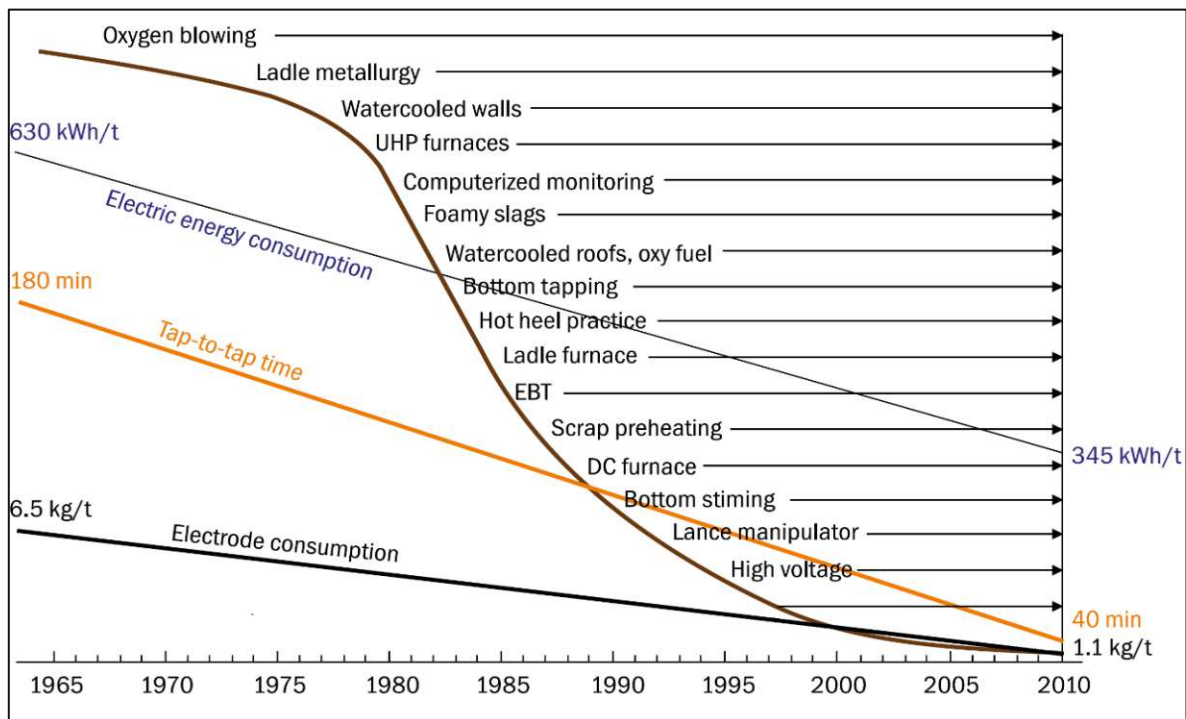


Figure 4: Technological development in the EAF sector [24].

When comparing a modern EAF with a tap weight of 120 t using 100% steel scrap with one from the 70s, the average electrical energy consumption per ton of steel got approximately halved from 630 to 345 kWh/ton, the tap-to-tap time went down from 180 to 40 minutes and electrode consumption has been reduced 4–5 times. Since this time, EAF's are often used for recycling of steel scrap into structural steel grades in smaller, locally focused steel plants, so-called minimills [13-16].

EAF steelmaking is a batch process, and most of the EAF's innovations target a shortening of the total time for an individual heat called the "tap-to-tap time", representing a higher

steel production rate. This is mainly possible by introducing more energy into the furnace to speed up the melting process [13-16].

The first major improvement in EAF steelmaking was the application of oxygen blowing into the metal bath. The resulting exothermic oxidation reactions generate heat, lowering the demand for electrical energy input. The blowing also decarburizes the metal bath and facilitates the removal of impurities like tramp elements. To prevent iron oxidation from the intense oxygen blowing, carbon is injected as well as part of the so called “foamy slag practice”. The carbon reduces iron oxides, preventing drops in yield. The created small CO travel through the melt and cause the slag to foam. The foamy slag stabilizes the arc, shields refractories from arc plasma and heat, reduces heat loss and prevents reoxidation of the melt [13-16].

Another important step was the application of water-cooling systems for the furnace shell. Cooling panels are installed on the walls and roof, allowing faster heating of the bath without the furnace shell taking damage. This also allowed for a higher electrical energy input which led to rising productivity. While first-generation furnaces had transformer ratings of up to 250 kVA/t steel and productivities of 15–20 t/h, the transformer capacity was increased in the 1960s and 70s from 250 to 450 kVA/t and productivity rose to 40 t/h. In the 80s, high-and ultra-high power EAF’s were introduced, with transformer ratings of 450 to 700 kVA/t for high-power and 700-1400 kVA/t for ultra-high power EAF’s. Capacities have reached around 100 t/h for high power up to 400 t/h for modern ultra-high power EAF’s [13-16].

Another common practice is the use of a hot heel, meaning that not all the crude steel is tapped, and a fraction remains in the furnace hearth. The remaining liquid crude steel speeds up the melting phase by improving heat conduction as well as the slag formation during the start of the following heat [13].

The trend of ongoing improvement in the EAF process is expected to continue considering new developments in automation and process control as on-line simulation models are more and more widely used. In addition, numerous efforts are being made to make the EAF process greener. Their goal is usually to save energy by using off-gas or slag heat recovery, to reduce emissions by the facilitating a more complete post combustion and better off-gas treatment or to reduce waste by recycling EAF slag and dust [25-27].

EAF Types

The great innovation in the EAF sector has also led to the development of many different EAF types. The most important technological categories are EAF's without scrap preheating, EAF's with scrap preheating and EAF's with continuous feed of ferrous inputs. The plant data used in this work included heats from a conventional EAF (Figure 2), a Quantum EAF (Figure 5, left) and a Conarc EAF (Figure 5, right).

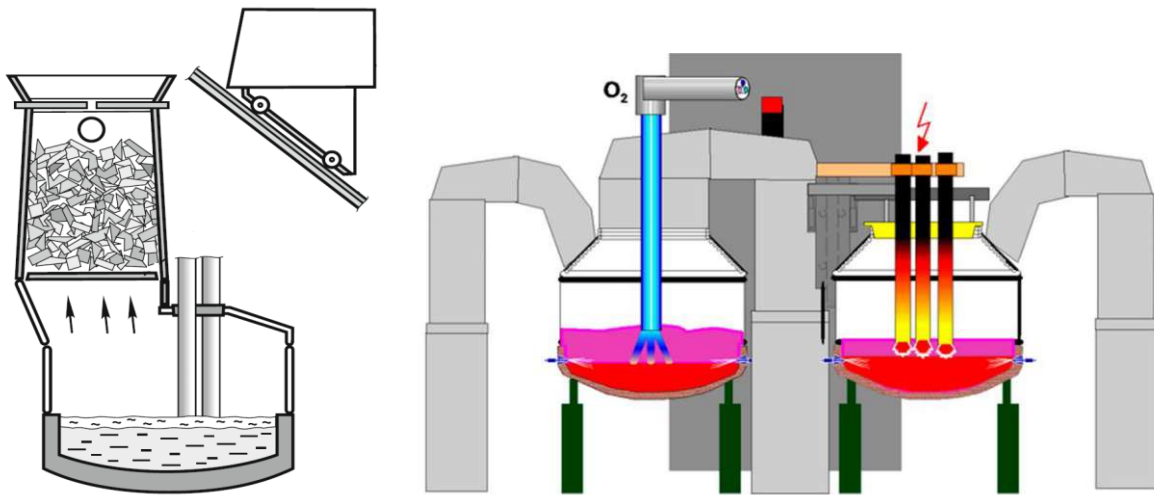


Figure 5: Quantum EAF(left) [13] and Conarc EAF (right) [28].

The Conarc EAF uses two furnace shells and is a combination of the BOF and EAF process. It features a rotating electrode arm and a rotating top lance for oxygen blowing. The shells are used interchangeably as a BOF or EAF and while the EAF is used for melting of the scrap input and superheating the melt the BOF is used for decarburization. This is because the BOF generally has a much higher decarburization rate compared to an EAF, while the EAF is a more energy efficient melting unit [29].

The Quantum EAF retains scrap in the furnace shaft using a finger system. The off-gases from the vessel are guided through the shaft, where additional post combustion takes place and the scrap is preheated. According to scientific literature the recovery of energy from the scrap preheating reduces the total energy demand on average by 13.7% [30]. The preheating shaft is loaded with scrap by an elevator-mounted tilting container with the charging process as well as scrap management in the scrap yard being highly automated. To prevent the formation of dioxins and furans at the lower off-gas temperatures after the preheating chamber, a post-combustion chamber with additional natural gas burners followed by a quenching tower are used [30].

2.1.5 Mass and Energy Balance

Mass balance

Mass balances are an important tool for the evaluation of a process and often provide the foundation for the calculation of energy balances. For the EAF process, many of the in- and output stream are not measured in daily production, which is why special measurement campaigns, for example to gain data on the off-gas amount and composition, are needed to equate accurate mass balances.

Under the assumption of conservation of mass, the mass of the inputs is equal to the mass leaving the system and the mass accumulate within the system. Assuming that mass and composition of the hot heel stay relatively constant between heats and that no other mass accumulation takes place over the process (steady-state assumption), a basic mass balance for the EAF process can be written according to eq. (1) [16, 31, 32].

$$\begin{aligned}
 & m_{\text{Ferrous inputs}} + m_{\text{Slag formers}} + m_{\text{Coal}} + m_{\text{Electrodes}} + m_{\text{Refractory}} \\
 & + m_{\text{Oxygen}} + m_{\text{Natural gas}} + m_{\text{Air}} + m_{\text{Oxygen}} \quad (1) \\
 & = m_{\text{Steel}} + m_{\text{Slag}} + m_{\text{Off-gas}} + m_{\text{Dust}}
 \end{aligned}$$

Actual in- and output values can vary widely depending on the used input material and the desired steel grade. Figure 6 includes a range as well as an example for an average mass balance of a conventional EAF with a tap weight of 100t [18].

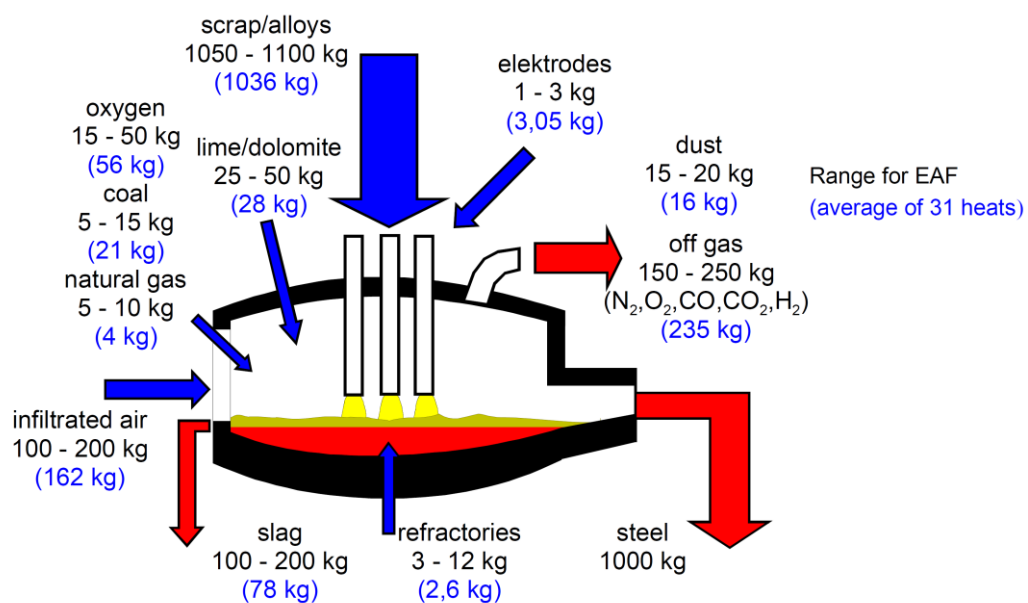


Figure 6: Typical mass balance for a 100t-EAF using 100% scrap input [18].

Energy balances

Energy balances play an integral role in understanding the EAF Process. While the EAF utilizes electrical as well as thermochemical energy, it can be assumed that over the whole process, the different energy forms are eventually used or lost as heat. Hence the energy balance is also called heat balance in the scientific literature. The system boundary for the balance can include different zones and time intervals of the EAF process [13].

The first law of thermodynamics, which states that the total energy input must be equal to the total energy output plus the energy change within the system, serves as the basis for the equation of a so-called total energy balance. If we regard the furnace as an open system and if we assume that the internal energy U_{EAF} of the system does not change over the process, the energy balance can be represented by eq. (2) [13, 18, 33].

$$\frac{dU_{EAF}}{dt} = \sum_i \dot{m}_i \cdot (u + pv + e_k + e_p)_i + \sum_i \dot{Q}_i + \sum_i \dot{W}_i = 0 \quad (2)$$

With \dot{m}_i represents a mass stream entering or leaving the system, u and v being the mass specific internal energy and volume, e_k and e_p being the mass specific kinetic and potential energy, and p being the pressure of the streams. \dot{Q}_i and \dot{W}_i are the heat and work transfers over the system boundary. If we assume constant pressure and if all form of work other than electrical work and pressure-volume work as well as kinetic and potential energy are neglected, we can introduce the mass specific enthalpy h_i and represent the energy of the mass streams (\dot{m}_i) with enthalpy streams (\dot{H}_i) [31].

$$\dot{H}_i = \dot{m}_i \cdot (u + pv)_i = \dot{m}_i \cdot h_i \quad (3)$$

The interval for the energy balance will be the complete tap-to-tap time from T_0 = charging to T_1 = tapping. We can now write the energy balance as a sum of energy changes according to eq. (4).

$$\sum_i \left[\int_{T_0}^{T_1} (\dot{H}_i + \dot{Q}_i + \dot{W}_i) dt \right] = \sum_i \Delta H_i + \Delta Q_i + \Delta W_i = 0 \quad (4)$$

The next step in equating the energy balance is the definition of a system boundary.

The system boundary used in this work is represented by zone a in Figure 7. It includes the furnace (zone c) with the bath (zone d) up to the gap at the end of the roof elbow as well as the transformer and the high current system (zone b). It excludes the dedusting system, the off-gas post combustion and any scrap preheating systems (zone e) [13, 34, 35].

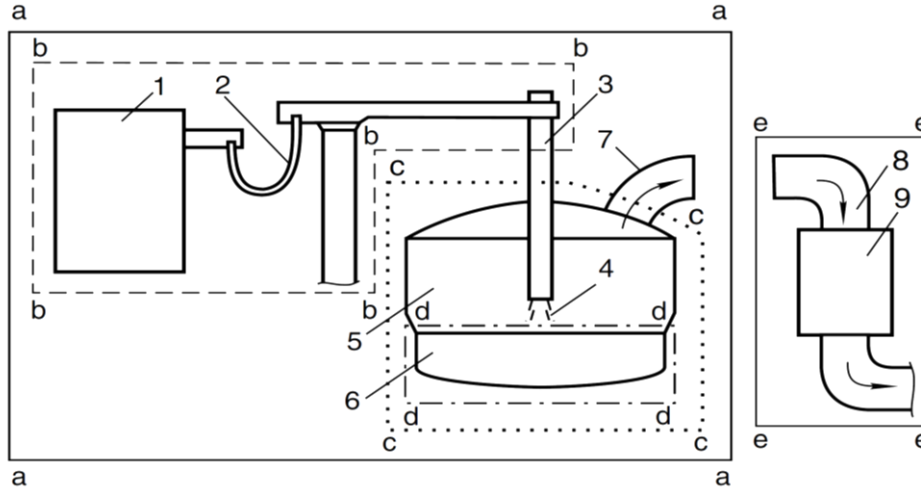


Figure 7: System boundaries for EAF energy balances: transformer (1); secondary circuit (2); graphite electrodes (3); electric arcs (4); freeboard zone (5); metal bath (6); off-gas elbow (7); gas duct (8); heat exchanger for scrap preheating (9) [13].

For zone (a-a), the balance can be written as eq. (5). The individual terms are described in Tab. 2. The values are usually divided by the tap weight and given in kWh/ton steel produced to facilitate the comparison of different EAF's [16, 35].

$$\Delta W_{Electric} + \Delta E_{Chem} + \Delta H_{Scrap, HM} = \Delta H_{Steel} + \Delta H_{Slag} + \Delta H_{Off-gas} + \Delta Q_{Cooling} + \Delta Q_{Rad, other} \quad (5)$$

Tab. 2: Typical terms considered in the EAF energy balance (kWh)

Symbol	Description	Equation
$\Delta W_{Electric}$	Electrical energy	$\int_{Start}^{Tap} P_{EL} dt$
ΔE_{Chem}	Thermal effects of all chemical reactions	$\Sigma \Delta H_{Chem}$
$\Delta H_{Scrap, HM}$	Enthalpy of ferrous inputs	$m_{scrap} \cdot h_{scrap}$
ΔH_{Steel}	Enthalpy of steel	$m_{steel} \cdot h_{steel}$
ΔH_{Slag}	Enthalpy of slag	$m_{slag} \cdot h_{slag}$
$\Delta H_{Off-gas}$	Enthalpy of the off-gas	$\int \Delta \dot{H}_{Off-gas} dt$
$\Delta Q_{Cooling}$	Heat loss of the cooling system	$\int \Delta \dot{Q}_{Cooling} dt$
$\Delta Q_{Rad, other}$	Radiation and other losses	$\int \Delta \dot{Q}_{Rad, other} dt$

$\Delta W_{Electric}$ is the amount of electrical energy delivered from the electrical grid for the duration of the heat. It can be measured directly at the EAF's transformer using a watt-hour meter. How much of the EAF's total energy input is electrical energy can vary widely. While 40 years ago the share was typically 70–75%, it has since dropped to about 50% in modern EAF's, and can be 30% or lower if hot metal is used as an input [13, 15].

$\Delta H_{Scrap, HM}$ represents the enthalpy delivered as sensible heat from inputs like hot metal, preheated scrap or hot DRI. This input of thermal energy can greatly reduce the demand for electrical energy [13].

ΔH_{Steel} , ΔH_{Slag} are the steel and slag enthalpies removed by the tapped steel and slag. They can be calculated by using the tapped masses and the mass specific enthalpies which depend on the chemical compositions of the streams and their temperatures [13, 35].

$\Delta Q_{Cooling}$ accounts for the heat removed by the EAF's water-cooling systems.

$\Delta \dot{Q}_{Rad, other}$ represents radiation losses to the surroundings, especially through the bottom of the furnace as well as electrical losses, for example ohmic loss from the electric circuit of the power system and other, non-accountable losses [13, 35, 36].

$\Delta H_{Off-gas}$ is the sensible heat removed with the off-gases. It is often exaggerated in publications by including not only the physical heat of the off-gas but also the potential chemical energy that could be released if all the CO were combusted to CO₂. This does not disturb the equality of inputs and outputs if the potential energy of carbon is also regarded as an input, but it distorts the rations of different types of energy in and outputs. The exact post combustion degree of CO in the freeboard zone, which results from oxidation by ingress air and oxygen from the oxy-fuel burners, is hard to measure [13, 19].

Estimation of the chemical energy

ΔE_{Chem} is the sum of thermal effects from all chemical reactions ($\Sigma \Delta H_{Chem}$). It is also called the chemical energy input, and the most impactful shares are shown in in eq. (6).

$$\Delta E_{Chem} = \Delta H_{COx} + \Delta H_{NG} + \Delta H_{MetOx} + \Delta H_{SF} + \Delta H_{Sol} \quad (6)$$

ΔE_{Chem} includes the change in enthalpy from oxidation of carbon (ΔH_{COx}), natural gas combustion (ΔH_{NG}) and metal oxidation (ΔH_{MetOx}). ΔH_{SF} and ΔH_{Sol} are the enthalpy changes of slag formation and dissolution of elements into liquid iron [13, 15].

The calculation of ΔE_{Chem} requires a comprehensive material balance of all chemical compounds to quantify the degrees to which carbon, iron, silicone, manganese chrome and other elements are oxidized in the process. Additional knowledge on how the different oxides interact in the slag is also needed [13, 15].

For example, the mass specific standard enthalpy of reaction (Δh_{298}^0) for the oxidation of C(s) is around 2.55 kWh per kg C to CO(g) and 9.11 kWh per kg C to CO₂. To calculate ΔH_{COx} correctly, the CO post combustion degree needs to be known. In the same manner, when calculating ΔH_{MetOx} , the iron distribution between steel and slag, as well as the FeO to Fe₂O₃ ratio in the slag must be known etc. One can conclude that to calculate ΔE_{Chem} correctly, accurate off-gas measurements and analysis of slag samples are essential. Many different methods to estimate ΔE_{Chem} have been found in the literature [13, 15].

A basic approach is the use of so-called “energy equivalent” of oxygen. This method only takes oxidation reactions into account and tries to establish a linear relation between the amount of injected oxygen and ΔE_{Chem} . This method yields inaccurate results, since the amount of chemical heat released does not only depend on the amount of injected oxygen, but also on the substance being oxidized, the used injection equipment, the time it is injected during the heat and other parameters [13].

Another approach is the use of mass specific standard enthalpies of chemical reactions Δh_{298}^0 , usually given in kWh/kg reactant. Δh_{298}^0 represents the quantity of heat released by the reaction of 1 kg of reactants under standard conditions. Values for Δh_{298}^0 can be found in data tables or calculated using the mass specific standard enthalpies of formation $\Delta_f h_{298}^0$ for the products p and the reactants r , their stoichiometric coefficients ν and molar mass M according to eq. (7) based on Hess's law. The thermal effect of all considered reaction can then be calculated by equation (8) [13].

$$\Delta h_{298}^0 = \sum_{products,p} \frac{\nu_p}{M_p} \cdot \Delta_f h_{298}^0(p) - \sum_{reactants,r} \frac{\nu_r}{M_r} \cdot \Delta_f h_{298}^0(r) \quad (7)$$

$$\sum_i \Delta H_{298}^0(i) = \sum_i \Delta h_{298}^0(i) \cdot m_i \quad (8)$$

This method is convenient, but the resulting reaction enthalpies are only accurate if reactants and products have the same temperature, and the reaction takes place at 298 K under 1 atm of pressure [13].

The reaction enthalpy at a different temperature ΔH_T^0 can be calculated, for example according to eq. (9), by using the temperature dependant standard difference in heat capacity between products and reactants at constant pressure (ΔC_p) [13].

$$\Delta H_T^0 = \Delta H_{298}^0 + \int_{298}^T \Delta C_p dt \quad (9)$$

However, data on the temperature dependence of the heat capacity are often unavailable at the extreme temperatures occurring during the EAF process [13].

Another calculation practice, sometimes called the method of “total enthalpy”, utilizes thermodynamic lookup tables with values for mass specific enthalpies of formation of a substance at different temperatures $h_T^0(i)$. $h_T^0(i)$ represents the enthalpy of formation at temperature T for the component i from its composition elements in their respective standard state under constant pressure. The required enthalpy tables can be found in thermodynamic databases or calculated by simulation software like HSC chemistry. The thermal effect can be calculated as seen in eq. (10) [13].

$$\sum_i \Delta H_{Chem}(i) = \sum_{products,p} m_p \cdot \Delta h_{T_p}^0(p) - \sum_{reactants,r} m_r \cdot \Delta h_{T_r}^0(r) \quad (10)$$

One factor that is not considered when using enthalpies of chemical reactions or enthalpies of formation are the thermal effects of slag formation and of dissolution of substances in the melt. To estimate these effects, data tables of the mass specific enthalpy of slag formation from solution in iron Δh_{sf} and the mass specific heat of dissolution into liquid iron Δh_{sol} can be used and the calculation can be done according to eq. (11) and eq. (12).

$$\Delta H_{sf} = \sum_i m_i \cdot \Delta h_{sf}(i) \quad (11)$$

$$\Delta H_{sol} = \sum_i m_i \cdot \Delta h_{sol}(i) \quad (12)$$

2.2 Process Modelling and Flowsheet Simulation

In large parts of natural sciences and engineering, modelling and simulation have become an integral pillar of knowledge acquisition. While in the past, only experiments or theoretical investigations could be used to better understand, predict, or optimize a process, this can nowadays be done in a safer, cheaper and more elegant way by developing a model, running simulations, and interpreting the results. The basis for modern process modelling is the combination of mathematics and computer science [37].

The field of applications includes the comparison of different scenarios, simulation of dangerous process states or incidents without actual risk, and training personnel on simulators. The general aim of modelling is to accurately represent the real process, making it possible to simulate different use cases and make it possible to derive knowledge from the simulation. However, correctly interpreting the result is sometimes not trivial since intermediate steps are not always known. In addition, costly software licences as well as highly trained operators are often needed [5].

While *modelling* describes the development of a new model to represent a processes or system by abstracting its structure, function or behaviour, *simulation* is the mathematical solving of the model to obtain knowledge that can be transferred to real life. In flowsheet simulation, sub-models or unit operations are often used. They are smaller models representing single steps of a complex process. The sub-models are then connected by mass, energy and information streams and depicted in a flow chart. If input and process parameters are correctly defined, the simulation software can then solve the flowsheet using data based on chemical, thermodynamic physical and kinetic properties [38].

Different flowsheeting tools can be classified by their time dependency into steady-state and dynamic tools. Steady-state simulation assumes that variables are constant with respect to time and usually need less processing power by several magnitudes. Dynamic simulation, on the other hand, can handle time dependencies and is also capable of simulating start-up and shut-down scenarios or test different control strategies. Solution strategies can be divided into modular-sequential and equation-oriented approaches. In modular-sequential programs, unit operations are solved one after another, and the output of one unit operation is used as the input for the next. Using this approach, recycling streams must be solved iteratively, often leading to convergence issues. If

equation-oriented solvers are used, the system of equations is solved simultaneously. Some examples of flowsheet simulation tools and their classifications can be found in Figure 8 [11].

A special case of simulation software are Computational Fluid Dynamics (CFD) programs, like Fluent[®], CFX[®] or Openfoam[®], that analyse and solve problems involving fluid flows with spatial, three-dimensional resolution. In an EAF steelmaking context, CFD based simulation tools represent the most complex and most analytical models. They can, for example, simulate the heat transfer and the thermal profile of the steel, slag and off-gas phases during the EAF process to predict hot spot formation inside the shell. In the following subchapters, the simulation software used in this work and state-of-the-art EAF models from the scientific literature will be presented [23].

		Time Dependence	
		Steady-state	Dynamic
Solver Strategy	Modular- Sequential	Aspen Plus [®] COCO [®] ChemCAD [®] DWSIM [®]	ChemCAD [®]
	Equation oriented	IPSEpro [®] gPROMS [®]	IPSEpro [®] Aspen Dynamics [®] gPROMS [®]

Figure 8: Different flowsheeting simulation software and their classification by solver and time dependency [11, 38].

2.2.1 gPROMS ModelBuilder[®]

For most of the modelling in this thesis, the equation-oriented flowsheeting environment of gPROMS ModelBuilder[®] (version 7.0.9, [39]) by Siemens Process Systems Engineering was used. Among researchers in academia, as well as in the pharmaceutical and petrochemical industry, gPROMS is widely utilized. It was selected due to its ability to handle multiple components and phases, providing good control over the initialisation procedure and solver options as well as its flowsheeting capabilities that enable easy combination of multiple models and sub-models in one flowsheet. This allows for modelling of complex processes by building large flowsheets, representing, for example, a complete integrated steel plant. Using gPROMS can save modelling time, since coding of the solution algorithms, which for example is necessary in the case of other programs such as MATLAB, is not always required. A gPROMS model can also be connected with other software, for example MS Excel, Aspen Plus or MATLAB Simulink using built-in interfaces [10, 39, 40].

Figure 9 shows the applications graphical user interface (GUI). It consists of the projects tree with a folder structure as well as the main working window, depicting different entities. The project tree (left) includes a list of available libraries, projects, models, and case files. Libraries are collections of models for potential re-use [10, 39, 40].

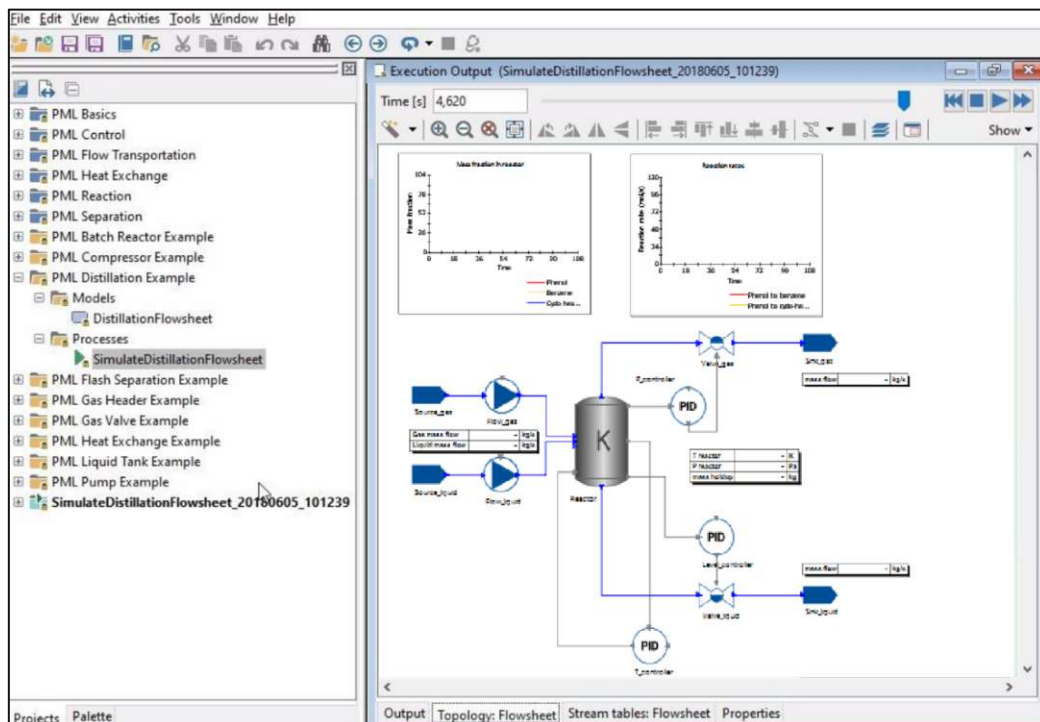
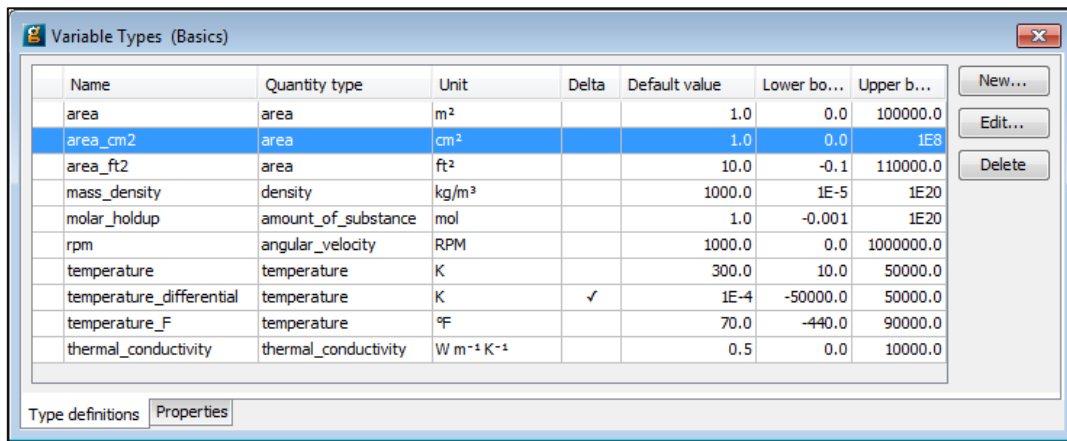


Figure 9: gPROMS ModelBuilder GUI [39].

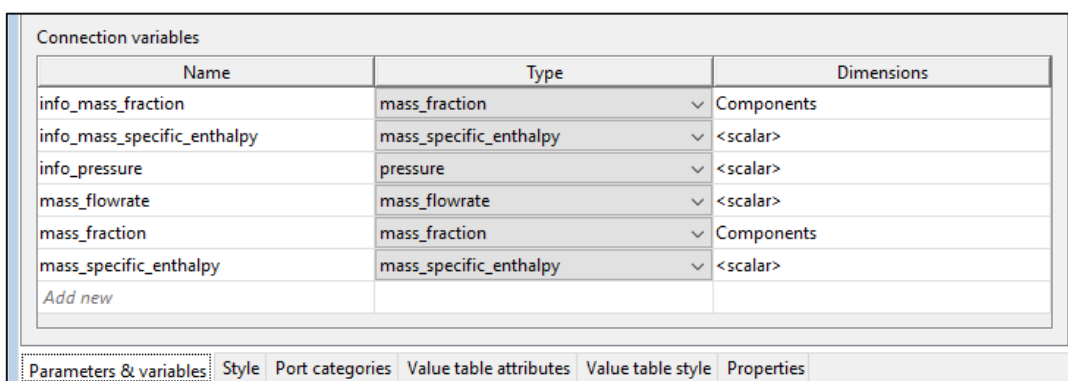
The folders that include models and process files for a specific simulation purpose are called “projects”. Case files represent records of inputs and results as well as diagnostic messages of a simulation. In the main working window, entities like the topology of a flowsheet as well as the underlying code, called gPROMS language, can be displayed and edited. The most important entities are “variable types”, “connection types”, “models” and “processes”. All variables used in a model must be assigned a name and a variable type (e.g., “temperature_C” for the temperature in °C) as seen in Figure 10. These variable types include an initial value as well as upper and lower bounds for the variable. Units of measurements for each variable type can be defined and will be displayed in value tables of the simulation output [10-12, 39].



Name	Quantity type	Unit	Delta	Default value	Lower bo...	Upper b...
area	area	m ²		1.0	0.0	100000.0
area_cm2	area	cm ²		1.0	0.0	1E8
area_ft2	area	ft ²		10.0	-0.1	110000.0
mass_density	density	kg/m ³		1000.0	1E-5	1E20
molar_holdup	amount_of_substance	mol		1.0	-0.001	1E20
rpm	angular_velocity	RPM		1000.0	0.0	1000000.0
temperature	temperature	K		300.0	10.0	50000.0
temperature_differential	temperature	K	✓	1E-4	-50000.0	50000.0
temperature_F	temperature	°F		70.0	-440.0	90000.0
thermal_conductivity	thermal_conductivity	W m ⁻¹ K ⁻¹		0.5	0.0	10000.0

Figure 10: Variable Types declared in gPROMS ModelBuilder [39].

To link the different models together and combine them as part of a flowsheet, connection types must be established. In this work, the information that is transferred between models is temperature, pressure, and chemical composition. Additional information, such as melt rates, can be transferred via special information ports. All values can be provided in scalar or in vector form [10, 39, 40].



Name	Type	Dimensions
info_mass_fraction	mass_fraction	Components
info_mass_specific_enthalpy	mass_specific_enthalpy	<scalar>
info_pressure	pressure	<scalar>
mass_flowrate	mass_flowrate	<scalar>
mass_fraction	mass_fraction	Components
mass_specific_enthalpy	mass_specific_enthalpy	<scalar>
Add new		

Figure 11: Material connection type from the gPROMS ModelBuilder [39].

The writing of the programming code, called gPROMS language, is mainly done in the model entity (Figure 12). It is used to write mathematical equations representing the behaviour of a process or system, like mass- and energy balances, distributions, or chemical reactions [10-12].

The “interface language”-tab can be used to create dialog boxes for selecting of input parameters for a model. For every model, a separate initialisation procedure can be defined. This procedure determines the order in which the models are solved in a specific flowsheet or the sequence of steps used to solve a single model. The initialisation also handles occurring recirculation to avoid convergence issues [10-12, 39].

Often, existing models are used as parts of new models in the form of sub-models. Many models have multiple layers. A visual depiction of a layer is also called the model topology (Figure 9, right). It shows the structure of the model including all sub-models and their connections [10-12, 39].

```

1  PARAMETER
2  Density          AS REAL
3  CrossSectionalArea AS REAL
4  Alpha           AS REAL
5
6  VARIABLE
7  HoldUp          AS Mass
8  FlowIn, FlowOut AS MassFlowrate
9  Height         AS Length
10
11 EQUATION
12 |
13 # Mass balance
14 $HoldUp = FlowIn - FlowOut ;
15
16 # Relation between liquid level and holdup
17 Holdup = CrossSectionalArea * Height * Density ;
18
19 # Relation between pressure drop and flow
20 FlowOut = Alpha * SQRT ( Height ) ;
21
22

```

Figure 12: The gPROMS language tab [39].

The “miscellaneous files” entity can be used to implement external files. For example, the enthalpies of formation used in the calculation of energy balances can be provided by thermodynamic look-up tables (Figure 13). Using lookup tables can significantly shorten the simulation time since no interfaces or external tools are needed. Data falling in between the intervals established in the lookup tables can be extrapolated [10-12, 39].

1 Data	range:	Energy Unit	kJ		Temp. Unit	K	
2 Number	of rows of data:						
3	399						
4 Number	columns of data						
5	138	2	3	4	5	6	7
6 [K]	Fe2O3	Fe3O4	FeO	Fe	C	CaO	MgO
7	20	-717118.92	-653918.16	-270217.81	-1834.80	-1052.77	-637729.58
8	30	-768080.35	-850246.20	-272949.20	-3286.86	-1051.53	-639817.90
9	40	-792850.76	-946223.38	-274062.60	-3908.63	-1049.05	-640748.75
10	50	-807146.53	-1002108.16	-274528.55	-4196.99	-1044.92	-641209.91
11	60	-816206.37	-1037985.61	-274670.54	-4317.57	-1038.90	-641430.79
12	70	-822275.35	-1062462.71	-274627.20	-4341.35	-1030.77	-641509.83
13	80	-826475.95	-1079842.16	-274467.83	-4303.83	-1020.35	-641496.40
14	90	-829431.68	-1092513.61	-274230.95	-4224.72	-1007.47	-641417.99
15	100	-831516.61	-1101910.24	-273939.63	-4115.88	-991.95	-641291.22
16	110	-832968.73	-1108943.47	-273608.56	-3984.82	-973.65	-641126.73
17	120	-833946.64	-1114220.38	-273247.54	-3836.59	-952.57	-640931.71
18	130	-834560.10	-1118160.79	-272863.34	-3674.65	-928.46	-640711.20
19	140	-834887.48	-1121064.07	-272460.78	-3501.49	-901.14	-640468.87
20	150	-834986.21	-1123149.38	-272043.40	-3318.95	-870.49	-640207.46
21	160	-834899.31	-1124580.64	-271613.86	-3128.39	-836.42	-639929.11
22	170	-834659.67	-1125482.86	-271174.17	-2930.87	-798.87	-639635.49
23	180	-834292.81	-1125952.91	-270725.91	-2727.20	-757.78	-639327.96

Figure 13: Look-up table for enthalpies of formation.

The process entity (Figure 14) is used to assign values for the parameters required in the simulation. It is also used to perform sensitivity analysis as well as special initialisation and optimization routines. The inputs declared in this entity include temperature, pressure, flow rate and composition of streams [10-12, 39].

```

1 #-----
2 # Process Description
3 #-----
4
5 UNIT # Equipment items
6   T101 AS BufferTank
7
8 SET # Parameter values
9   T101.CrossSectionalArea := 1 ; # m2
10  T101.Density := 1000 ; # kg/m3
11  T101.Alpha := 10 ;
12
13 ASSIGN # Degrees of freedom
14  T101.FlowIn := 20 ;
15
16 INITIAL # Initial conditions
17  T101.Height = 2.1 ;
18
19 SOLUTIONPARAMETERS
20  REPORTINGINTERVAL := 60 ;
21
22
23 SCHEDULE # Operating procedure
24  CONTINUE FOR 1800
25
  
```

Figure 14: The process entity [39].

The modelling and simulation process in gPROMS ModelBuilder generally follows these steps: First, variable- and connection types are defined. Then, the design of the flow sheet model, often consisting of several sub-models and their connections, takes place. Finally, the simulation is run, solving the models using input parameters from the process entity. The simulation results can then be viewed directly in the ModelBuilder program or exported to different software, for example MS Excel or MATLAB using build-in interfaces [10-12, 39].

2.2.2 HSC Chemistry[®]

HSC chemistry by Metso Outotec [41] is a static simulation software frequently used in the chemical and mineral processing industry. HSC stands for H (enthalpy), S (entropy) and Cp (heat capacity). It enables the calculation of thermodynamic data for chemical systems at equilibrium conditions [41].

The Reaction Equations Module of HSC chemistry (version 10.0, Figure 15) was used to verify the data of the thermodynamic lookup tables (Figure 13) used in gPROMS ModelBuilder and to calculate values for the enthalpy of chemical reactions for the energy balances of the model validation [10, 41].

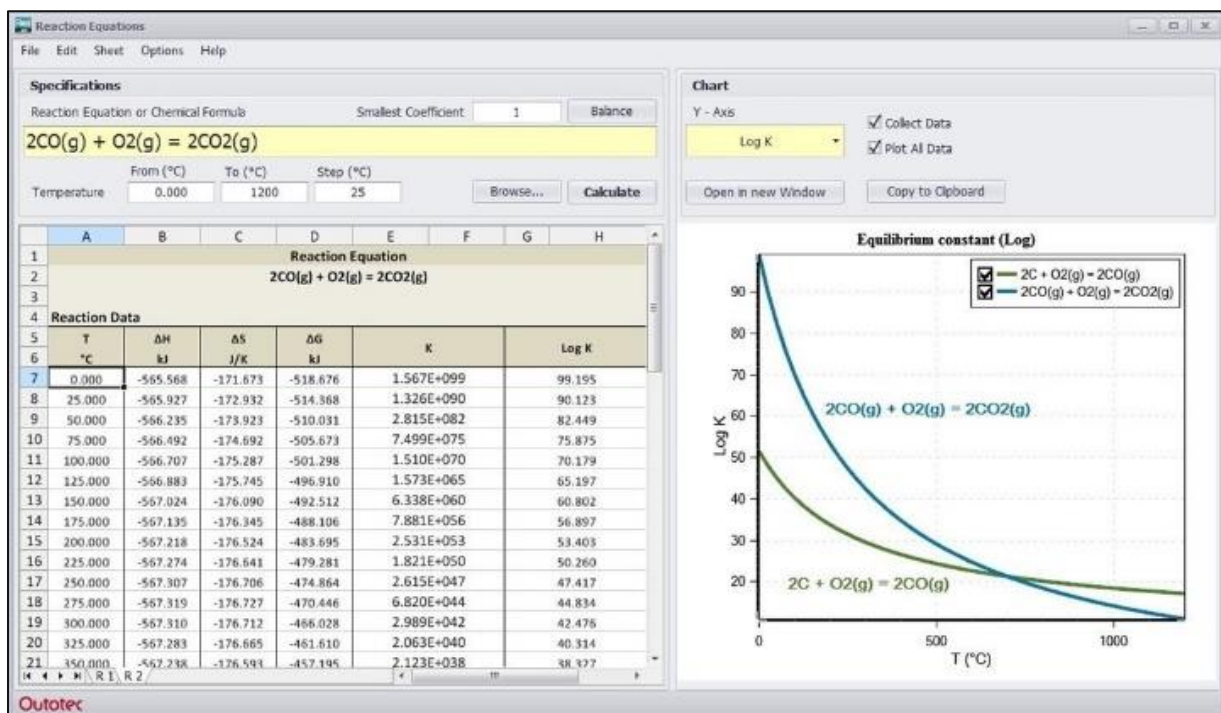


Figure 15: Reaction Equations Module of HSC chemistry [41].

2.2.3 State of the Art EAF Modelling

Since the EAF route is the second most widely used steelmaking route in the world and the most important process for steel recycling, it is subject to extensive scientific research and investigations. Compared to other industrial processes, many important parameters of the EAF process, like the metal and slag temperatures or the metal, slag and off-gas composition in the vessel are difficult to measure because of extreme conditions and nonideal mixing. Plant trials are very expensive and often accompanied by safety concerns, which leaves modelling and process simulation as the tool of choice [8, 9, 42].

The EAF process is highly depending on operator decisions, creating a need for both online models to support the operator in real time as well as offline models to better understand and optimise the EAF and plan future operations. Online models need to have a short execution time and are thus limited in their scope while offline models can take into account more complex physical and chemical phenomena but will require more runtime [8, 9, 42].

In contrast to the well understood blast furnace and converter route, the range and fluctuation of EAF process parameters is significantly higher and the accuracy of the available models is lower. Electrical steelmaking is historically younger and generally has more variation in input materials and in the produced steel grade than oxygen steelmaking in the BOF. In the EAF process, batches tend to have lower volumes and every batch can potentially use different input materials and produce a different steel grade if needed. The multitude of existing EAF models can be divided into 3 categories [8, 9]:

Statistical models

Statistical models, also called data-driven models, are used to predict a specific process parameter based on input data. In case of EAF modelling, the parameter being predicted is usually the electric energy demand. This is no simple task, since it can vary widely depending on the EAF type, melting practice, input material, the produced steel grade, unplanned delays and other factors, some of which are summarised in Figure 16 [8, 9, 43].

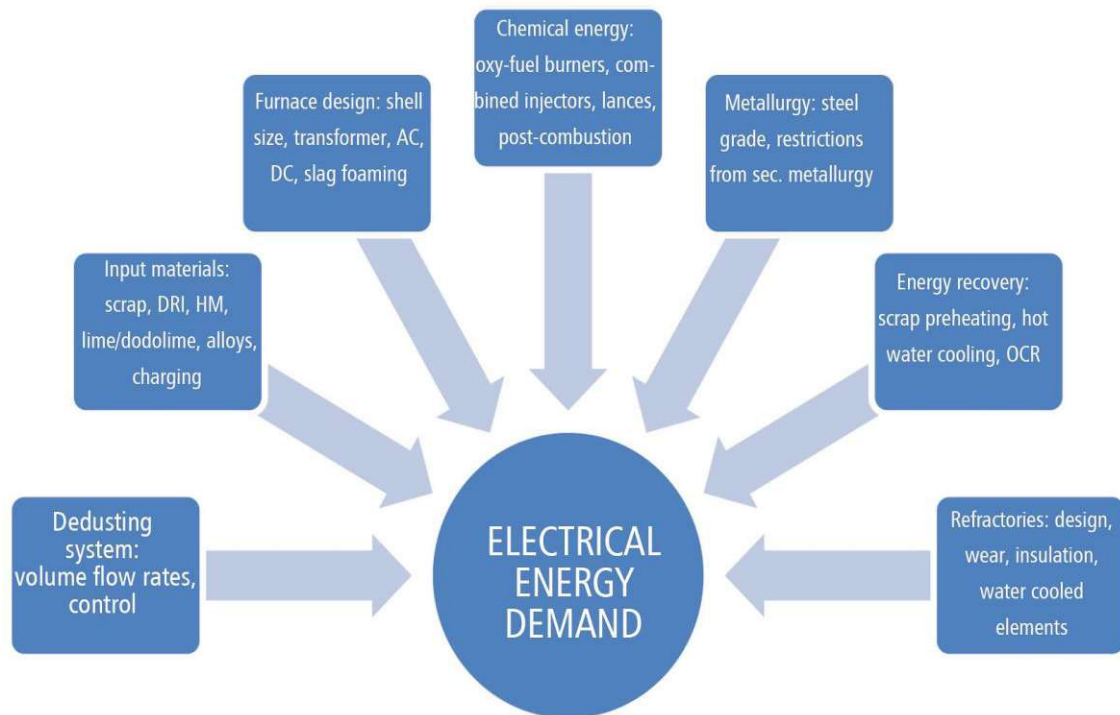


Figure 16: Parameters influencing the electrical energy demand of an EAF [43].

Compared to the other model types, they are relatively easy to develop, since it is not necessary to describe all the underlying chemical and physical phenomena. They can be further divided by the modelling approach into linear and non-linear models. Linear models use methods like multiple linear- or partial least square regression while non-linear models use artificial or deep neural networks, Gaussian process regression or other non-linear methods [44].

According to scientific literature, the Köhle model [45, 46] still represents the most used data-driven approach for energy demand prediction [43]. It was originally developed in 1992 based on 14 EAF's (eq. (13), [45]) and later expanded to include post combustion as well as alternative ferrous inputs like DRI or hot metal (eq. (14), [46]). The expanded model was based on over 5000 single heats of 5 different EAFs and data for monthly averages over the course of 3 years for an individual furnace [18, 47]. Another common model is the Adams model, which also takes oil and liquefied petrol gas as fuel into account [12, 48].

While the Köhle model is based on linear regression, a nonlinear transformation on some variables through dividing them by the tap weight is performed. Unfortunately, the original publications of the model did not include statistical evaluations of the model quality such as by means of an ANOVA [32, 43].

$$\frac{W_R}{\text{kWh/t}} = 300 + 900 \left(\frac{G_E}{G_A} - 1 \right) + 1600 \frac{G_Z}{G_A} + 0.7 (T_A - 1600) + 0.85 (t_S + t_N) - 8 M_G - 4.3 M_L \quad (13)$$

$$\frac{W_R}{\text{kWh/t}} = 375 + 400 \left(\frac{G_E}{G_A} - 1 \right) + 80 \frac{G_{\text{DRI/HBI}}}{G_A} - 50 \frac{G_{\text{Shr}}}{G_A} - 350 \frac{G_{\text{HM}}}{G_A} + 1000 \frac{G_Z}{G_A} + 0.3 (T_A - 1600) + 1 (t_S + t_N) - 8 M_G - 4.3 M_L - 2.8 M_N + NV \times W_V \quad (14)$$

W_R	Specific electrical energy demand (kWh/t)	T_A	Tapping temperature (°C)
G_E	Mass of all ferrous input materials (t)	t_S	Power on (min)
$G_{\text{DRI/HBI}}$	Mass of DRI or HBI input (t)	t_N	Power off (min)
G_{HM}	Mass of Hot Metal input (t)	M_G	Specific burner gas (m ³ /t)
G_{Shr}	Mass of shredder input (t)	M_L	Specific lanced oxygen (m ³ /t)
G_A	Furnace tap weight (t)	M_N	Specific post-combustion oxygen (m ³ /t)
G_Z	Mass of slag formers (t)	W_V	Specific energy losses (kWh/t)
		NV	Furnace specific factor

An advantage of the Köhle model is the relatively easy interpretation of the results. The coefficients also indicate the effectiveness of conversions between electrical and chemical energy which occur during the EAF process. As an example, the factor for the natural gas input is assigned the value 8, which can be compared to the specific energy for natural gas combustion, which is about 9.4 kWh/m³. This makes the Köhle Model a hybrid empirical-theoretical one [32, 43].

Despite being old, the Köhle model is still widely used today. A recent paper by Reimann et. al. used data from more than 21.000 heats from five EAF's to test the applicability of the Köhle model, as well as a non-linear regression model and a Gaussian process regression model to predict the electric energy demand [8].

A comprehensive review of statistical EAF models predicting the electrical energy demand has been recently published by Carlsson et al. [42]. The accuracy and applicability of a statistical model depends to a large degree on the range and quality of the underlying data and the applicability of the models to processes outside the range of their training data is generally limited [9, 23].

Computational Fluid Dynamics (CFD) models

CFD models are the most detailed and most analytical type of EAF models. Their goal is to describe all relevant phenomena of the EAF process, including heat and mass transfer, chemical reactions, and fluid as well as electromagnetic flows with spatial, three-dimensional resolution. The fact that many of these phenomena are of a turbulent, friction dependant, non-isothermal nature and take place in multiple phases at a rapid pace make this modelling approach the most challenging. The complexity of the models results in long computational times, even when using high-end hardware, making CFD models unsuitable for online modelling at the present time. Current CFD models found in the scientific literature focus on individual components like the off-gas elbow, refractory lining, the electric arcs, oxy-fuel burners etc., or on parts of the process like the melt phase or post combustion. An example is shown in Figure 17, where the displacement of protective foamy slag (red) from the electrodes by oxygen jets (blue isosurfaces) is depicted. This replacement can cause overheating of the refractory lining and cooling panels [9, 23, 49].

While it is already possible to simulate specific phases or components in great detail, a holistic CFD model of the EAF process calculating all phenomena simultaneously is yet to be developed [9, 23].

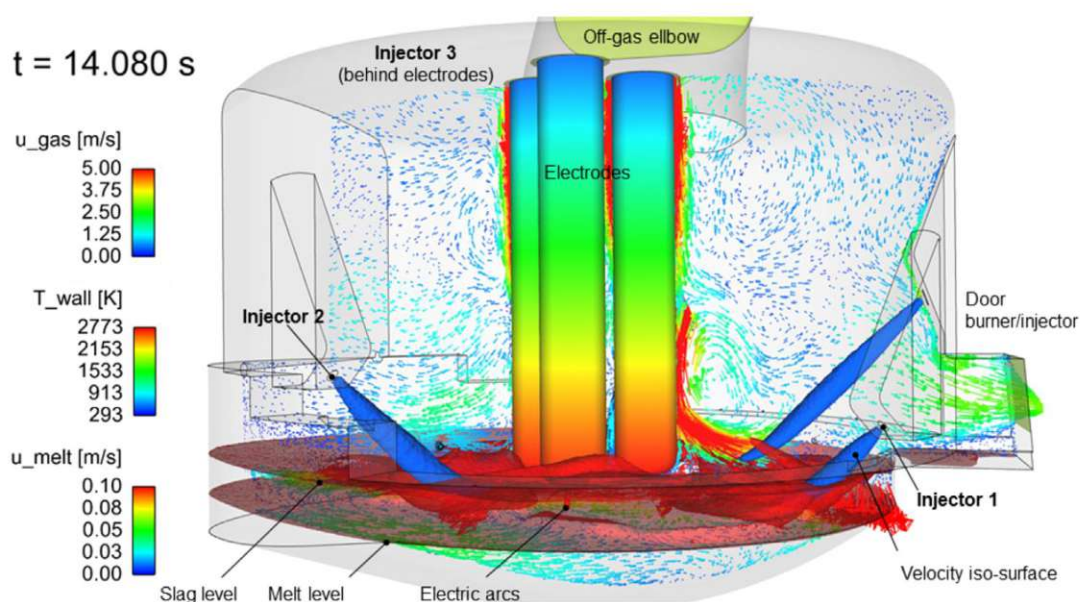


Figure 17: CFD simulation of a 120 t AC EAF, showing velocity and temperature distributions [23, 49].

Process models

In terms of complexity, process models are located in between the highly complex CFD models and the rather simple statistical models. While CFD models have a high spatial resolution, process models often divide the EAF into simplified zones (Figure 18). Phenomena like mass and energy transfer between the zones or chemical reactions inside a zone are estimated using simple empirical approaches like distributions and equilibrium constants or more sophisticated thermodynamic methods like Gibbs free energy minimization [9].

The individual zones are often represented by sub-models for which equilibrium conditions are assumed. Temperature and composition of each zone can be calculated using mass and energy balances and the zones are connected by energy, mass and information streams. In regard to time dependency, process models can be static or dynamic, and the computational time is often fast enough for online applications. While many models use the furnace shell as their system boundary, some also include secondary equipment like scrap preheating units, off-gas treatment or even a ladle furnace for secondary metallurgy. [9, 50].

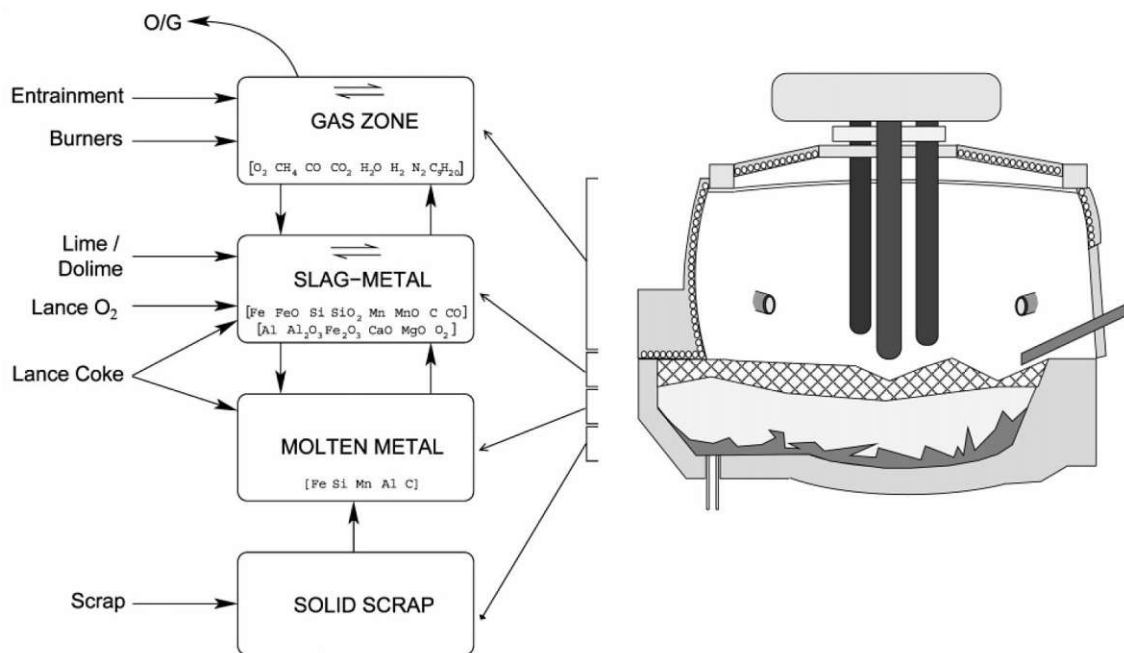


Figure 18: Schematic of EAF model using four zones. For the slag and gas zone, equilibrium conditions are assumed [51].

The heat transfer inside the EAF can be modelled by assuming isothermal phases and defining heat flows for in- and outputs, for example by setting an off-gas or hot metal temperature, or by assuming heat transfer coefficients and specific surface areas. Some models also take radiative heat transfer into account. The EAF process is often split by using sub-models for the melting and the refining phase [9, 52].

The melting phase cannot be described by heat flows alone, since it depends on the shape, density, and composition of the ferrous inputs as well as flow conditions inside the metal bath. All those parameters can vary from batch to batch. A simple approach to model the meltdown is to assume fixed melt rates for each kind of ferrous input by calculating the energy used to heat the inputs as well as the energy needed for the phase transition from solid to liquid. More sophisticated models divide the scrap zone into different sections and take parameters like the change in geometry and composition of the ferrous input during the melting process into account using differential equations [9].

A big challenge in simulating the refining phase is the accurate representation of the equilibrium between metal and slag phase. Because of suboptimal mixing conditions in the furnace, the reactions are often limited by kinetic factors. A simple approach to solve phase equilibria during the flat bath phase is the use of equilibrium constants while more complex models use Gibbs energy minimization, which can also be used for description of the equilibrium conditions in the gas phase for the freeboard zone. Another important metal–slag interaction is the creation of the foaming slag. A widespread approach is the use of a foaming index, to describe the relation between slag density and CO generation rate [9].

The validation of complex process models is often problematic. According to the scientific literature, the quality of process models is limited by the availability of accurate data. Especially measurements of the off-gases, noise and vibrations, as well as the evolution of the melting phase would be beneficial. To obtain this data, special measurement campaigns are necessary and not all the results from industrial plant trial are shared with the scientific community [9].

2.3 Statistics

One question that often arises in process simulation is how an important variable depends on other variables. For EAF modelling, the electric energy consumption is such a variable of high interest. In this work, the statistical tool of Multiple Linear Regression (MLR) will be utilized to develop and validate models to predict the electric energy consumption needed to produce one ton of crude steel based on the material inputs. The principles and basic equations of MLR, which is one of the most commonly used methodology in statistics, will be briefly summarized in the following chapters [53].

2.3.1 Multiple Linear Regression

The dependency of a target variable on a single input variable is often immediately visible in a simple scatterplot. However, this fast graphical method is no longer sufficient to describe the relationship between a target variable and several input variables. This is when MLR is used [53, 54]. The statistical relation between the observed values y_i and the predictor variables $x_{i,k}$ is described by eq. (15) [53].

$$y_i = \beta_0 + \beta_1 x_{i,1} + \dots + \beta_k x_{i,k} + \epsilon_i \quad (15)$$

Where β_0 represents the intercept and each β_k represents the partial regression coefficient or slope for x_k . The slope represents the mean change of the observed values when x_k is increased while the other input variables remain unchanged. The index i refers to the i^{th} unit in the population (in this case an individual EAF heat), k is the number of predictor or independent variables, and ϵ_i is the random error term, also called residual. The model is fitted to a given data set by estimating the partial regression coefficients in a way that minimizes the sum of squared errors (SS) for a given sample. The estimate for the regression coefficients β_0 is given as b_0 . A predicted value \hat{y}_i is calculated via eq. (16) and the residual term, representing the difference between an observed and a predicted [54] value is calculated according to eq. (17) [54-56].

$$\hat{y}_i = b_0 + b_1 x_{i,1} + \dots + b_k x_{i,k} \quad (16)$$

$$\epsilon_i = y_i - \hat{y}_i \quad (17)$$

2.3.2 Regression Statistics

The MLR model assumes that the output variable is a linear combination of the regression coefficients and the input variables. The coefficient of determination (R^2) quantifies the degree linear relation between y_i and \hat{y}_i . R^2 can have values between 0 to 1, with 1 indicating perfect linear correlation. R^2 is calculated according to eq. (18)-(20) [54, 57].

$$R^2 = \frac{SS_{\text{reg}}}{SS_{\text{tot}}} \quad (18)$$

with

$$SS_{\text{reg}} = \sum (y_i - \bar{y}_i)^2 \quad (19)$$

and

$$SS_{\text{tot}} = \sum (y_i - \bar{y}_i)^2 \quad (20)$$

Since R^2 values automatically increase when more regression coefficients are added, even if the coefficients are unrelated to the output variable, the adjusted R^2 (eq. (21)) is used. This facilitates the comparison of models using a different number of input variables (n) to predict the same response variable [54, 57].

$$\text{adjusted } R^2 = 1 - \left(\frac{n-1}{n-(k+1)} \right) (1 - R^2) \quad (21)$$

Another important parameter is the regression standard error (RSE), which indicates how “wrong” the regression model is on average using the unit of the target variable (eq. (22), (23)) [53, 54].

$$RSE = \sqrt{\frac{SS_{\text{res}}}{(n-k)}} \quad (22)$$

with

$$SS_{\text{res}} = \sum (y_i - \hat{y}_i)^2 \quad (23)$$

Apart from a linear correlation between the input and output variable, other important prerequisites for a MLR are the normal distribution and homoscedasticity of the residuals. The normal distribution can be visually checked by using a histograms plot or mathematically using tests like the Kolmogorov-Smirnov test [58]. Homoscedasticity can be determined by visually checking a standardised residual plot [58].

In addition, the independent variables should be checked for multicollinearities. The term multicollinearity means that one input variable of the MLR model can be accurately predicted from other input variables. One method to check for multicollinearities is by calculating the variance inflation factor (VIF) by eq. (24) [55].

$$\text{VIF} = \frac{1}{1 - R_i^2} \quad (24)$$

With R_i^2 representing the unadjusted coefficient of determination when an MLR is performed for the i th input variable from the remaining variables. If the VIF indicates significant correlations, the tested variables should be removed from the regression or combined, for example by means of a linear transformation [54, 55].

2.3.3 Analysis of Variance (ANOVA)

To interpretate the quality of a MLR, an analysis of variance is needed. The F-statistic tests the null hypothesis which states that all slope parameters b_i except for b_0 are 0. An F-value is calculated as shown in Tab.3. An associated P-value representing the probability of the null hypothesis can be determined from the F-distribution function (eq.(25)) Inputs for the F-distribution are the F-value (F_{qv}) as well as the numerators (df_q) and denominators degrees of freedom (df_v) [54, 56].

$$\text{significance F} = p(F_{qv}, df_q, df_v) \quad (25)$$

Tabulated numerical values of p can be found in various texts on statistics. It can also be calculated using the corresponding statistical function. In this work, the p-values were calculated using the FDIST function of MS Excel [57]. A high F-value or low P-value imply a statistically significant linear relation between the input and the output variable [53, 56].

Tab. 3: Statistic Parameters for the ANOVA of the linear Regression for the regression mode. n represents the size of the sample and k the number of predictor variables, y_i is the observed value for i , \hat{y}_i is the predicted value for i , and \bar{y}_i the mean value [57].

	df	SS	MS	F	Significance F
Regression	k	$SS_{reg} = \sum (\hat{y}_i - \bar{y})^2$	$MS_{reg} = \frac{SS_{reg}}{k}$	$F = \frac{MS_{reg}}{MS_{res}}$	$P = \text{FDIST}(F, k - 1, n - k)$
Residual	$n - k + 1$	$SS_{res} = \sum (y_i - \hat{y}_i)^2$	$MS_{res} = \frac{SS_{res}}{(n - (k + 1))}$		
Total	$n - 1$	$SS_{tot} = \sum (y_i - \bar{y})^2$			
$SS_{reg} \dots\dots$		Sum of squared errors of the regression model			
$SS_{res} \dots\dots$		Sum of squared errors of the residual			
$SS_{tot} \dots\dots$		Total sum of squared errors			
$MS_{reg} \dots\dots$		Mean square (variance) of the regression model			
$MS_{res} \dots\dots$		Mean square (variance) of the residual			
F.....		F statistic value			
P.....		P statistic value			
FDIST....		F distribution function			

3 Development of the EAF Process Model

This section will cover the expansions of the EAF model that were made during the course of this work. Since no documentation of the model was available prior, this section will also serve as a documentation of the model's structure and capacities. It will also cover how the simulation results used for the validation were calculated.

The most important additions to the model as part of this work, were the statistical energy demand sub-model (section 3.4), the implementation of a case selector for the species distributions (section 3.2) and the reworking of the port structure (section 3.1) as well as the initialisation procedure (section 3.5). A basic flowsheet setup for the EAF model with sources and sinks for the in- and outputs is depicted in Figure 19.

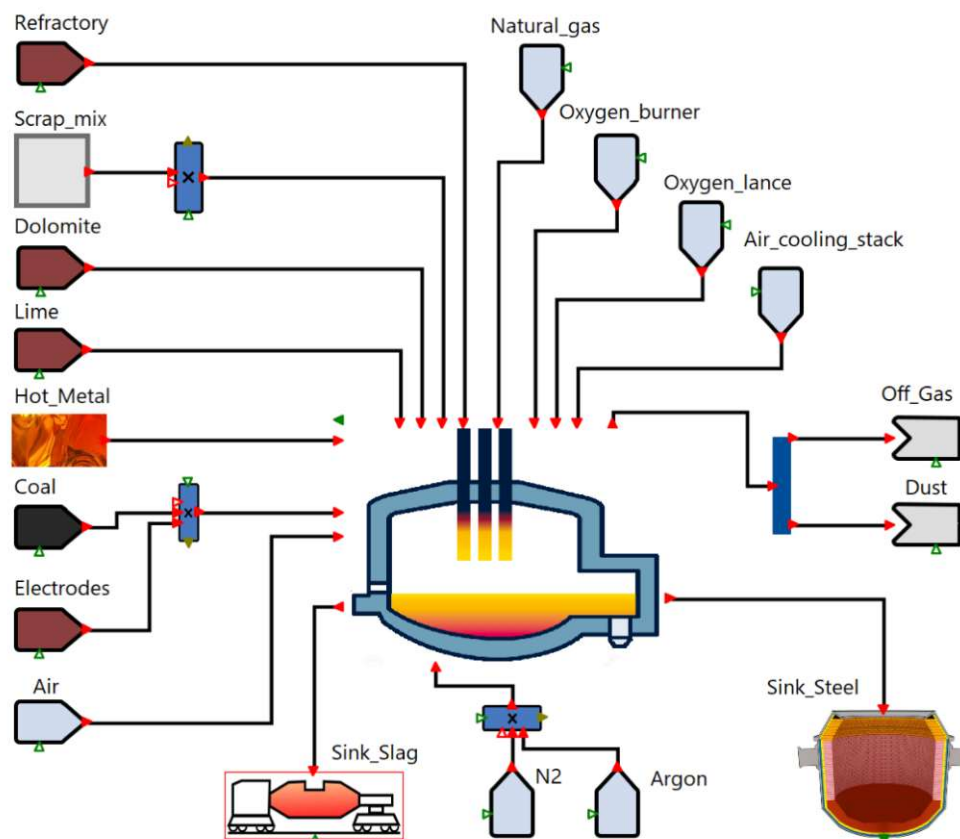


Figure 19: Basic flowsheet including sources and sinks of the EAF process model.

The foundation for the EAF process model is the simulation platform for iron and steelmaking developed by Primetals Technologies Austria GmbH in cooperation with voestalpine and TU Wien [10, 11, 59]. Many existing unit operation models like splitters,

mixers, material sources and sinks were available for use. Physical properties for all included chemical compounds, including molecular weights and thermodynamic data like enthalpies of reaction, formation and dissolution were already implemented in the form of sub-models or lookup tables and validated in previous works [59]. The models and sub-models are connected via standardised connection types to transfer scalar values like temperature, and pressure as well as vectors like the chemical composition of a stream. This enables the creation of complex flowsheets, and the developed model can thus be used for standalone simulations or as part of complete iron and steelmaking process routes. The EAF model was originally based on a basic oxygen furnace model developed by Almpanis-Lekkas [10]. It was later expanded by Spanlang [unpublished] and can be classified as a steady-state process model using an equation-oriented solver.

3.1 Model Structure

The EAF model consists of multiple layers. A simplified topology of the top layer can be seen in Figure 20. The in- and output ports are represented by arrows. Each box corresponds to a sub-model, with some sub-models also having multiple layers [10]. Section 3.2 and 3.3 include a detailed description of the cooling stack and the black box sub-model. The different stream colours represent different species sets with different components and different thermodynamic properties.

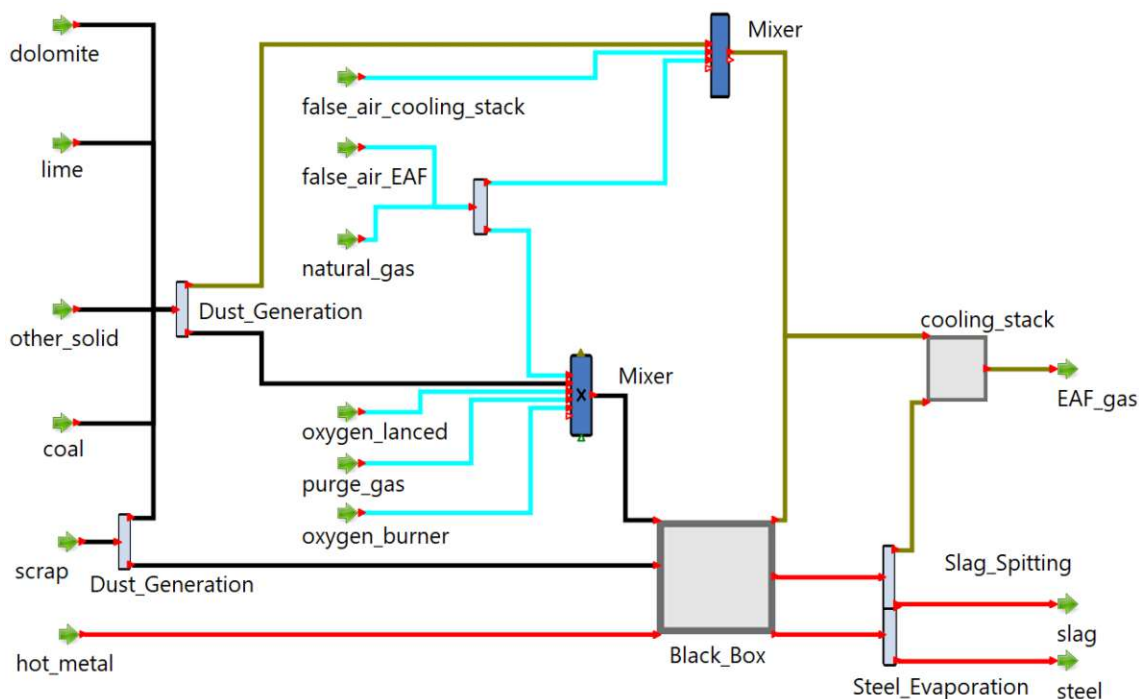


Figure 20: Top layer topology of the Electric Arc Furnace model, simplified.

On the left side, the ports for the input of dolomite, lime, scrap, coal and other solids can be seen. The “other_solids” input port is used for the furnace refractory material and the coal input includes charged and injected coal as well as electrode consumption. The scrap port can be used for all solid ferrous inputs like GPI, hot and cold DRI, solid slag or ferroalloys. The solid inputs are separated by dust splitters using a fixed split factor for each port based on empirical information. The created dust is transported to the cooling stack mixer while the rest of the solid inputs is transported to the main mixer and mixed with the gaseous inputs [10].

The gaseous inputs include false air, natural gas, lanced and burner O₂ as well as Ar and N₂ as purge gas for bottom stirring. Parts of the air and natural gas are split and used for the post combustion, for example to represent a post combustion burner or to represent air ingress through gaps.

The hot metal port is used for liquid ferrous inputs like hot metal or liquid slag. The output of the main mixer and the hot metal input is transferred to the black box [10].

The black box model represents the furnace vessel and the off-gas elbow up to the air gap before the dedusting system. It is the core of the EAF process model where all the metallurgic reactions take place, creating crude steel, slag as well as off-gas. The chemical and physical processes inside the black box will be described in section 3.2. Evaporation of steel elements is implemented by using a splitter inside the black box and can be set individually for each element. Together with the created off-gas from the melting and refining processes, the steel vapor is transported to the cooling stack mixer. The off-gas output port of the black box represents part of the off-gas elbow right before the gap between the off-gas elbow and the dedusting system [10].

To simulate steel and slag spitting as well as the small degree of steel-slag mixing, a splitter cascade was implemented after the hot metal and slag outputs of the black box. The extent of those phenomena can be set in the user interface. Droplets created from the steel and slag spitting are transported from the splitter cascade to the cooling stack, while the steel and slag are transferred to the output ports of the model [10].

The cooling stack handles post combustion of CO and H₂. The needed volume of false air for the post combustion is determined based on the oxygen, CO and H₂ content of the black box off-gas as well as a set lambda factor. Reactions for dust oxidation as well as a water-gas shift reaction (see eq.(45)) are optional [10].

Mass and energy balances for all sub-models as well as the whole model are closed and based on the eq. (26) and (28) [10].

$$\sum_{e,\text{in}} \dot{n}_{e,\text{in}} = \sum_{e,\text{out}} \dot{n}_{e,\text{out}} \quad (26)$$

$$\sum_{i,\text{in}} \left(sp_{i,e} \cdot \frac{\dot{m}_{i,\text{in}}}{MW_i} \cdot c_{i,\text{in}} \right) = \sum_{i,\text{out}} \left(sp_{i,e} \cdot \frac{\dot{m}_{i,\text{out}}}{MW_i} \cdot c_{i,\text{out}} \right)$$

The mass balance seen in eq. (26) is calculated on a molar basis for each chemical element e , meaning that the total molar input for each element is equal to its total molar output. Input streams are denoted with *in* and output streams with *out*, i representing the system components or “species” (a chemical compound). The number of elements found in a component is indicated by the species incidence $sp_{i,e}$. The mass flow of a stream in kg/s is represented by \dot{m}_i , c_i represents the mass fraction of component i in the stream and $\dot{n}_{i,\text{in}}$ is the molar flow of component i . The complete mass balance of the EAF model is represented by eq. (27) [10].

$$\sum \dot{n}_{scrap} + \dot{n}_{lime} + \dot{n}_{dolomite} + \dot{n}_{coal} + \dot{n}_{other.solides} + \dot{n}_{hot.metal} = \sum \dot{n}_{steel} + \dot{n}_{slag} + \dot{n}_{off.gas} \quad (27)$$

The energy balance seen in eq. (28) is calculated using the specific enthalpies of formation for all in and outputs [10].

$$\sum_{i,\text{in}} (\dot{m}_{i,\text{in}} \cdot c_{i,\text{in}} \cdot h_{T_{\text{in}}}^0(i)) = \sum_{i,\text{out}} (\dot{m}_{i,\text{out}} \cdot c_{i,\text{out}} \cdot h_{T_{\text{out}}}^0(i)) \quad (28)$$

$h_T^0(i)$ is the mass specific enthalpy of formation at the temperature T for the component i from the elements in their standard state under constant pressure in J/kg. T_{in} and T_{out} are the in- and outlet temperatures of the component in K [10].

The inlet flow rates can be set or calculated based on specific criteria using a reverse calculation regime. For example, either the steel productivity is set and the ferrous input flow to reach this production is calculated or the ferrous input stream is set and the

resulting steel productivity is determined. The flows and their calculation criteria are shown in Tab. 4 [10].

Tab. 4: Inlet flow calculation criteria of the EAF model. The formulas for the criteria can be found in Tab. 7 and Eq. (31) [10].

Flow	Criteria
Ferrous inputs (kg/h)	Steel productivity (kg/h)
Lime (kg/h)	Basicity (-)
Dolomite (kg/h)	MgO composition slag (w%)
Coal (kg/h)	PCD (Post Combustion Degree) at mouth (%)
Oxygen (Nm ³ /h)	O ₂ content at mouth (v%)
Air for post combustion (Nm ³ /h)	λ cooling stack (-)

3.2 Black Box

The Black box sub-model is the core of the EAF process model. It includes the chemical and physical phenomena needed to represent the process, and turns the hot metal, solid ferrous, and other inputs streams into the steel, slag, and off-gas output streams. The important chemical and physical phenomena are implemented using a combination of outlet specific elemental assignments, empirical distribution factors, generic reaction degrees and equilibrium constants. An energy balance is calculated inside the black box to determine the electrical energy consumption and the heat loss for the whole process model [10].

Elemental assignments

The elemental assignments are a way to model the complex three phase reactions between the liquid steel, the liquid and solid particles in the slag as well as the gas phase inside the furnace. To facilitate this, incoming mass streams need to be split into molecular and elemental molar flows. The steps of this calculation are explained in Tab. 5. All element assignments are shown in Tab. 6 [10].

The elemental assignment defines not only the output streams of the elements but also the chemical compound in which the elements is present inside a phase. For example, phosphorus is present in the steel phase as P and in the slag phase as the oxide P₂O₅. The “rest” species is used to cover all solids species which are not defined in the composition analysis [11].

Tab. 5: Calculation procedure for the elemental assignment and distribution [10].

Step	Procedure
	Transform the inlet mass flows to molar flows for each component
1	using the molar mass
2	Calculate the elemental molar flow rates using the species incidences Assign or distribute the elements between steel, slag and off-gas
3	phase using equations or empirical coefficients
4	Reverse step 2 to get the outlet molar flow rate
5	Reverse step 1 to get the outlet mass flow rate

Tab. 6: Elemental assignment for the Black Box [10].

Element	Off-Gas	Steel	Slag
H	H ₂ O, H ₂	H	-
C	CO, CO ₂	C	-
N	N ₂	N	-
Ar	Ar	-	-
O	O, CO, CO ₂ , H ₂ O	O	FeO, CaO, MgO, SiO ₂ , Al ₂ O ₃ , MnO, TiO ₂ , Na ₂ O, K ₂ O
Na	-	-	Na ₂ O
Mg	-	-	MgO
Al	-	-	Al ₂ O ₃
Si	-	Si	SiO ₂
P	-	P	P ₂ O ₅
S	-	S	S
Cr	-	Cr	Cr ₂ O ₃
Cu	-	Cu	-
Mo	-	Mo	-
Ni	-	Ni	-
Sn	-	Sn	-
Zn	-	Zn	-
Pb	-	Pb	-
V	-	V	-
K	-	-	K ₂ O
Ca	-	-	CaO
Ti	-	-	TiO ₂
Mn	-	Mn	MnO
Fe	-	Fe	FeO Fe ₂ O ₃
Rest	-	Rest	Rest

Distributions and compositions specifications

Apart from the element assignment, several distributions and composition specifications regulate the partition of elements to components and zones. For example, the phosphorus distribution P_{Dist} defines what portion of phosphorus is assigned to the steel and what portion is assigned to the slag phase. A list of all distributions and specifications regarding compositions is provided in Tab. 7. w_i represents the mass- and v_i the volume-composition of species i in a phase (w% or vol%). Not all specifications have to be set. For example, the distributions for P, Cr, Mn and S can be set or calculated using a distributions case selector. The formulas are based on previous works and scientific literature [10, 60].

Tab. 7: Distributions and compositions specifications for of the black box model [10].

Phase		Specification	
Steel	Steel analysis (w%): Gas dissolution (w%):	W_C, W_{Si}, W_{Rest} W_H, W_N, W_O	
	Phosphorus distribution (-)	$P_{Dist} = \left(\frac{W_{P,Slag}}{W_{P,Steel}} \right)$	(29)
	Sulphur distribution (-)	$S_{Dist} = \left(\frac{W_{S,Slag}}{W_{S,Steel}} \right)$	(30)
	Manganese distribution (-)	$Mn_{Dist} = \left(\frac{W_{Mn,Slag}}{W_{Mn,Steel}} \right)$	(31)
	Chrome distribution (-)	$Cr_{Dist} = \left(\frac{W_{Cr,Slag}}{W_{Cr,Steel}} \right)$	(32)
	Steel in slag (w%): Slag analysis (w%):	W_{Steel} W_{FeO}, W_{MgO}	
Slag	Basicity (-)	$B_2 = \frac{W_{CaO,Slag}}{W_{SiO_2,Slag}}$	(33)
		$B_3 = \frac{W_{Cr,Slag} + W_{MgO,Slag}}{W_{SiO_2,Slag}}$	(34)
		$B_4 = \frac{W_{Cr,Slag} + W_{MgO,Slag}}{W_{SiO_2,Slag} + W_{Al_2O_3,Slag}}$	(35)
Gas	Off-gas analysis (vol%)	$V_{H_2O}, V_{H_2}, V_O,$	
	Post Combustion Degree (vol %)	$PCD = \frac{v_{CO_2,Gas} + v_{H_2O,Gas}}{v_{CO_2,Gas} + v_{H_2O,Gas} + v_{CO,Gas} + v_{H_2,Gas}}$	(36)

Distributions case selector

In the old model, distinct values had to be set for all the element distributions. Those values had to be calculated using external metallurgical tools. As part of this work, a case selector was implemented that allows the user to use fixed values for the P, Cr, S and Mn distribution or to calculate the values based on empiric correlations found in the literature [10, 60]. The implemented correlations can be seen in Tab. 8. The model also allows for easy implementation of additional correlations.

While the stability of the case selector was proven during validation, the distribution correlations could not be fully validated, since insufficient plant data regarding the composition of steel and slag during the process was available for this work.

Tab. 8: Distribution correlations used in the case selector [10].

Element	Distribution Correlation
Sulphur	$\frac{w_{S,Slag}}{w_{S,Steel}} = \frac{760 - 60.822 \cdot Ac + 1.8682 \cdot Ac^2 - 0.0201 \cdot Ac^3}{w_{FeO,Slag}} \quad (37)$
	$Ac = w_{SiO_2,Slag} + w_{P_2O_5,Slag} + w_{Al_2O_3,Slag} \quad (38)$
Phosphorus	$\frac{w_{P,Slag}}{w_{P,Steel}} = 79.98 \cdot \frac{w_{CaO,Slag}}{w_{SiO_2,Slag}} - 3.4 \cdot w_{Fe\ total,Slag} \cdot 1.28649 \quad (39)$
	$w_{Fe\ total,Slag} = w_{Fe,Slag} + w_{FeO,Slag} \cdot \frac{MW_{Fe}}{MW_{FeO}} + \quad (40)$
	$w_{Fe_2O_3,Slag} \cdot \frac{2 \cdot MW_{Fe}}{MW_{Fe_2O_3}} \quad (41)$
Chrome	$\frac{w_{Cr,Slag}}{w_{Cr,Steel}} = 10^{\frac{9000}{T_{Steel}} - 4.99 + \log_{10}(w_{FeO,Slag})} \quad (42)$
Manganese	$\frac{w_{Mn,Slag}}{w_{Mn,Steel}} = 6 \cdot \frac{MW_{Mn}}{MW_{MnO}} \cdot \frac{w_{FeO,Slag}}{B^*} \quad (43)$
	$B^* = \frac{w_{CaO,Slag} + 1.4 \cdot w_{MgO,Slag}}{w_{SiO_2,Slag} + 0.84 \cdot w_{P_2O_5,Slag}} \quad (44)$

Water-gas shift reaction

The homogenous water-gas shift reaction (WGSR, eq. (45)) is a reversible, exothermic reaction producing carbon dioxide and gaseous hydrogen from steam and carbon monoxide. At higher temperatures the equilibrium moves to CO and H₂O [61]. *K* is the equilibrium constant. It's written as the fraction of the partial pressures of the reaction products and educts (eq. (46)) [12].

In the black box as well as the cooling stack, the WGSR can be applied to calculate the off-gas composition using equilibrium constants that are functions of the off-gas temperature (*T*, K) as seen in eq. (46) The corresponding parameters were calculated using linear regression based on plant data in previous work [10]. If the WGSR is activated in the GUI, no specification for the H₂O or H₂ content in the off-gas can be set simultaneously.



$$K = \frac{p_{\text{H}_2} \cdot p_{\text{CO}_2}}{p_{\text{H}_2\text{O}} \cdot p_{\text{CO}}} = 10^{(a + b \cdot T + c \cdot T^2 + d \cdot T^3 + e \cdot T^{-1} + f \cdot T^{-2})} \quad (46)$$

$$\begin{array}{lll} a = -2,56803 & b = 0.0006709381 & c = -0.0000001720595, \\ d = 1.856492 \cdot 10^{(-11)} & e = 2196.949 & f = 1697.599 \end{array}$$

Slag FeO to Fe₂O₃ ratio

As seen in Tab. 6, iron can be present as wustite (FeO) or hematite (Fe₂O₃) in the slag. Metallic iron (Fe) can only enter the slag phase after the black box via slag-steel mixing. The ratio of FeO to Fe₂O₃ in the Slag can be set in the GUI according to eq. (47)

$$Fe_{ox \text{ rate,slag}} = \frac{2 \cdot MW_{Fe} \cdot w_{Fe_2O_3,Slag}}{2 \cdot MW_{Fe} \cdot w_{Fe_2O_3,Slag} + MW_{Fe} \cdot w_{FeO,Slag}} \quad (47)$$

Enthalpy of formation and dissolution sub-model

In the method of “total enthalpy” used by default to calculate the energy balance of all sub-models, the enthalpy change from the dissolution of a solid into liquid iron or the evolution from it when slag is formed are not considered (see chapter 2.1.3) [13]. Since the dissolution of the scrap and the slag formation are calculated in the black box model, a sub-model to calculate the energies of dissolution and slag formation was already

implemented, as part of previous work. The calculated enthalpies can then be considered in the energy balance. This approach as well as the used enthalpy data are based on established metallurgical tools provided by Primetals Technologies Austria GmbH. The enthalpy data are assumed to be temperature independent in a range of 1400 to 2000 K [62].

The mass specific enthalpy of slag formation from solution in iron $\Delta_{sf}h(j)$ in kWh/kg for a stream j is calculated according to eq. (48) as the sum of the specific heats of slag formation of all slag forming species i in the stream.

$$\Delta h_{sf}(j) = \sum_i (c_{i,j} \cdot \Delta h_{sf}(i)) \quad (48)$$

$c_{i,j}$ is the mass fraction for the species i in the stream j . The species considered in the slag formation are CaF_2 , CaO , MgO , SiO_2 , MnO , P_2O_5 , Al_2O_3 , Cr_2O_3 , V_2O_3 , TiO_2 , FeO and Fe_2O_3 . The mass specific enthalpy associated with the formation of a solution in iron $\Delta h_{sol}(j)$ (kWh/kg) for a stream j is calculated by the eq. (49) on an elemental basis.

$$\Delta h_{sol}(j) = \sum_{e_s} (c_{e_s,j} \cdot \Delta h_{sol}(e_s)) + \sum_{e_l} (c_{e_l,j} \cdot \Delta h_{sol}(e_l)) \quad (49)$$

$\Delta h_{sol}(e)$ is the mass specific heat of solution for the solid element e_s or the liquid element e_l into iron. If the temperature of stream j is higher than the melting point of the element e , it is considered liquid. Otherwise, the element is considered solid. $c_{e_s,j}$ and $c_{e_l,j}$ are the mass fractions of stream j for elements regarded solid (s) and elements regarded liquid (l). The elements considered in this submodel are H, C, N, O, Al, Si, P, S, Cr, Cu, Mo, Ni, Sn, Pb, V, Ti and Mn.

Mass Balance

The complete mass balance for the Black box model is shown in eq. (50). With \dot{n}_j being the molar flow of the stream j in mol/s, calculated on an elemental or species basis.

$$\sum (\dot{n}_{scrap} + \dot{n}_{other} + \dot{n}_{hot.metal}) = \sum (\dot{n}_{steel} + \dot{n}_{slag} + \dot{n}_{off.gas}) \quad (50)$$

Energy Balance

The energy balance of the black box model is of essential importance, since it is used to calculate the electrical energy demand $\Delta W_{Electric}$ (kWh) as well as the heat loss ΔQ_{Loss} (kWh) for the complete EAF process model. For this reason, the basic energy balance of eq. (28) was modified to include $\Delta W_{Electric}$, ΔQ_{Loss} as well as terms for the slag formation ΔH_{sf} and solutions ΔH_{sol} . The result can be seen in eq. (51) and in more detail in eq. (52). To convert the values of $\Delta W_{Electric}$ and ΔQ_{Loss} into kWh/t steel, which is the standard for EAF energy balances, they need to be divided by the steel productivity (t/h).

$$\sum_{i,in} (\dot{m}_{in} \cdot c_{i,in} \cdot h_{T_{in}}^0(i)) + \Delta W_{Electric} + \Delta H_{sf} + \Delta H_{sol} = \sum_{i,out} (\dot{m}_{out} \cdot c_{i,out} \cdot h_{T_{out}}^0(i)) + \Delta Q_{Loss} \quad (51)$$

$\dot{m}_{i,j}$, is the mass in- or output stream of component i in kg/h and $c_{i,j}$ is the mass fraction of component i in the stream j .

$$\begin{aligned} & \sum_{i,scrap} (\dot{m}_{i,scrap} \cdot c_{i,scrap} \cdot [h_{T_{scrap}}^0(i) + \Delta h_{sol}(i)]) + \\ & \sum_{i,hot.metal} (\dot{m}_{i,hot.metal} \cdot c_{i,hot.metal} \cdot [h_{T_{hot.metal}}^0(i) + \Delta h_{sf}(i) + \Delta h_{sol}(i)]) + \\ & \sum_{i,other} (\dot{m}_{i,other} \cdot c_{i,other} \cdot h_{T_{other}}^0(i)) + \Delta W_{Electric} = \\ & \sum_{i,steel} (\dot{m}_{i,steel} \cdot c_{i,steel} \cdot [h_{T_{i,steel}}^0(i) + \Delta h_{sol}(i)]) + \\ & \sum_{i,slag} (\dot{m}_{i,slag} \cdot c_{i,slag} \cdot [h_{T_{i,slag}}^0(i) + \Delta h_{sf}(i) + \Delta h_{sol}(i)]) + \\ & \sum_{i,off.gas} (\dot{m}_{i,off.gas} \cdot c_{i,off.gas} \cdot h_{T_{off.gas}}^0(i)) + \Delta Q_{Loss} \end{aligned} \quad (52)$$

As part of this work, a case selector was implemented for the calculation of $\Delta W_{Electric}$ and ΔQ_{Loss} . If case 1 is selected, one of the two is set and the other one is calculated by closing eq. (52). If case 2 is selected, $\Delta W_{Electric}$ is calculated based on input streams by the energy demand submodel (see chapter 3.4) and ΔQ_{Loss} is calculated by closing eq. (52). Another case selector can turn the calculation of ΔH_{sf} and ΔH_{sol} on and off. In case 1 ΔH_{sf} and ΔH_{sol} are calculated using the formation and dissolution sub-model and in case 2 they are set to 0.

Energy Calculations for model validation

For the validation of the EAF model, the results of the energy balance have to be compared with the results of other models or results from the scientific literature. This section will explain what output values are shown in the model validation and how they were calculated. The calculation of the terms used in the comparison of the black box energy balance and a typical EAF energy balance can be seen in tab. (Tab. 10). The reference point for the calculation of the stream enthalpies, is set at 298 K and 1 atm.

Since the metallurgical tools used in the model validation calculate the enthalpy input of individual chemical reactions using standard enthalpies of reactions, the most impactful reactions (Tab. 9) were also calculated using this method in an external sub-model to facilitate a comparison of the results as part of the model validation. The mass specific standard enthalpies of reactions (ΔH_{298}^0) were calculated using HSC chemistry.

Tab. 9: Reactions calculated separately for the model validation and their specific reaction enthalpies.

Reaction				ΔH_{298}^0	
In the melt or slag phase					
C (s)	+	0.5 O ₂ (g)	→	CO	-2.556 kWh/kg C
Fe (s)	+	0.5 O ₂ (g)	→	FeO	-1.318 kWh/kg Fe
2 Fe (s)	+	1.5 O ₂ (g)	→	Fe ₂ O ₃	-2.020 kWh/kg Fe
Si (s)	+	1 O ₂ (g)	→	SiO ₂	-9.009 kWh/kg Si
2P (s)	+	2.5 O ₂ (g)	→	SiO ₂	-6.749 kWh/kg P
Mn (s)	+	0.5 O ₂ (g)	→	MnO	-1.948 kWh/kg Mn
2Cr (s)	+	1.5 O ₂ (g)	→	Cr ₂ O ₃	-3.010 kWh/kg Cr
In the gas phase					
CH ₄ (g)	+	2 O ₂ (g)	→	CO ₂ (g)+H ₂ O (l)	-13.900 kWh/kg CH ₄
CO (g)	+	0.5 O ₂ (g)	→	CO ₂	-9.101 kWh/kg CO
H ₂ O (l)			→	H ₂ O (g)	-1.461 kWh/kg H ₂ O

The mass of reactants was calculated from the in- and outlet molar flowrates on a species level. In most cases, the sum of reaction enthalpies of all reactions only deviated slightly from the value of ΔE_{Chem} calculated according to Tab. 10. This proves that the reactions from Tab. 9 do account for most of the chemical energy considered in the process model.

Tab. 10: Terms for the validation of the energy balance as calculated by the black box model. $\dot{m}_{i,j}$ represents the mass flow, t_{ttt} is the tap-to-tap time and $c_{i,j}$ the mass fraction of the component i in the stream j .

Energy Balance	Equation Black Box Model
$\Delta W_{Electric}$	$\Delta W_{Electric}$
$\Delta Q_{Cooling} + \Delta Q_{Rad,other}$	ΔQ_{Loss}
$\Delta H_{Scrap,HM}$	$\sum_{i,scrap} \left(\dot{m}_{i,scrap} \cdot t_{ttt} \cdot c_{i,scrap} \cdot h_{T_{Scrap}}^0(i) \right) - \sum_{i,scrap} \left(\dot{m}_{i,scrap} \cdot t_{ttt} \cdot c_{i,scrap} \cdot h_{298}^0(i) \right) +$ $\sum_{i,hot.metal} \left(\dot{m}_{i,hot.metal} \cdot t_{ttt} \cdot c_{i,hot.metal} \cdot h_{T_{hot.metal}}^0(i) \right) - \sum_{i,hot.metal} \left(\dot{m}_{i,hot.metal} \cdot t_{ttt} \cdot c_{i,hot.metal} \cdot h_{298}^0(i) \right)$
ΔH_{Steel}	$\sum_{i,Steel} \left(\dot{m}_{i,Steel} \cdot t_{ttt} \cdot c_{i,Steel} \cdot h_{T_{Steel}}^0(i) \right) - \sum_{i,Steel} \left(\dot{m}_{i,Steel} \cdot t_{ttt} \cdot c_{i,Steel} \cdot h_{298}^0(i) \right)$
ΔH_{Slag}	$\sum_{i,Slag} \left(\dot{m}_{i,Slag} \cdot t_{ttt} \cdot c_{i,Slag} \cdot h_{T_{Slag}}^0(i) \right) - \sum_{i,Slag} \left(\dot{m}_{i,Slag} \cdot t_{ttt} \cdot c_{i,Slag} \cdot h_{298}^0(i) \right)$
$\Delta H_{Off-gas}$	$\sum_{i,Off-gas} \left(\dot{m}_{i,Off-gas} \cdot t_{ttt} \cdot c_{i,Off-gas} \cdot h_{T_{Off-gas}}^0(i) \right) - \sum_{i,Off-gas} \left(\dot{m}_{i,Off-gas} \cdot t_{ttt} \cdot c_{i,Off-gas} \cdot h_{298}^0(i) \right)$
$\Delta H_{sf} + \Delta H_{sol}$	$\sum_{i,hot.metal} \left(\dot{m}_{i,hot.metal} \cdot t_{ttt} \cdot c_{i,hot.metal} \cdot [h_{T_{hot.metal}}^0(i) + \Delta h_{sol}(i)] \right) + \sum_{i,scrap} \left(\dot{m}_{i,scrap} \cdot t_{ttt} \cdot c_{i,scrap} \cdot \Delta h_{sol}(i) \right) -$ $\sum_{i,steel} \left(\dot{m}_{i,steel} \cdot t_{ttt} \cdot c_{i,steel} \cdot \Delta h_{sol}(i) \right) - \sum_{i,slag} \left(\dot{m}_{i,slag} \cdot t_{ttt} \cdot c_{i,slag} \cdot [h_{T_{i,slag}}^0(i) + \Delta h_{sf}(i) + \Delta h_{sol}(i)] \right) +$
ΔE_{Chem}	$\Delta E_{Chem} = \Delta H_{Steel} + \Delta H_{Slag} + \Delta H_{Off-gas} - \Delta H_{Scrap,HM} - \Delta W_{Electric} + \Delta Q_{Loss} + \Delta H_{sf} + \Delta H_{sol}$

3.3 Cooling Stack

The required air input for the cooling stack is determined based on the off-gas output and composition from the black box and an air ratio λ , which represents the ratio of the actual amount of used oxygen to the minimum amount of oxygen needed for a theoretical complete oxidation. The implemented equation for the dust oxidation and post combustion in the cooling stack is given as eq. (53) [11].

$w_{\text{off gas},i}$ is the mass fraction and MW_i is the molar mass of the species i in the off-gas. If dust oxidation is not chosen in the GUI, only CO and H₂ are oxidised completely and only the first two terms of eq. (53) apply. If dust oxidation is active, all combustion reactions given in Tab. 11 take place completely in the direction of the oxides, representing complete dust oxidation [11].

$$\begin{aligned}
 \frac{\dot{m}_{\text{Air CS}} \cdot w_{\text{Air,O}}}{\lambda \cdot \dot{m}_{\text{off gas}}} = & w_{\text{off gas,CO}} \cdot \frac{1}{2} \cdot \frac{MW_{\text{O}}}{MW_{\text{CO}}} + w_{\text{off gas,H2}} \cdot \frac{1}{2} \cdot \frac{MW_{\text{O}}}{MW_{\text{H2}}} + \\
 & w_{\text{off gas,Fe}} \cdot \frac{1}{2} \cdot \frac{MW_{\text{O}}}{MW_{\text{Fe}}} + w_{\text{off gas,Si}} \cdot 1 \cdot \frac{MW_{\text{O}}}{MW_{\text{Si}}} + w_{\text{off gas,Mn}} \cdot \frac{1}{2} \cdot \frac{MW_{\text{O}}}{MW_{\text{Mn}}} \\
 & + w_{\text{off gas,P}} \cdot \frac{5}{4} \cdot \frac{MW_{\text{O}}}{MW_{\text{P}}} + w_{\text{off gas,Cr}} \cdot \frac{3}{4} \cdot \frac{MW_{\text{O}}}{MW_{\text{Cr}}} + w_{\text{off gas,V}} \cdot \frac{3}{4} \cdot \frac{MW_{\text{O}}}{MW_{\text{V}}} \\
 & + w_{\text{off gas,Cu}} \cdot \frac{1}{4} \cdot \frac{MW_{\text{O}}}{MW_{\text{Cu}}} + w_{\text{off gas,Mo}} \cdot 1 \cdot \frac{MW_{\text{O}}}{MW_{\text{Mo}}} + w_{\text{off gas,Ni}} \cdot \frac{1}{2} \cdot \frac{MW_{\text{O}}}{MW_{\text{Ni}}} \\
 & + w_{\text{off gas,Sn}} \cdot 1 \cdot \frac{MW_{\text{O}}}{MW_{\text{Sn}}} + w_{\text{off gas,Pb}} \cdot \frac{1}{2} \cdot \frac{MW_{\text{O}}}{MW_{\text{Pb}}} + w_{\text{off gas,Zn}} \cdot \frac{1}{2} \cdot \frac{MW_{\text{O}}}{MW_{\text{Zn}}} \\
 & - w_{\text{off gas,CO}}
 \end{aligned} \tag{ 53 }$$

Tab. 11: Dust oxidation reaction considered in the cooling stack model [11].

$\text{CO} + 0.5 \text{O}_2 \rightarrow \text{CO}_2$	$2 \text{V} + 1.5 \text{O}_2 \rightarrow \text{V}_2\text{O}_3$
$\text{H}_2 + 0.5 \text{O}_2 \rightarrow \text{H}_2\text{O}$	$2 \text{Cu} + 0.5 \text{O}_2 \rightarrow \text{Cu}_2\text{O}$
$\text{Fe} + 0.5 \text{O}_2 \rightarrow \text{FeO}$	$\text{Mo} + \text{O}_2 \rightarrow \text{MoO}_2$
$\text{Si} + \text{O}_2 \rightarrow \text{SiO}_2$	$\text{Ni} + 0.5 \text{O}_2 \rightarrow \text{NiO}$
$\text{Mn} + 0.5 \text{O}_2 \rightarrow \text{MnO}$	$\text{Sn} + \text{O}_2 \rightarrow \text{SnO}_2$
$2 \text{P} + 2.5 \text{O}_2 \rightarrow \text{P}_2\text{O}_5$	$\text{Pb} + 0.5 \text{O}_2 \rightarrow \text{PbO}$
$2 \text{Cr} + 1.5 \text{O}_2 \rightarrow \text{Cr}_2\text{O}_3$	$\text{Zn} + 0.5 \text{O}_2 \rightarrow \text{ZnO}$

3.4 Electrical Energy Demand Sub-model

Since the electrical energy demand represents an important factor for overall cost as well as CO₂ emissions of the EAF process, a sub-model was needed to enhance the predictive capabilities of the EAF process model by calculating this parameter based on the used solid and gaseous inputs. After extensive research in the scientific literature (see chapter 2.2.3), the approach of a data-driven model based on multiple linear regression inspired by the Köhle model was chosen. The math behind the MLR is explained in chapter 2.3. All equations needed were directly implemented in the top layer of the EAF process model. The main equation to calculate the specific energy demand is shown in eq. (54) and the used parameters are explained in Tab. 13

The inputs variables for the calculation of the electrical energy demand are directly taken from the input ports of the EAF model. Not all available implemented parameters were used in this work, but they can be used in future modelling approaches. To determine the regression parameters, 4 modelling approaches were tested using plant data, and the results are covered in chapter 4.1. The input parameters that need to be set in the GUI of the mode and their bounds and typical range are shown in Tab. 12.

Tab. 12: Statistical sub-model GUI input parameters.

Parameter	Symbol	Range	Pre-set
Fraction of HBI/DRI of the total ferrous inputs (-)	$c_{DRI/HBI}$	0 to 1	0
Fraction of scrap of the total ferrous inputs (-)	c_{Scrap}	0 to 1	1
Fraction of coal charged (not injected) (-)	c_{Coal}	0 to 1	0.4
Fraction of nat. gas used for post combustion (-)	c_{GPC}	0 to 1	0
Yield factor hot metal (mechanical losses) (-)	y_{HM}	0 to 1	0
Yield factor scrap (mechanical losses) (-)	y_{Scr}	0 to 1	0
Power on time (min)	t_{S2}	0 to ∞	50
Power off time (min)	t_N	0 to ∞	10
Furnace factor (-)	NV	-1 to 3	0
Regression Variables (-)	Various	$-\infty$ to ∞	Various

For the validation part of this work, the second MLR model (MLR model 2, see chapter 4.1) was used, but other models from this work or future models based on additional data can easily be implemented by changing the regression parameters in the user interface. This enables the adaptation of the sub-model to different EAF types and operations.

$$\begin{aligned} \frac{W_R}{\text{kWh/t}} = & \text{Base} + G_E \cdot \left(\frac{G_E}{G_A} - 1 \right) + G_Z \cdot \frac{G_Z}{G_A} + G_{DRI} \cdot \frac{G_{DRI}}{G_A} + G_{HM} \cdot \frac{G_{HM}}{G_A} \\ & \cdot + G_{SR} \cdot \frac{G_{Shr}}{G_A} + G_{SC} \cdot \frac{G_{Scr}}{G_A} + T_A \cdot (T_A - 1600) + StN \\ & \cdot (t_S + t_N) + M_G \cdot M_G + M_L \cdot M_L + M_N \cdot M_N + NV \cdot W_V \end{aligned} \quad (54)$$

Tab. 13: Input parameter description for the electrical energy (EE) demand statistical sub-model. m_j is the mass input through port j in t , c_i is the mass fraction of i in the input stream.

Input Parameter	Description	Equation
W_R	Specific EE demand (kWh/t)	Equation (54)
G_E	Mass of ferrous inputs (t)	$m_{Scrap} \cdot c_{Scrap} + m_{HM} \cdot c_{HM}$
$G_{DRI/HBI}$	Mass of DRI or HBI input (t)	$m_{Scrap} \cdot c_{DRI/HBI}$
G_{HM}	Mass of Hot Metal input (t)	$m_{HM} \cdot Y_{HM} \cdot c_{HM}$
G_{Scr}	Mass of scrap input (t)	$m_{Scrap} \cdot Y_{Scr} \cdot c_{SHR}$
G_A	Furnace tap weight (t)	m_{Steel}
G_Z	Weight of slag formers (t)	$m_{Lime} + m_{Dolomite}$
T_A	Tapping temperature (°C)	Set in GUI
t_S	Power-on time (min)	Set in GUI
t_N	Power-off time (min)	Set in GUI
M_G	Specific burner gas (kg/t)	$\frac{m_{nat.Gas} \cdot (1 - c_{GPC}) \cdot 1000}{m_{Steel}}$
M_L	Specific lance oxygen (kg/t)	$\frac{m_{O2-Lance} \cdot 1000}{m_{Steel}}$
M_N	Specific burner oxygen (kg/t)	$\frac{m_{O2-Burner} \cdot 1000}{m_{Steel}}$
W_V	Specific energy losses (kWh/t)	Set in GUI or calculated in black box sub-model
NV	Furnace factor (-)	Set in GUI
Base	Regression parameter (kWh/t)	Set in GUI
$G_E, G_Z, G_{DRI}, G_{HM},$ $G_{SR}, G_{SC}, T_A, StN,$ M_G, M_L, C, M_N	Regression parameters (-)	Set in GUI

3.5 Initialisation Procedures

The initialisation is a crucial part of the process model as it is needed to reach solution convergence and to enable the execution of reverse calculations. In a reverse calculation, values for an input stream are calculated based on given output specifications (see Tab. 4). An initialisation procedure is not based on physics and chemical phenomena. It is a tool to help the mathematical solver group equations, handle recycles and reach convergence [10]. The standard initialisation sequence of the EAF process model is shown in Tab. 14 with an explanation of the steps given below.

Tab. 14: Initialisation procedure of the EAF process model [10].

Step	Procedure
1	Application of specifications at the black box outlet ports
2	Applications of product specifications at the EAF outlet ports
3	Calculation of the air demand for the cooling stack
4	Activation of the energy balance

Step 1: Input flows and the electrical energy demand are set to empirical values. When “set” is selected in the distribution case selector, the element distributions are set to the values provided in the GUI. When “calculated” is selected, they are set to empirical values. The compositions of the black box output streams are set to the specifications defined in the GUI. Steel evaporation, steel and slag spitting, and phase mixing are calculated.

Step 2: The compositions of the EAF output streams are set to the specifications defined in the GUI. If the element distributions are calculated, they are now set to the calculated values. Input flows for the black box are then calculated to meet the set criteria.

Step 3: The air demand of for the cooling stack is calculated based on the black box off-gas amount and composition considering dust oxidation and the WGSR according to the GUI settings.

Step 4: The EAF’s electrical energy demand and heat loss are calculated according to the energy balance or the statistical sub-model according to the settings chosen in the GUI. If the energy consumption case selector is set to “set consumption or heat loss”, $\Delta W_{Electric}$ or ΔQ_{Loss} need to be set and the other one is calculated, if “calculate consumption and heat loss”, is selected, $\Delta W_{Electric}$ is set by the energy demand sub-model and ΔQ_{Loss} is calculated.

3.6 Range and Processing of the Plant Data

The plant data used for the development of the Energy demand sub-model and for the model validation was provided by Primetals Technologies Austria GmbH and included data from 62 individual heats of three different EAF types, a conventional EAF, a Quantum EAF with a scrap preheating system and a Consteel EAF, which is a combination of a BOF and EAF using two shells (see chapter 2.1.4). The received plant data included input amounts and compositions of non-ferrous materials, various process parameters, steel temperature and values for the specific chemical and electrical energy consumptions.

For some heats, steel and slag analysis were included. Information on the mass or composition of the hot heel was not provided. The steel and slag analysis only represents the composition at the time it was taken and not the endpoint composition, since tapping and de-slagging are processes that take several minutes and the steel and slag composition at the beginning of the tap is not the same as the composition at the end. For some heats, a steel analysis at the beginning of the ladle process was available. However, this also doesn't represent the endpoint composition of the EAF process, as ferroalloys were already added during the tapping before the samples were taken. For this reason, the steel analysis from the ladle couldn't be used and the last available analysis from the EAF process was used instead. The slag analysis was performed using x-ray fluorescence spectroscopy and in the provided results about 10% of the mass composition were unaccounted for. The reasons for the missing 10% are probably errors in the conversion of the detected elements into the oxides, as well as elements not detected at all by the used spectrometer. For this work, the missing mass percent were assigned the species "rest", which is a catch-all term for all components that were not assigned a specific species.

Only 3 Heats were removed from the data set due to faulty or irregular data logging or equipment malfunctions resulting in tap-to-tap times of multiple hours. Some heats showed noticeable higher energy demands combined with longer than average tap to tap times, but were not removed, since the model should represent the actual industrial process which sometimes include unplanned delays. The received data were processed using the integrated development environment PyCharm for the python programming language [63]. The created scripts were mainly used to add up all the additions of lime, dolomite, coal and different scrap types to the furnace for each heat. The data was then exported to MS Excel, where the statistical calculations were performed.

4 Results and Validation

In this chapter, the regression results of the statistical energy model (chapter 4.1) as well as the validation of the new EAF process model using results of proven metallurgical tools (chapter 4.2.1) and plant data (chapter 4.2.2) will be presented. The validation is performed to ensure the accuracy as well as stability of the new model and it includes the description of validation scenarios, model specifications and detailed discussion of the simulation results, including mass and energy balances. The validation of the statistical sub-model for calculation of the electrical energy (EE) demand will also include more details on the modelling process and provides statistical data as well as a validation and discussion of each regression model.

4.1 Electrical Energy Demand Sub-model

The statistical energy demand sub-model is based on the received plant data from three industrial EAF's. To enable easy comparison of EAFs with different capacities, the unit of the output values for the electric energy demand is kWh per ton crude steel produced. The calculations of the sub-model are solely based on the material inputs and process parameters given in the plant data. Four different regression model approaches are presented and their applicability to estimate the demand of electrical energy for individual and average EAF heats was examined. The models were then compared to choose the best one for implementation in the EAF process model. The approaches are:

- Köhle model without a set energy loss:
- Köhle model with a set energy loss
- MLR model 1
- MLR model 2

The first two models were based on the established Köhle model, first without and then with a set energy loss. The third modelling approach MLR model 1 determines the regression coefficients of the Köhle model using multiple linear regression. For the fourth model, MLR model 2, the most important regression coefficients were selected, and their values were determined using MLR.

Köhle model without set energy loss

The first approach was to apply the expanded Köhle model presented in eq. (14) directly to the plant data of all three EAF's. The results can be seen in Figure 21. Since there was no information given regarding the energy loss in the plant data, this term was set to zero.

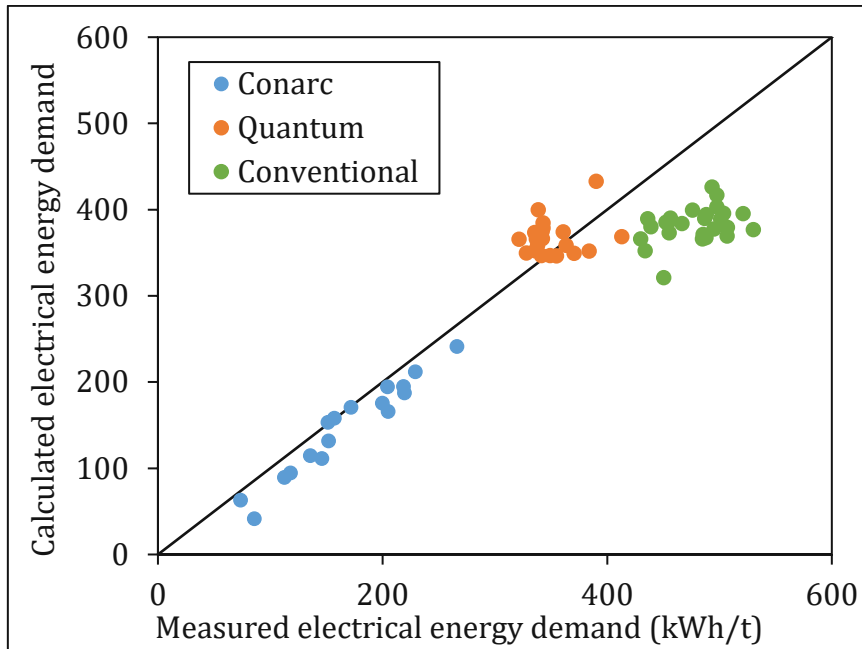


Figure 21: Measured EE demand from the industry data vs. EE demand results of the Köhle model for the Conarc, Quantum and conventional EAF; Energy loss is set to 0; $R^2= 0.83$, RSE= 53.9 kWh/t; the black line represents a perfect fit.

As expected, three clusters representing the three EAF types are clearly visible. With a regression standard error (RSE) of 53.9 kWh/t steel (about 12.5%), the model's accuracy is insufficient.

The offset of the clusters from the perfect fit line is probably partly caused by different heat losses of the three furnace types. The calculated values for the conventional EAF are significantly lower than the measured values, indicating that this EAF has a higher heat loss than the Quantum EAF. The lower heat loss of the Quantum EAF can be explained by its integration of off-gas heat for scrap preheating.

The energy demand for the Conarc is lower than the other two EAF's, which results from the higher sensible heat introduced by the use of hot metal as an input. In terms of heat loss, the Conarc seems to be located between the Conventional and the Quantum EAF.

Köhle model with set energy loss

Based on the findings from the first approach, an energy loss of 100 kWh/t crude steel was assumed and a furnace factor for each EAF type was determined according to the average offset of each EAF cluster in the first approach. The result is shown in Figure 22.

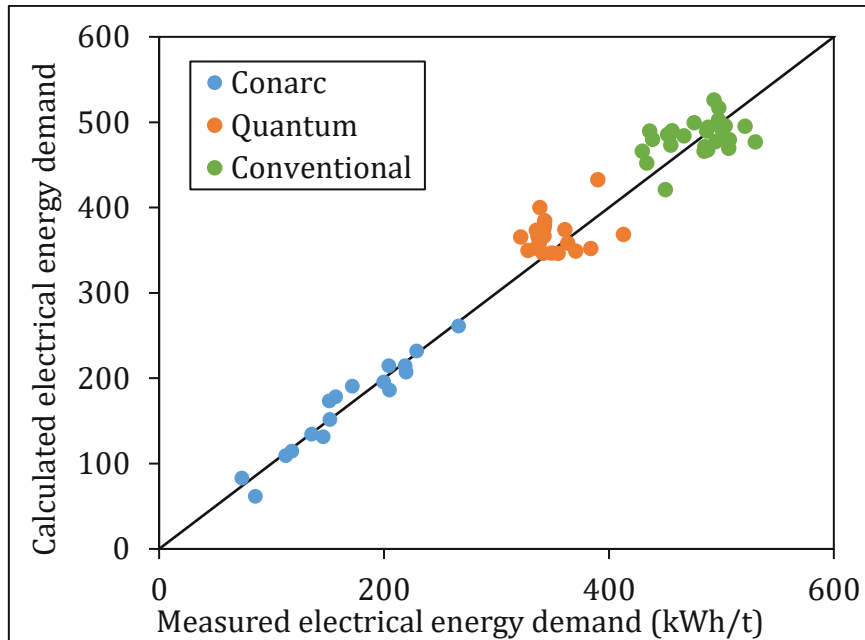


Figure 22: Measured EE demand from the industry data vs. EE demand results of the Köhle model for the Conarc, Quantum and conventional EAF; Energy loss is set to 100 kWh/t; furnace factors Conarc=0.1, Quantum = 0, Conventional = 1; $R^2= 0.96$, RSE = 25.2 kWh/t.

The RSE could be significantly reduced from 54 to 25 and a higher coefficient of determination (R^2) was achieved, indicating a better fit of the data to the linear model. This model could be implemented as is, but the problem that a heat loss or a furnace factor, which is often not available, must be set remains.

MLR model 1

Since there are many examples of regression models in the literature that don't use the energy loss term (e.g. [44]), the next step was to estimate the regression parameters of the Köhle model using multiple linear regression to fit the industry data. The results are shown in Figure 23.

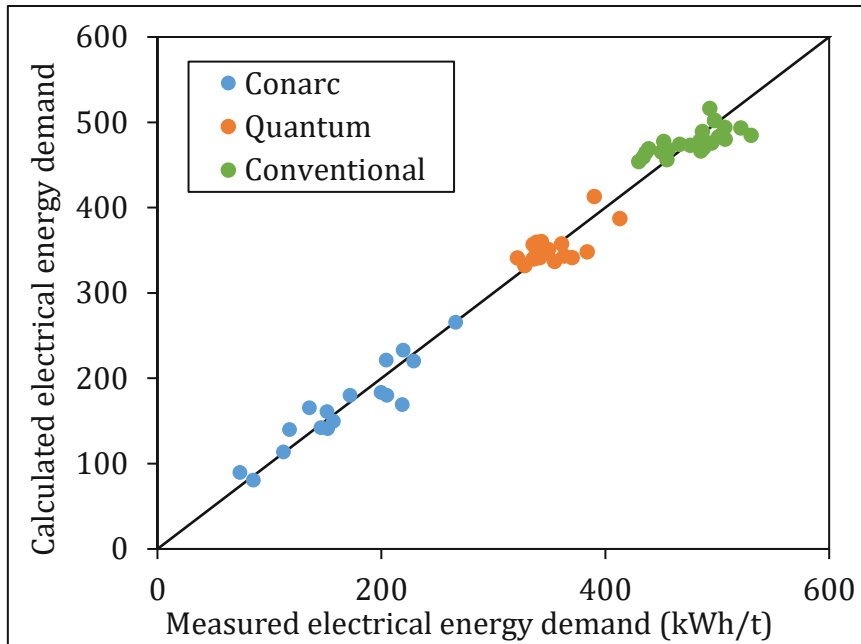


Figure 23: Measured EE demand from the industry data vs. EE demand results of MLR model 1 for the Conarc, Quantum and conventional EAF, using the same descriptors as the Köhle model; Energy loss is set to 0; $R^2 = 0.97$, $RSE = 22.9$ kWh/t.

At first sight the results look promising, since a lower RSE and a higher R^2 value was achieved, while also getting rid of the unwanted term for the energy losses. However, to validate the overall quality of the linear regression model these parameters alone are not sufficient and an analysis of variance (ANOVA) as well as other statistical tests were performed.

The results of the ANOVA of regression model 1 are shown in Tab. 15. The high F value of 198 and the low significance of the F value indicate that there exists a significant linear relation between the selected inputs and the electrical energy demand. Looking at the individual coefficients in Tab. 16, the high corresponding p-Values indicate, that either the chosen input parameters do not have a significant influence on the output or that strong collinearities between the input parameters are present.

One explanation for this is that only 62 heats were used in this model while the original Köhle model used over 5000. If we compare the results for the coefficients with the Köhle model (Tab. 17) it is obvious, that unlike the Köhle model, not all values for the regression coefficients can be explained directly by empirical considerations. For example, the coefficient for the burner gas is positive despite the use of additional gas as fuel should lower the electrical energy demand. This is not unusual and was also the case in many models found in the literature [43]. It must be considered that the MLR model only fits the

coefficients to the data and correlation does not imply causation, since the coefficients only indicate a change in the target variable relative to the other coefficients.

To test the prerequisites of normal distribution and homoscedasticity of the residuals, a histogram (Figure 24) and a scatter plot (Figure 25). were visually checked. In conclusion, the residuals seem normally distributed and it can be assumed they are homoscedastic. The final equation of MLR model 1 is given in eq. (13).

Tab. 15: ANOVA results for MLR model 1.

	df	SS	MS	F	Significance F
Regression	10	1041609	104160.9	197.9	< 0.0001
Residual	52	27363.05	526.2		
Total	62	1068972			

Tab. 16: Regression results of MLR model 1.

	Coefficients	Standard Error	t Stat	P-value
Intercept	353.18	152.09	2.32	0.02
Ferrous inputs	336.99	150.97	2.23	0.03
Slag formers	-170.06	514.13	-0.33	0.74
Tapping temperature	0.16	0.13	1.21	0.23
DRI or HBI input	130.04	131.68	0.99	0.33
Hot Metal input	-433.16	161.73	-2.68	0.01
Shredder input	-12.48	138.45	-0.09	0.93
Burner gas	21.80	9.23	2.36	0.02
Lance oxygen	-1.42	1.15	-1.23	0.22
Post-combustion oxygen	-3.38	2.69	-1.26	0.22
Tap-to-tap time	-0.32	0.59	-0.54	0.59

Tab. 17: Regression coefficients from MLR model 1 compared to the Köhle model.

	Coefficients Köhle	Coefficients MLR Model 1
Intercept	375	353.175
Ferrous inputs	400	336.986
Slag formers	1000	-170.06
Tapping temperature	0.3	0.158
DRI or HBI input	80	130.035
Hot Metal input	-350	-433.162
Shredder input	-50	-12.480
Burner gas	-8	21.803
Lance oxygen	-4.3	-1.419
Post-combustion oxygen	-2.8	-3.382
Tap-to-tap time	1	-0.318

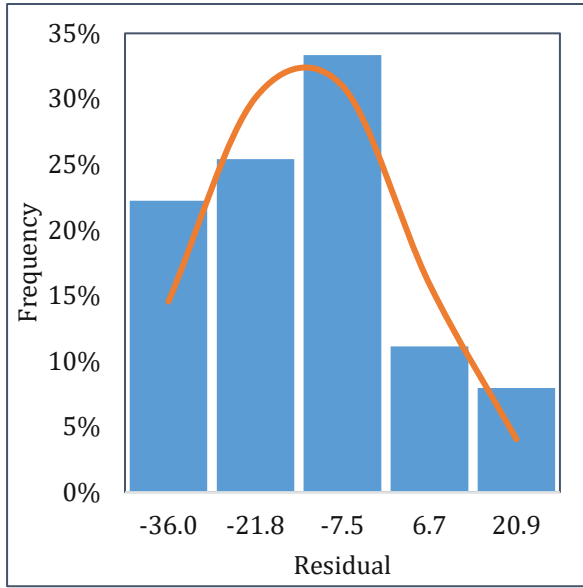


Figure 24: Histogram of the residuals for MLR model 1. The orange curve illustrates an ideal normal distribution.

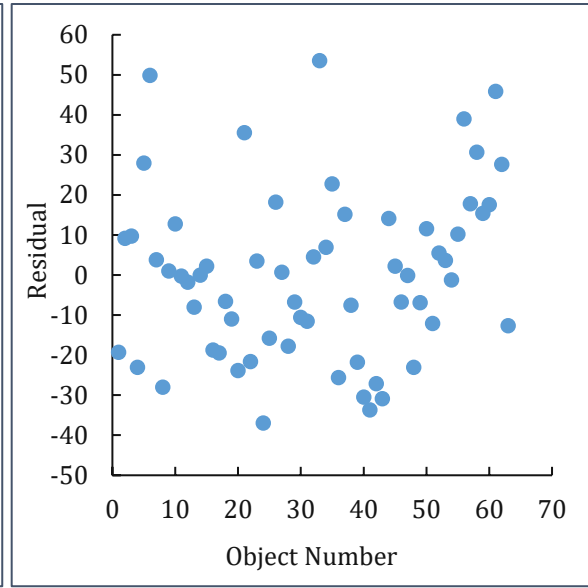


Figure 25: Scatter plot of the residuals for MLR model 1.

$$\begin{aligned} \frac{W_R}{\text{kWh/t}} = & 353.18 + 336.99 \left(\frac{G_E}{G_A} - 1 \right) + 131.04 \frac{G_{\text{DRI/HBI}}}{G_A} - 12.48 \frac{G_{\text{Shr}}}{G_A} \\ & - 433 \frac{G_{\text{HM}}}{G_A} - 170.6 \frac{G_Z}{G_A} + 0.16 (T_A - 1600) - 0.32 \frac{t_S}{t_N} \quad (55) \\ & + 21.8 M_G - 1.42 M_L - 3.38 M_N + NV \times 100 \end{aligned}$$

MLR model 2

Since MLR model 1 did not pass all the statistical tests, as too many variables were used and multicollinearities were present, another model was developed. It is obvious that fitting 10 regression parameters with only 62 values will probably result in an overfit. The received plant data includes a multitude of different input variables, many of which are being used in other linear regression models found in the scientific literature [18, 43, 44]. Multiple MLRs were performed to select the six most impactful input variables, which were then used as a basis for MLR model 2. The accepted and rejected parameters can be found in Tab. 18. The rejected variables could be added to the model once more data points are available.

The result can be seen in Figure 26. The ANOVA, regression results and comparison to the Köhle model can be found in Tab. 19-Tab. 21.

Tab. 18: Selection of Key Input Variables for MLR model 2.

Input Variable	Selected	Rejected	Reason for rejection
Ferrous inputs	✓		
DRI or HBI input	✓		
Hot metal input	✓		
specific burner gas	✓		
specific lanced oxygen	✓		
specific burner oxygen	✓		
Injected coal		X	insignificant, high p value
Slag formers		X	insignificant, high p value
Charged coal		X	insignificant, high p value
Scrap input		X	multicollinearity (hot metal input)
DRI temperature		X	not enough data points
HBI temperature		X	not enough data points
Scrap temperature		X	not enough data points
C content in steel		X	insignificant, high p value
Tap-to-tap time		X	various multicollinearities

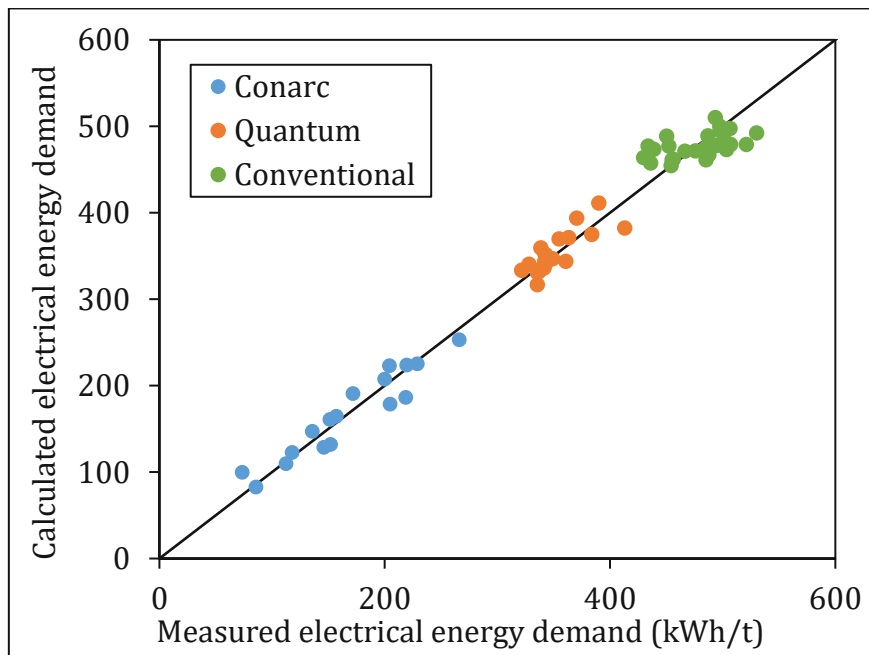


Figure 26: Measured EE demand from the industry data vs. EE demand results of MLR model 2 for Conarc, Quantum and conventional EAF; no energy loss; $R^2 = 0.97$, RSE = 20.0 kWh/t.

Tab. 19: ANOVA results for MLR model 2.

	df	SS	MS	F	Significance F
Regression	6	1046645	174441	437	< 0.0001
Residual	56	22329	399		
Total	62	1068972			

Tab. 20: Regression results of MLR model 2.

	Coefficients	Standard Error	t Stat	P-value
Intercept	294.81	27.66	10.66	< 0.0001
Ferrous inputs	343.95	51.16	6.72	< 0.0001
DRI or HBI input	195.71	41.93	4.67	< 0.0001
Hot metal input	-254.72	63.55	-4.01	0.0002
Burner gas	-5.91	1.25	-4.73	< 0.0001
Lanced oxygen	-2.56	1.01	-2.54	0.0139
Post-combustion oxygen	30.21	3.26	9.28	< 0.0001

Tab. 21: Regression coefficients from MLR model 2 compared to the Köhle model.

	Coefficients Köhle	Coefficients Model 1
Intercept	294.81	353.16
Ferrous inputs	343.95	336.99
DRI or HBI input	195.71	130.04
Hot metal input	-254.72	-433.16
Burner gas	-5.91	21.80
Lanced oxygen	-2.56	-1.42
Post-combustion oxygen	30.21	-3.38

The normal distribution of the residuals was checked by visually examining the histogram (Figure 28) and a normal distribution can be observed (Figure 27). To get a better picture of the variance inside each EAF cluster, they are individually depicted in Figure 29. There seem to be no artificial trends in the data.

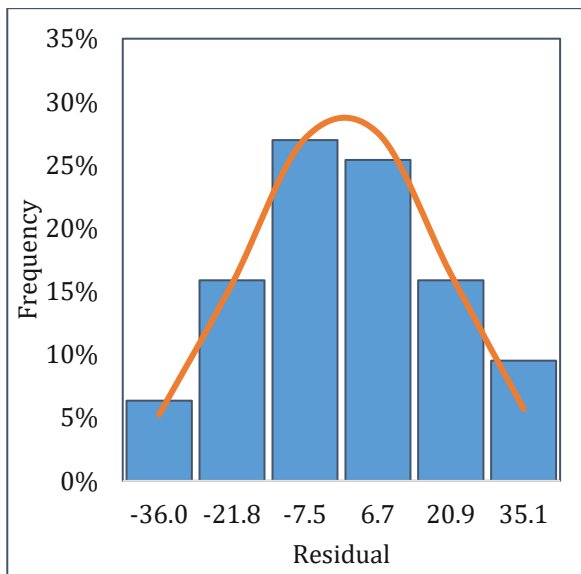


Figure 27: Histogram of the residuals for MLR model 3. The orange curve illustrates an ideal normal distribution.

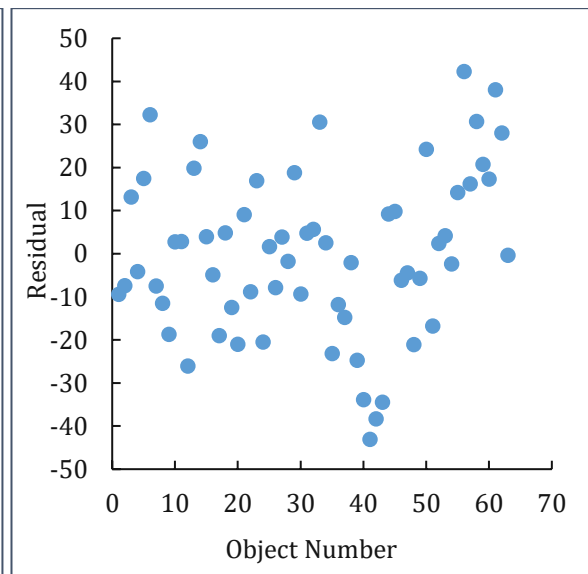


Figure 28: Scatter plot of the residuals for Model 2.

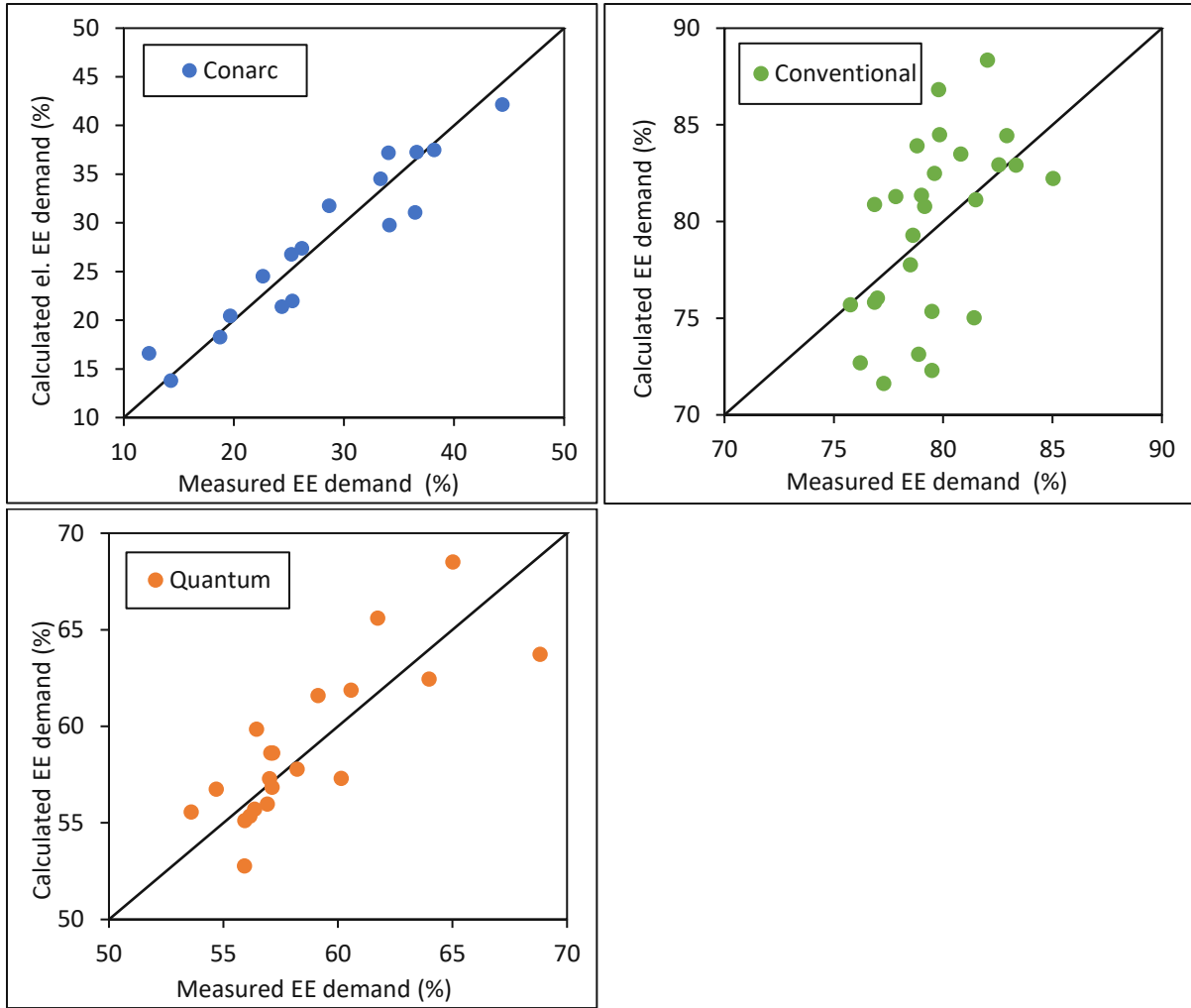


Figure 29: Clusters of the different EAF types, measured EE demand from the industry data vs. simulation results of MLR model 2 for the Conarc, Quantum and conventional EAF.

The final equation of MLR model 2 can be seen in eq. (56). In conclusion, MLR model 2 shows high linearity with an R^2 value of 0.97 and represents the plant data well with an RSE of 20.0 kWh/t steel, which equals about 6% of the electrical energy demand.

$$\frac{W_R}{\text{kWh/t}} = 294.81 + 343.95 \left(\frac{G_E}{G_A} - 1 \right) + 195.71 \frac{G_{\text{DRI/HBI}}}{G_A} - 254.72 \frac{G_{\text{HM}}}{G_A} - 5.91M_G - 2.56 M_L + 30.21 M_B \quad (56)$$

W_R	Specific electrical energy demand (kWh/t)	M_G	Specific burner gas (m ³ /t)
G_E	Mass of ferrous input materials (t)	M_L	Specific lance oxygen (m ³ /t)
$G_{\text{DRI/HBI}}$	Mass of DRI or HBI input (t)	M_B	Specific burner oxygen (m ³ /t)
G_{HM}	Mass of hot metal input (t)		
G_A	Furnace tap weight (t)		

Comparison of the Regression Models

To decide which model is the best, a comprehensive comparison of the regression standard error (RSE), the max. error and R^2 for each tested model is shown in Tab. 22. The max. error shows the maximum occurring deviation of the calculated value from the true value for a single heat while the RSE is the average deviation from the true value for single heat.

Tab. 22: Comparison of results for the prediction models.

Model	R^2	RSE (kWh/t)	Max. Error (kWh/t)
Köhle no energy loss	0.83	53.9	153.3
Köhle energy loss	0.96	24.6	60.2
MLR model 1	0.97	22.9	53.5
MLR model 2	0.97	20.0	43.1

MLR model 2 shows the best fit to the data with both the lowest RSE and max. error, as well as the highest R^2 together with MLR model 1. While the R^2 values seem high, similar values have been achieved by other models from the scientific literature [43]. This indicates that the electrical energy demand is in fact highly correlated to the inputs of the process. Since the model will probably not be used to calculate individual heats but rather monthly or yearly averages for an individual EAF, Figure 30 shows the results for each prediction model and EAF type for average heats with the error bars showing the RSE. Since the deviations for the calculated averages (Figure 31) are quite low.

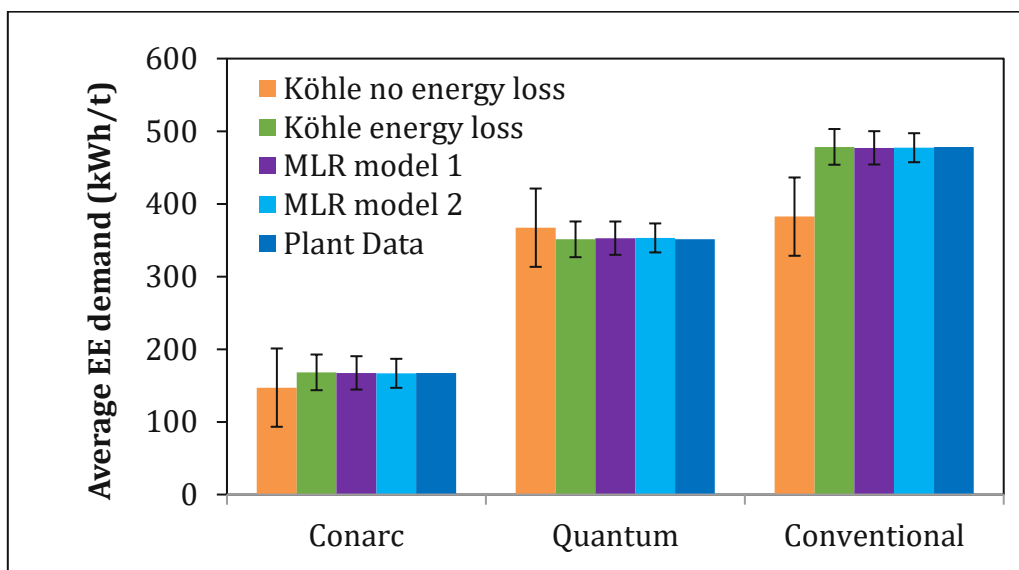


Figure 30: Comparison of the measured average EE demand from the industry data and the average EE demand calculated by the MLR models for the Conarc, Quantum and conventional EAF. Error bars show the regression standard error.

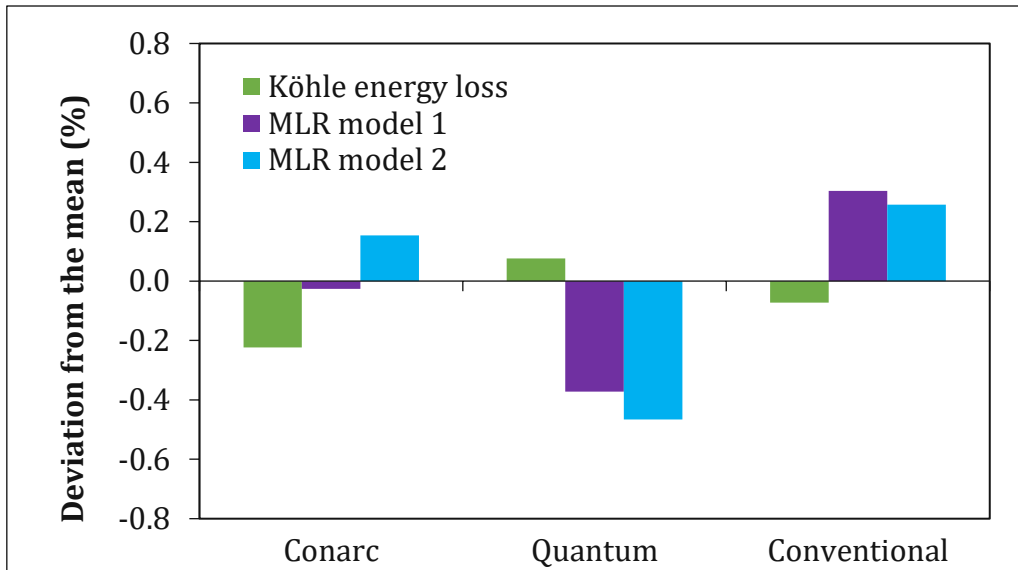


Figure 31: Deviation of the calculated and measured average EE demand for each furnace type (right).

While all models except the Köhle model without energy loss achieve a more than sufficient accuracy with deviations for the average values well below 1%, the lowest deviations for the quantum and conventional EAF are achieved by the Köhle model with a set energy loss. However, since information on the energy loss is usually not available, this model was not chosen for implementation in the new EAF process model. MLR model 1 has the lowest total deviation (Figure 31) for the Conarc and Quantum EAF. In the end, MLR model 2 was chosen for the validation of the EAF process model, since the statistical analysis detected many multicollinearities in MLR model 1 while MLR model 2 passed all the statistical test and even exceeds the other models in terms of accuracy or individual heats.

It is important to mention that the model only represents the provided data it was based on and no predictions for fitting different EAF's or different operations, for example the use of different inputs or the production of different steel grades can be made. The model is also limited by the fact that only data from 62 heats was available, while most models found in the scientific literature use a much larger data set. This work shows how the tool of MLR can successfully be applied to plant data and can serve as a basis for the development of a more generally valid model once more data is available. For specific studies regarding a specific steelmaking route, plant data from a specific EAF can be used to train the model, which can then deliver accurate results for monthly or yearly average productions.

4.2 Validation Using Proven Models

To assure the model's quality, it was tested and validated using proven metallurgical tools as a reference model (ref. model). For this purpose, detailed input data and calculation results for different EAF operation scenarios were received from the EAF specialists at Primetals Technologies Austria GmbH. The data included amount and composition of all input and output materials of individual heats as well as all important process parameters and energy balances. Additional information regarding the furnace type and operation (Tab. 23) were also included. Unfortunately, only the results and not the models itself were made available. Two cases using different types of ferrous inputs (Tab. 24) will be discussed in detail. In both cases, the flowrate of ferrous inputs was calculated based on a set steel production and all other solid and gaseous input streams were set.

Tab. 23: Provided specifications of the EAF used in the validation.

Furnace Specifications	
EAF type	Conventional
Furnace tap weight	150 t
Hot Heel	30 t
Transformer Rating	119 MVA
Operation	Batch
Scrap charging	2 Buckets
DRI charging	Continuous, 5th hole
Hot Metal charging	Discontinuous, HM lounder
Scrap/DRI preheating	no
Number RCB burners	4
Post-Combustion	Not considered
Tap-to-tap time	56 min
Productivity	153 t/h

Tab. 24: Ferrous input materials for case 1 and 2 of the validation.

	Operation Scenario 1	Operation Scenario 2
Hot metal	0%	25%
Steel scrap	20%	25%
Hot DRI	80%	30%
Hot Heel steel	0	20%

In operation scenario 1 (case 1), there was no hot heel steel present in the vessel at the start of the heat and the ferrous inputs consisted of scrap and hot DRI. Operation scenario

2 (case 2) uses hot heel steel from the last heat as well as hot metal as additional ferrous inputs. The parameters presented in Tab. 25 were set as input parameters for the developed EAF process model to calculate the output parameters shown in Tab. 26.

Tab. 25: Input parameters of the EAF process model used for the validation.

Input parameters
Steel production
Solid non-ferrous inputs mass and composition
Gaseous inputs mass and composition
Steel and Slag temperature
C and Si content of steel
Gas dissolution of O, N and H in steel
Distributions for S, Cr, Mn, P
Dust losses for solid inputs
Steel and slag spitting
Steel evaporation
Specific heat loss
Slag FeO and Fe ₂ O ₃ content
Off-gas temperature at off-gas elbow
Off-gas O ₂ , and H ₂ O composition at mouth

Tab. 26: Output parameters of the EAF process model used for the validation. The simulation results were compared to the target values from the ref. model.

Output parameters
Steel composition
Slag quantity, composition and basicity
Off-gas quantity and composition
Dust quantity and composition
Specific electric energy consumption
Post combustion degree at off-gas elbow

The following section will cover a comparison of the provided results and the new model regarding input- and output flows and their composition. Since the metallurgical tool uses the same system boundaries as the black box model, the energy balances of the ref. model and black box model will be compared.

4.2.1 First Operation Scenario

Mass Balance

The solid and gaseous inputs for the first operation scenario are shown below in Figure 32 and Figure 33.

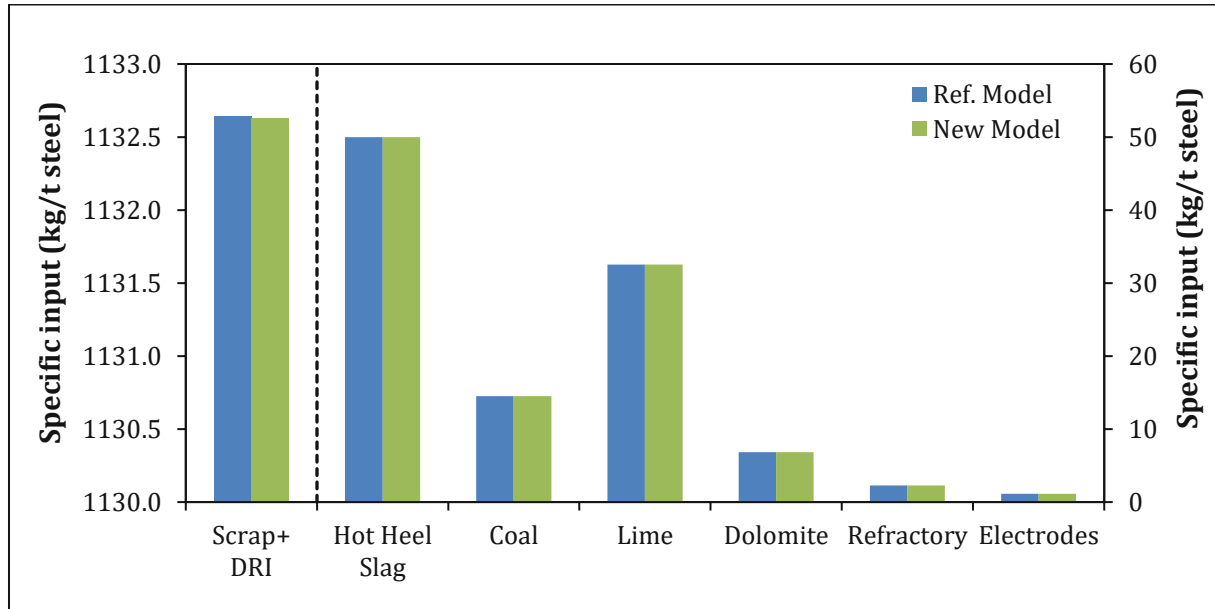


Figure 32: Solid inputs for case 1. New EAF process model (green) compared to the provided ref. model (blue). Ferrous inputs are calculated based on a set steel production. Other inputs are set to target values.

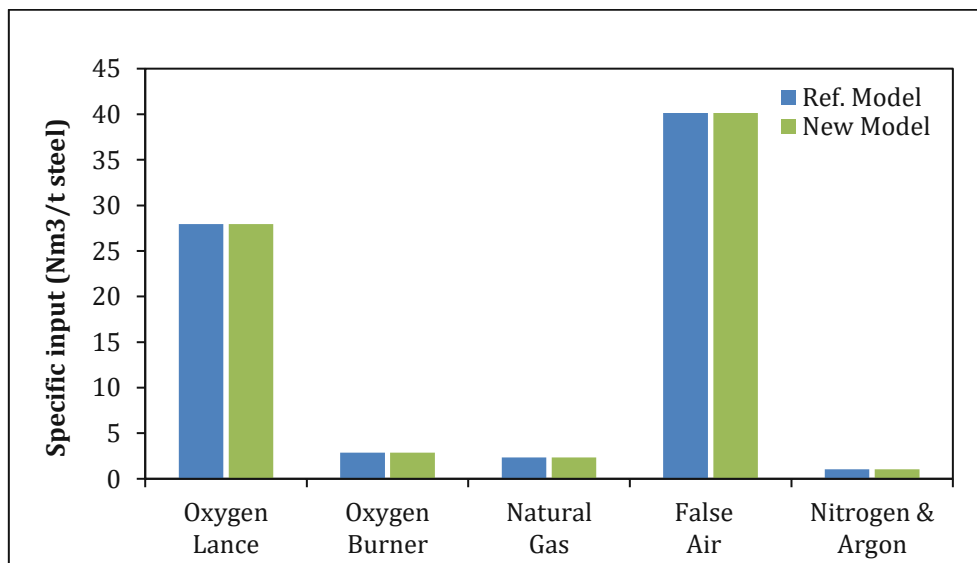


Figure 33: Gaseous inputs for case 1. New EAF process model (green) compared to the provided ref. model (blue). All values set.

The results for the calculated required amount of ferrous inputs (Scrap and DRI) showed no significant deviations. Since all other inputs in Figure 32 were set according to the metallurgical model results, they fit their target values without measurable deviations.

The calculated amount of solid by-products per ton of crude steel produced is shown in Figure 34.

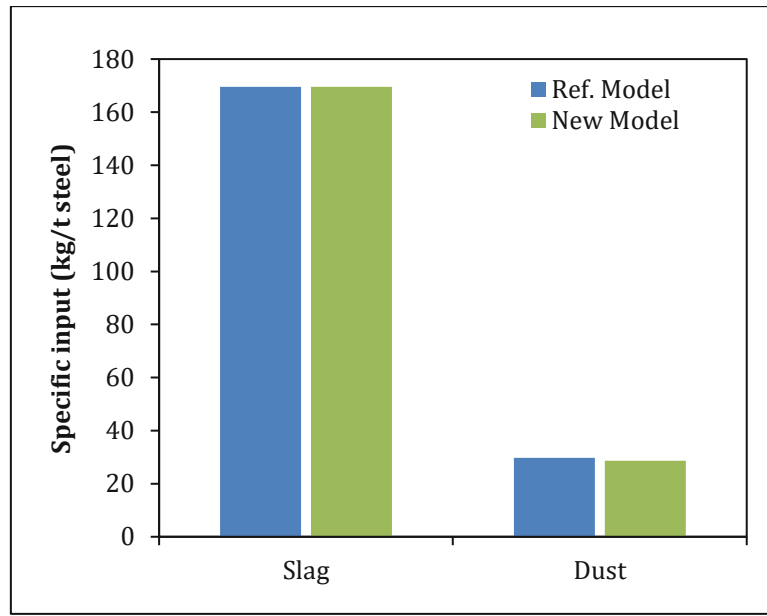


Figure 34: Solid by-products for case 1. New EAF process model (green) compared to the ref. model (blue).

The absolute deviation regarding the slag amount is below 0.01%. The calculated dust amount deviates by about 1% (abs.%). This is due to the different means of dust creation of the two compared models. In the ref. model, all inputs end up in one zone and dust is created using set distributions for every element. The new model uses a splitter cascade before the black box as well as splitters for steel and slag spitting after the black box to create dust. The splitters remove a set mass fraction of the input stream and do not differentiate by chemical compounds or elements. This leads to inevitable differences in dust composition and only the created dust amount was compared. While the new model also has the capability to calculate dust oxidation as part of the post combustion process, post combustion and dust oxidation are not considered in the ref. model. This is because the system boundary of the ref. model is the EAF vessel and the electric system (equal to zone a-a in Figure 7).

Calculation results for the steel and slag composition are depicted in Figure 35 and Figure 36.

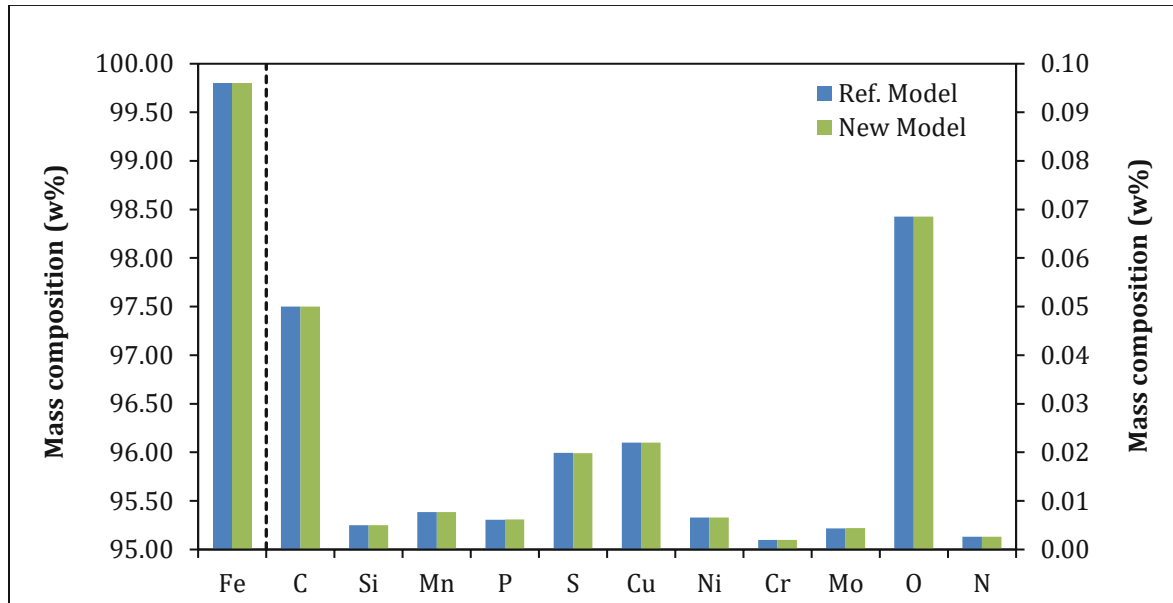


Figure 35: Steel composition for case 1. New EAF process model (green) compared to the ref. model(blue). Steel temperature is 1620 °C.

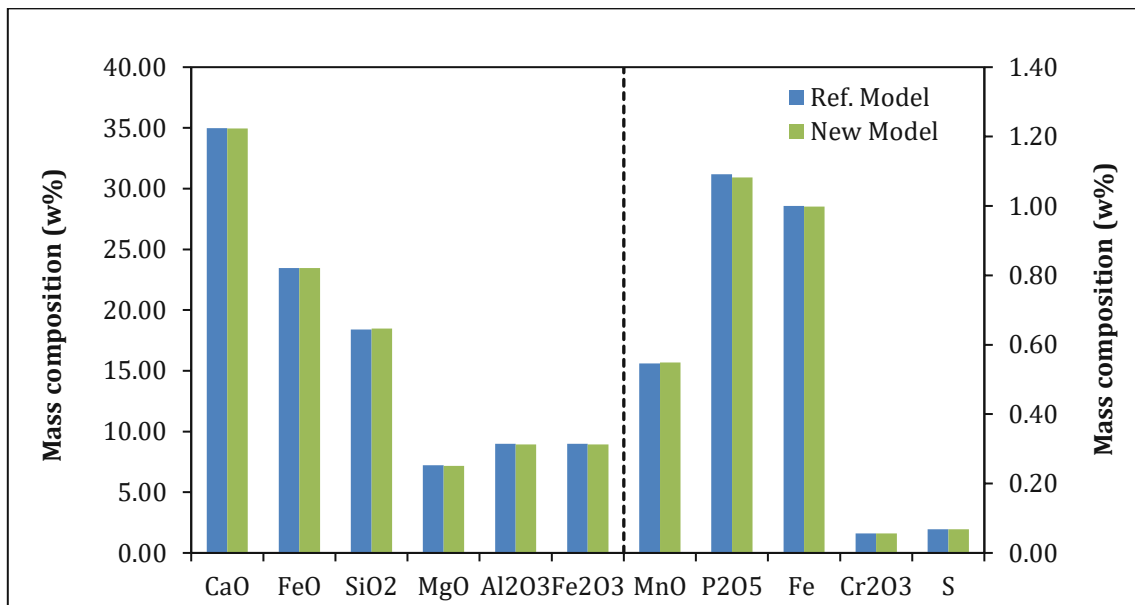


Figure 36: Slag composition for case 1. New EAF process model (green) compared to the ref. model (blue). Slag temperature is 1600 °C.

The calculation outputs show no significant deviations to the provided data. For chrome, phosphor manganese and sulphur, the distributions between the slag and steel phase provided by the ref. model were used as input parameters for the new model. The FeO and MnO content of the slag were set as well. The basicity 2 of the slag calculated using

eq. (33) is 1.88 in the ref. model and 1.89 in the new model. The steel temperature is 1620 °C and the slag temperature is 1600 °C.

The off-gas output was compared at the off-gas elbow. The calculation was performed with and without consideration of the water-gas shift reaction (WGSR). Results are shown in Figure 37 and Figure 38.

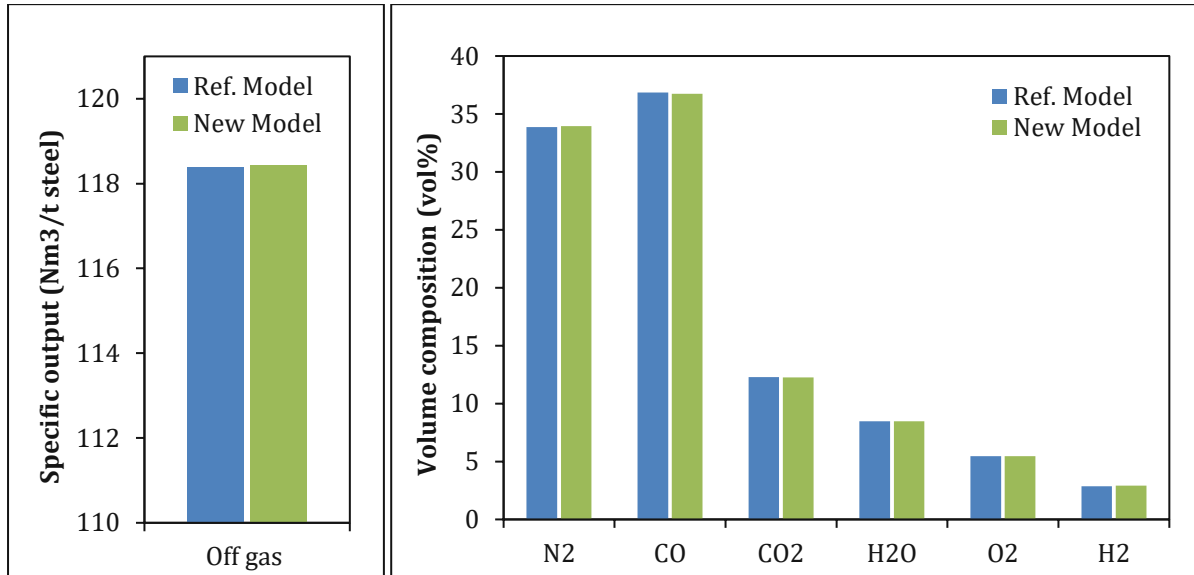


Figure 37: Off-gas volume flow (left) and composition (right) at the off-gas elbow for case 1. New EAF process model (green) compared to the ref. model (blue). Water-gas shift disabled.

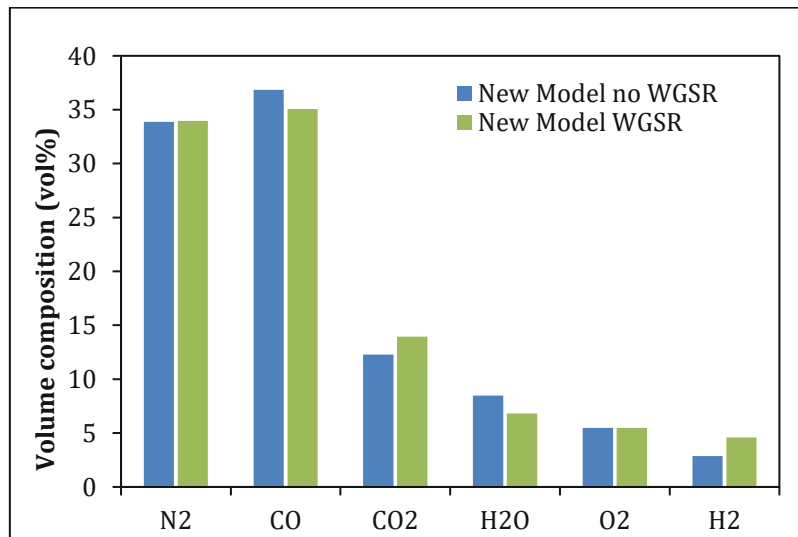


Figure 38 Off-gas composition at the off-gas elbow for case 1. New EAF process model without WGSR (blue) compared to new model with WGSR (green).

The volume flows are in good accordance with the provided data with a deviation below 0.05% (Figure 37). The post combustion degree of CO and H₂ (see eq.(36)) at the off-gas-

elbow was calculated at 34.3% in both the new and the ref. model. The portion of H₂O in the off-gas, which was set to the value given by the ref. model (6.8%) seems high compared to values given in the literature (e.g. [64]). The WGSR is not considered in the ref. model and it was turned off for the calculation results seen in Figure 37. Considering that in the validation based on plant data, (chapter 4.3), the WGSR is turned on and for comparison, the off-gas composition was calculated again with WGSR (Figure 38). As a result, about 4.8 vol. % of the CO was shifted to H₂. At an off-gas temperature of 1489 °C, the reverse WGSR should be dominant, but a high amount of H₂O in the form of steam still shifts the reaction in the direction of hydrogen formation. It can be assumed, that the composition provided by the ref. model did not represent equilibrium conditions with regards to the WGSR. However, since real-life measurements of the off-gas composition at the off-gas elbow were not available and since it is unclear to what extent equilibrium conditions are reached in the gas phase at this point of the EAF process, it cannot be concluded which modelling approach yields better results.

Energy Balance

To compare the energy balance calculated by the EAF process model and the reference model, some adjustments were required. The ref. model uses standard enthalpies of chemical reactions to determine the chemical energy input and calculates a heat loss based on heat conduction losses, radiation losses and electrical losses. The calculations for the losses are based on furnace geometry, operation parameters and empirical constants. The new model equates the energy balance using the specific enthalpy of in- and outputs. For better comparison of the chemical energy input, the enthalpies of the most important reaction in the new model were also calculated using specific reaction enthalpies (see chapter 3.2). For this validation, the heat loss was set to the value provided in the ref. model and the electric energy demand was determined by the new model by closing the energy balance. The black box was chosen as the system boundary for the energy balance, since the electrical energy demand and the heat loss for the new model are calculated in the black box sub-model.

Both models consider the energy of slag formation and dissolution by using specific enthalpies, but they use slightly different approaches. The ref. model does consider scrap dissolution, but not DRI dissolution for the calculation of the dissolution energy. The reasons for this are unclear and it might be a mistake in the ref. model. The hot DRI input has a temperature of about 600°C and should melt and dissolve similar to scrap. Because

case 1 uses 80% DRI as ferrous input, this results in an underestimation of the dissolution energy. There are also minor differences in the sensible heat calculation of in- and output streams, probably due to the use of different thermodynamic databases. The calculation output is shown in Figure 39 to Figure 41.

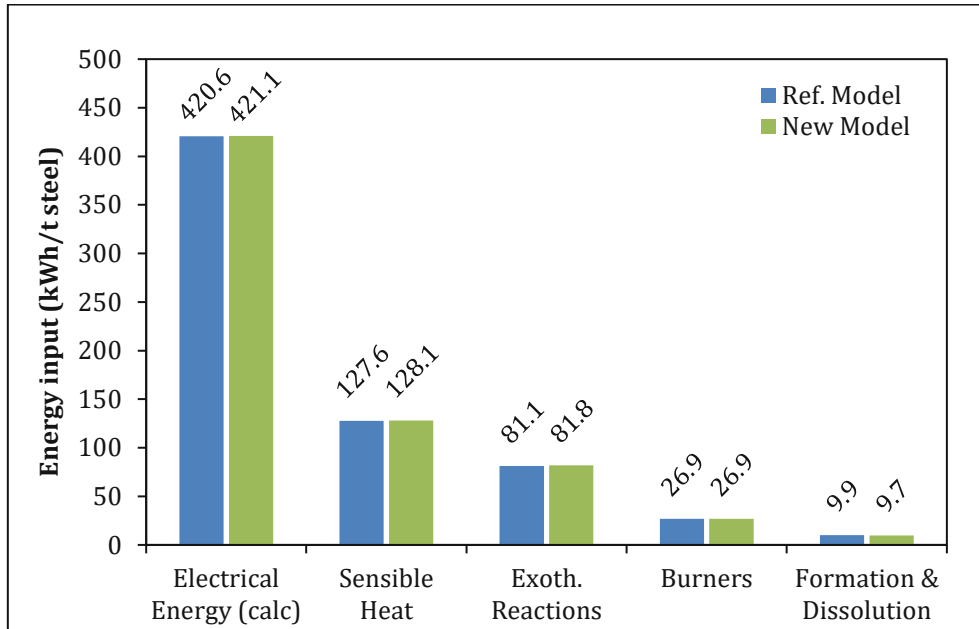


Figure 39: Energy inputs for case 1. New EAF process model (green) compared to the ref. model (blue). Electric energy demand is calculated based on a set heat loss.

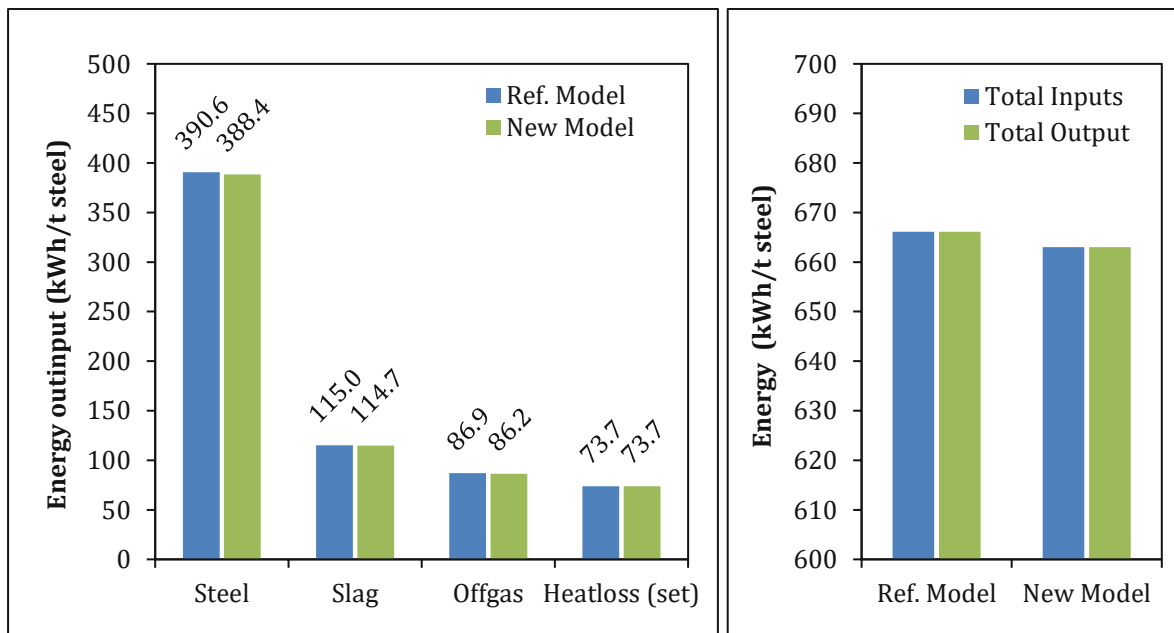


Figure 40: Energy outputs (left), and total energy in- and outputs (right) for case 1. New EAF process model (green) compared to the ref. model (blue); The heat loss is set to the value provided in the ref. model.

When looking at the calculated energy inputs as seen in Figure 39 it can be concluded that the models delivered comparable results, with an abs. deviation of only 0.1% in the electrical energy input. The abs. deviations regarding the exothermic reactions (0.9%) and the sensible heat of inputs (0.4%), can be explained since not all reactions considered in both models, and slightly different thermodynamic data was used.

The simulation results for the energy outputs (Figure 40, left) matched their target values well (abs. deviations: steel 0.2%, slag 0.5%, off-gas 0.1%). A good fit for the total energy in- and outputs (Figure 40, right) was achieved with an abs. error of less than 0.3%. The metallurgical model heats all the dust to 1450°C, while in the new model, the dust created from solid inputs by the dust splitters has the same temperature as the inputs (e.g., 25 °C for dolomite) and is heated and oxidized in the post combustion. Since the post combustion takes place outside of the black box, the energy needed to heat the dust was considered in the energy balance of the black box to compensate this difference. A visualisation of the simulation result for all energy flows of the new model is shown in Figure 41. Potential chemical energy is not included in the in- or outputs.

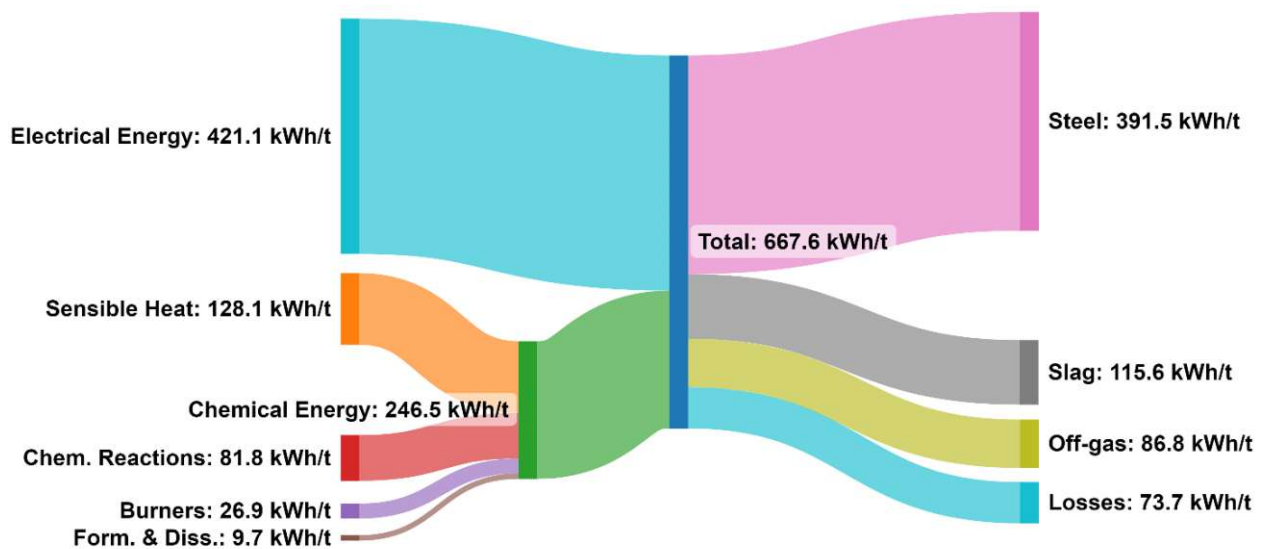


Figure 41: Simulation results of the energy flows for case 1. System boundary is the black box model. Outputs include sensible heat only.

According to the simulation, electrical energy accounts for 63% of the total energy input and 59% of the energy output is in the form of enthalpy of the liquid steel. The results are in good accordance with comparable calculations found in the scientific literature, which defines the enthalpy of the liquid steel as the usable energy output and suggest a range of 45-60% [16] for it.

4.2.2 Second Operation Scenario

Mass Balance

In order to test the new models' capabilities to handle different ferrous input materials, another case was calculated, using scrap, DRI, hot metal as well as a hot heel. The liquid hot heel consists of slag and steel phases. The solid inputs for operation scenario 2 can be seen in Figure 42, and the gaseous inputs and solid by-products are depicted in Figure 43.

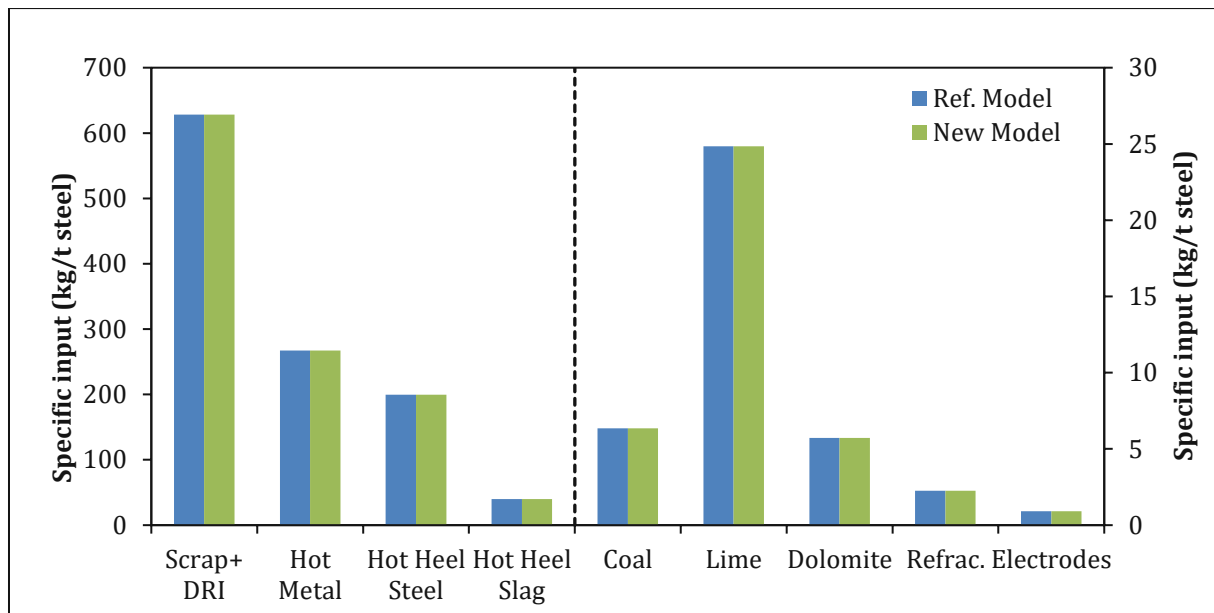


Figure 42: Ferrous (left) and other solid inputs (right) for case 2. New EAF process model (green) compared to the ref. model (blue). Refrac. = Refractory. Scrap and DRI inputs(left) are calculated based on a set steel production. Other values are set.

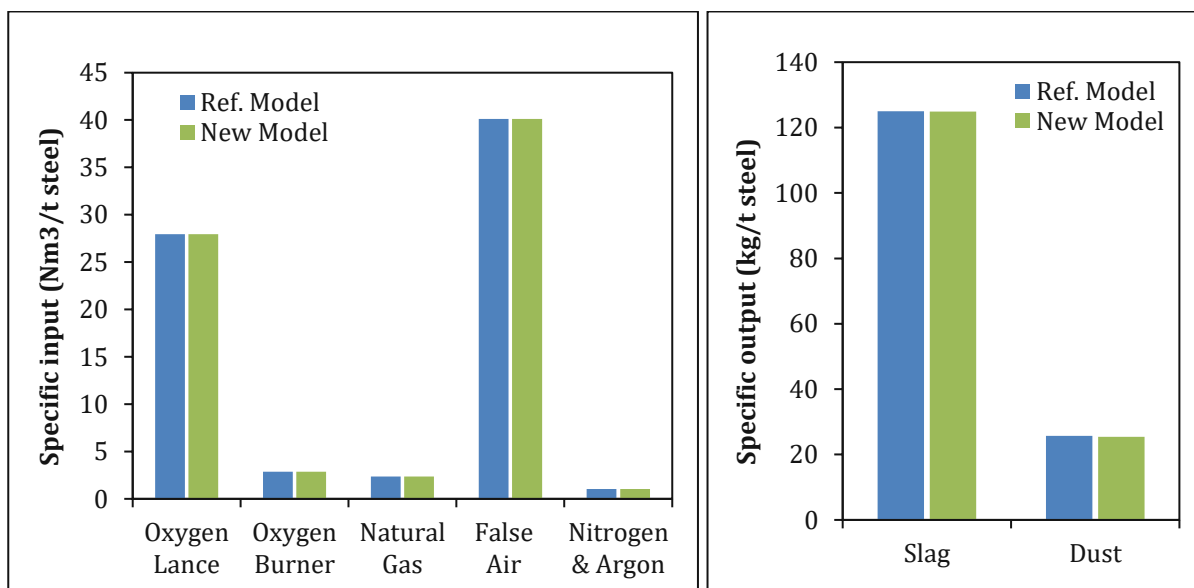


Figure 43: Specific gaseous inputs (left) and other by-products (right) for case 2. New EAF process model (green) compared to the ref. model (blue). Inputs are set and outputs are calculated.

The amount of Scrap and DRI needed to meet a set steel production was calculated, with an absolute deviation of 0.01% as shown in Figure 42. The other ferrous inputs as well as the other solid and gaseous inputs (Figure 43) were set. Analogue to case 1, the calculated dust amount of case 2 deviates by about 1% (abs.%) (Figure 43). This is due to different methods of dust creation explained in section 4.2.1. The calculated slag amount fits the results of the ref. model with no significant deviations (Figure 43).

Simulation results of the new model for the steel and slag compositions are shown in Figure 44 and Figure 45.

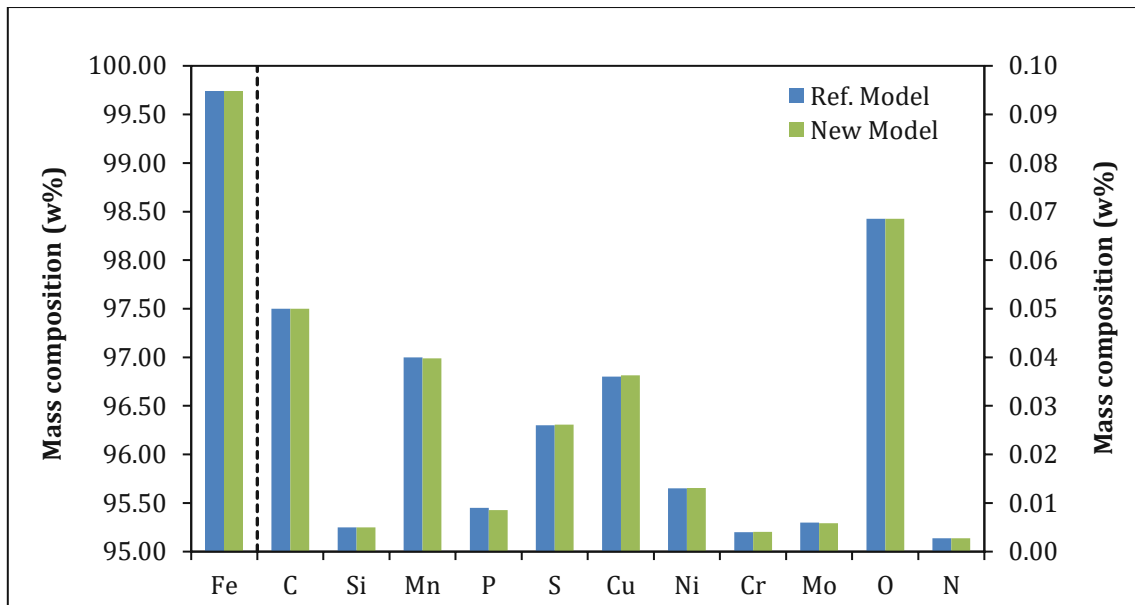


Figure 44: Steel composition for case 2. New EAF process model (green) compared to the ref. model (blue). Steel temperature is 1620 °C.

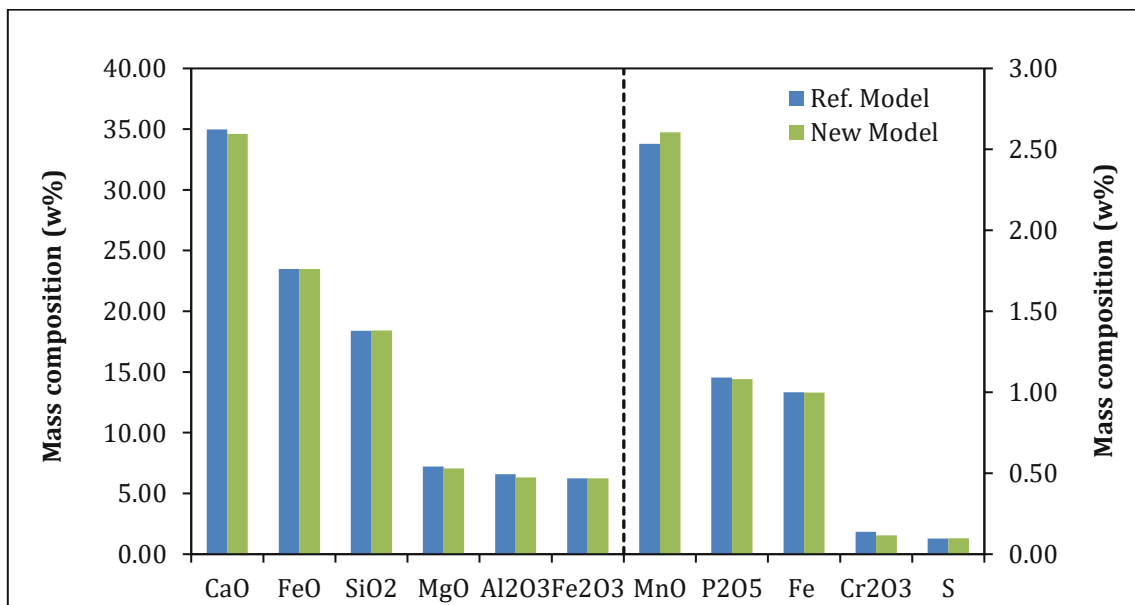


Figure 45: Slag composition for case 2. New EAF process model (green) compared to the ref. model (blue). Slag temperature is 1600 °C.

The simulation results are consistent with the results of the ref. model. Set input parameters were the amount of FeO and MnO in the slag as well as C and Si in the steel phase. The element distributions between the steel and slag phase for sulphur, chrome, manganese and phosphor were also set to their target values from the ref. model. The resulting slag basicity Z is 2.33 for both models. The simulation results show that the new model can accurately calculate steel and slag compositions even when using multiple different ferrous inputs if the element distributions and inputs are set correctly.

The comparison of the off-gas volume flow and composition is shown in Figure 46 and Figure 47.

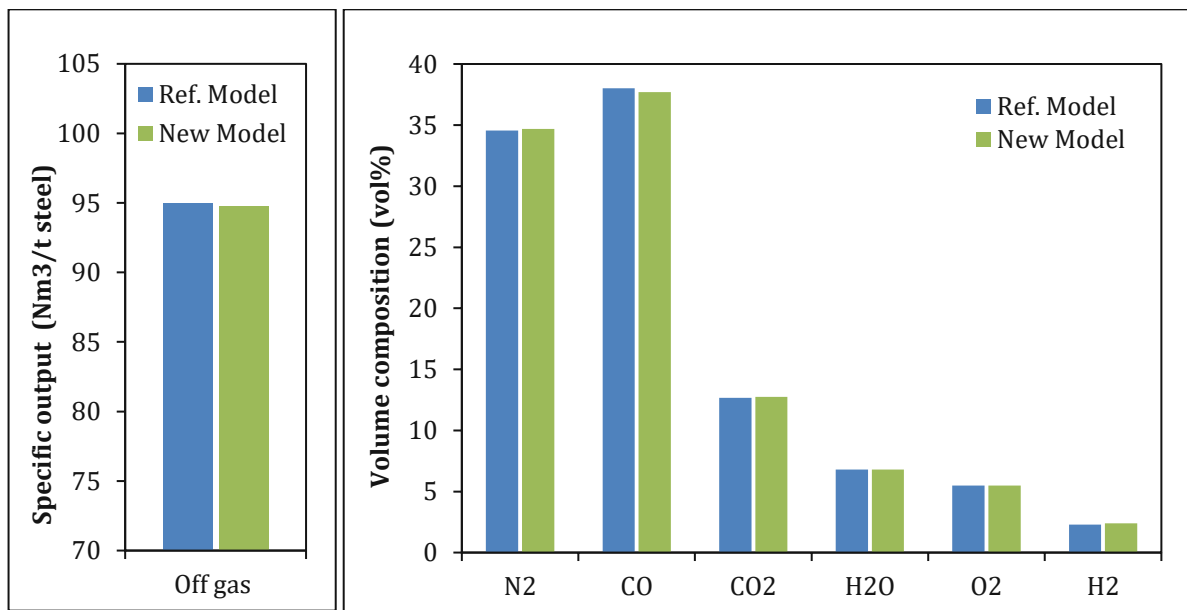


Figure 46: Off-gas volume flow (left) and composition (right) at the off-gas elbow for case 2. New EAF process model (green) compared to the results of the ref. model (blue). WGSR disabled.

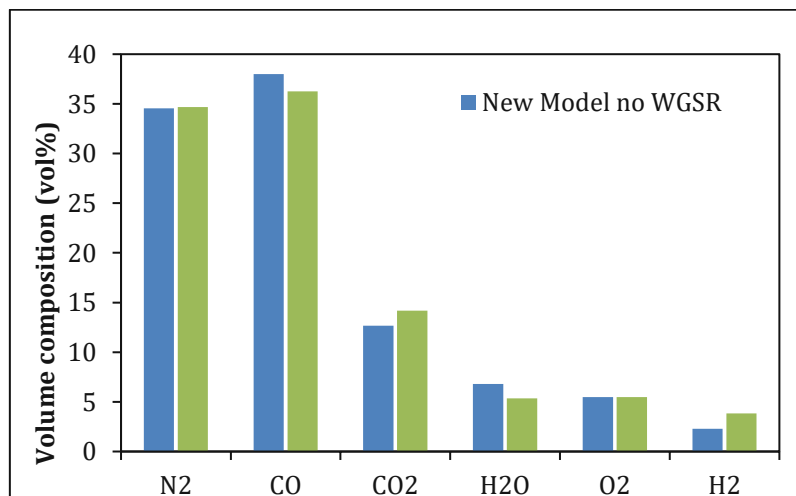


Figure 47: Off-gas composition at the off-gas elbow for case 2. New EAF process model without WGSR (green) compared to new model with WGSR (blue).

The specific off-gas output at the off-gas elbow deviates by about 0.25% (abs.%). The results for the post combustion degree at the off-gas elbow was 34.8% in the new and 34.6% in the ref. model. Considering the gas composition, a satisfying fit to the provided ref. calculations was achieved as shown in Figure 46. For comparison, the off-gas composition was also calculated considering the water-gas shift reaction and similar to case 1, about 4.9 vol.% of the CO was shifted to H₂ at an off-gas temperature of 1489 °C.

Energy Balance

The energy balance was validated in the same manner presented in chapter 4.2.1. The calculated energy in- and outputs are shown in Figure 48 and Figure 49, respectively.

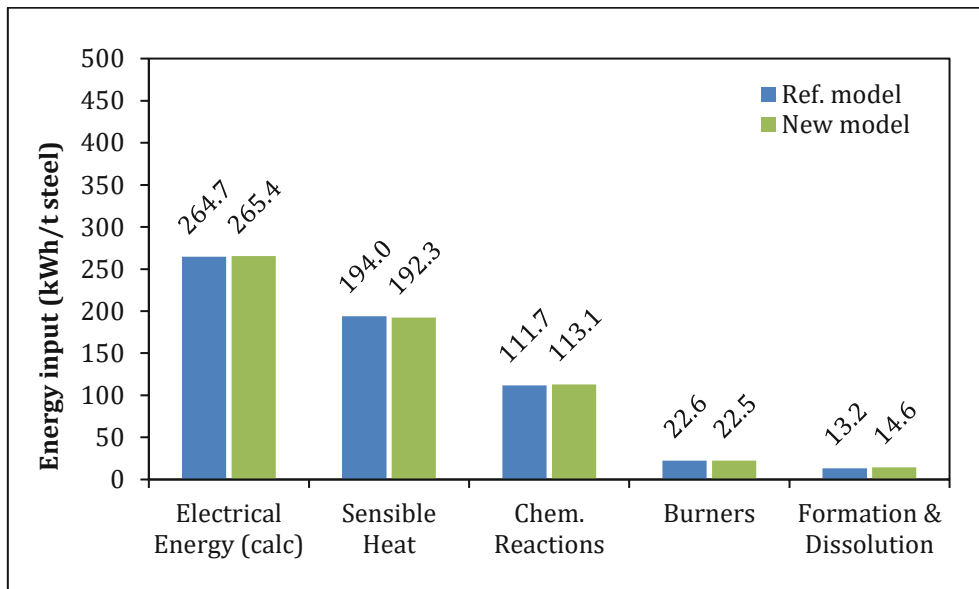


Figure 48: Energy inputs for case 2. New EAF process model (green) compared to the ref. model (blue). The electric energy demand is calculated based on a set heat loss.

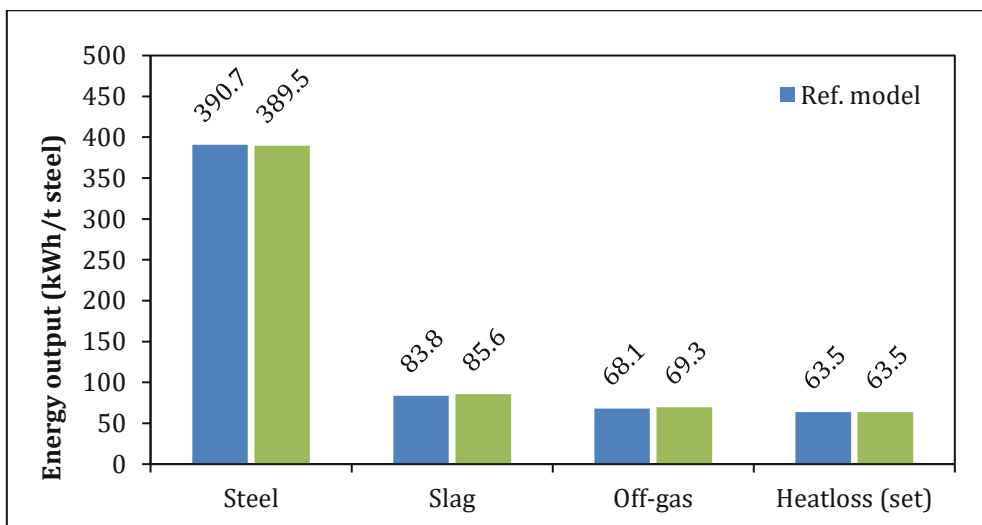


Figure 49: Energy outputs for case 2. New EAF process model (green) compared to the ref. model (blue). The heat loss is set to the value provided in the ref. model.

Since case 2 uses hot metal, the sensible heat input is about 65% higher compared to case 1, and the electric energy demand is about 60% lower (Figure 48). Less slag is produced compared to case 1, because the hot metal already has a metallic iron content of 94% while the DRI used in case 1 only has 85% and includes more gangue. This results in a smaller energy amount from slag formation as well as less energy output through the slag phase (Figure 48).

Compared to the ref. model there are some minor differences in the calculated energy of the slag, steel and off-gas output (Figure 49, abs. deviations: steel 0.3%, slag 2.1%, off-gas 1.75%), as well as the formation and dissolution energies. The calculated sensible heat is about 1% lower and the heat introduced by the exothermic chemical reactions is about 1.3% higher than their target values as shown in Figure 48. The deviations are caused by differences in the underlying thermodynamic data and in the modelling approach as discussed in section 4.2.1. The higher calculated outputs in the new model led to a slightly higher calculated electrical energy demand, showing an abs. deviation of about 0.3%.

Ultimately, the simulation results fit the provided data sufficiently, with the total in and outputs (Figure 50) and the calculated electric energy demand (Figure 48) both showing absolute deviations of less than 1%.

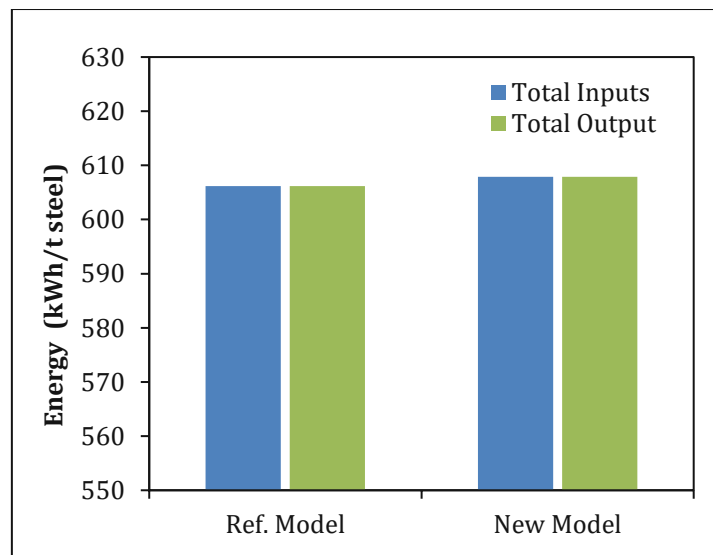


Figure 50: Total energy in- and outputs for case 2. New EAF process model (green) compared to the ref. model (blue).

The simulated energy flows of the new model are depicted in Figure 33. In case 2, the electrical energy accounts for only 44% of the total energy input. This is expected since the sensible heat input of the hot metal yields about 32% of the energy demand for the process.

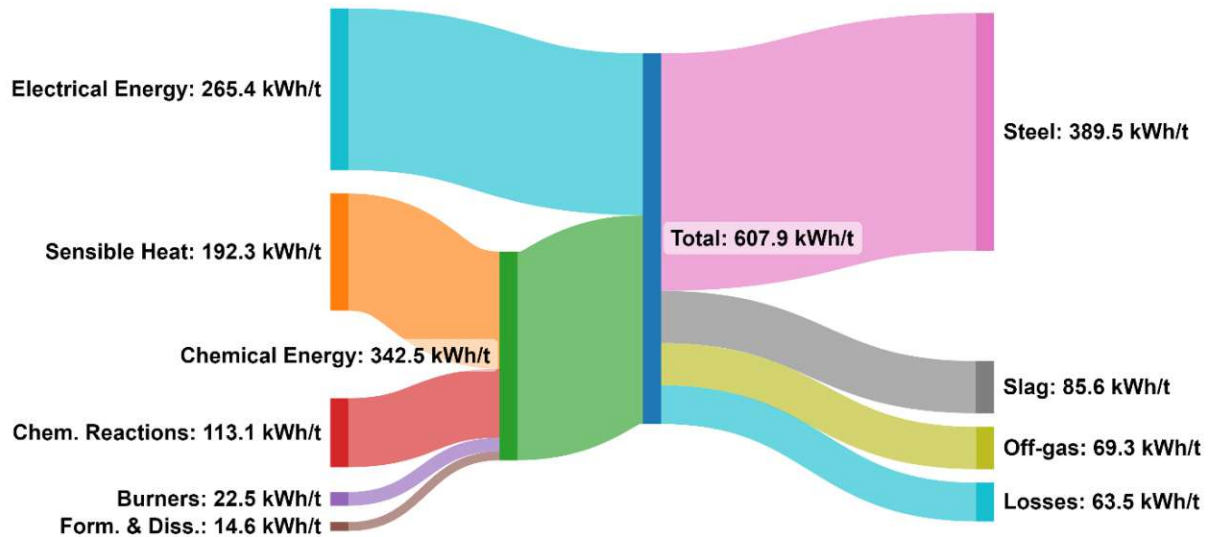


Figure 51: Simulation results of the energy flows for case 2. System boundary is the black box model. Outputs include sensible heat only.

The usable energy output as liquid steel is comparably high with 64%. This can be explained by the use of hot metal, which already has a high metallisation, less gangue and less carbon content, leading to less slag formation and less off-gas compared to case 1.

4.3 Validation Using Plant Data

As part of a larger metallurgic simulation platform, the EAF process modelling will be used in the planning and optimisation of real-life, industry-scale steelmaking operations. To prove its capability in this regard, the developed model was also validated using three individual heats as well as average data from eight heats of the Quantum EAF from the received plant data. Specifications for the used EAF were provided by Primetals Technologies Austria GmbH (Tab. 27).

The Quantum EAF uses 100% Scrap as ferrous input and the input composition for every heat had to be calculated individually. The composition for six different scrap types and corresponding factors for typical mechanical losses were included in the plant data. For the calculation of the scrap input composition, all scrap additions of each scrap type in the furnace for an individual heat were summed up. The total composition was then calculated using the provided analysis for each scrap type proportional to the share of that scrap type in the ferrous input of the heat. This procedure represents a potential source for error since the scrap composition is not homogenous and mechanical losses may vary from heat to heat.

Information on the slag, dust and off-gas amount as well as a dust or off-gas analysis were not provided in the plant data. The samples for the steel and slag analysis were taken about 14 minutes before the end of tapping. Accordingly, the results represent the steel and slag compositions at a given moment, but not the mean endpoint composition of the tapped steel. The values for the species distributions of elements between the steel and the slag phase were calculated from the averages of the provided analysis and set as input parameters for the validation.

Since there was no information provided on the size or composition of the hot heel, it was assumed that the hot heel does not change significantly in size or composition between heats. The flowrate of the scrap inputs was calculated based on a set steel production and other inputs were set according to the plant data. Missing process parameters were assumed based on literature values (Tab. 28). The specific electrical energy demand as well as the specific heat loss were calculated using the built in data-driven model developed as part of this work. An overview of the provided and calculated output parameter can be seen in Tab. 29. In the following section, results of the new model will be compared to the given plant data.

Tab. 27: Provided specifications of the industrial EAF [30].

Furnace Specifications	
EAF type	Quantum
Furnace tap weight	80 t
Hot Heel	70 t
Transformer Rating	60 MVA
Operation	Batch
Scrap charging	3 Buckets
DRI/HBI charging	possible
Hot Metal charging	no
Scrap/DRI preheating	yes, in the shaft
Burners	1 RCB, 1 FAST, 1 PC
Tap-to-tap time	41 min
Productivity	120 t/h max

Tab. 28: Input parameters for the model validation using plant data.

Plant data input parameters	Assumed input parameters
Steel production	Dust losses for solid inputs
Slag formers quantity and composition	Air, N ₂ and Ar input quantity
Lanced and injected O ₂ volume	Refractory and Electrodes consumption
Burner gas volume	Gas dissolution of O, N and H in steel
Steel temperature	Distributions for S, Cr, Mn, P
C and Si content of steel	Steel and slag spitting degree
Slag FeO content	Steel evaporation degree
Tap-to-tap time	Slag temperature
	Off-gas temperature at mouth
	Off-gas O ₂ vol%, composition at mouth

Tab. 29: Output parameters of the plant data and the process model.

Plant data output parameters	Process model output parameters
Scrap consumption	Scrap consumption
Steel composition	Steel composition
Slag composition	Slag composition
Electric energy consumption	Electric energy consumption
Chemical energy consumption	Chemical energy consumption
	Slag quantity
	Off-gas quantity and composition
	Dust quantity and composition
	Post combustion degree at mouth

4.3.1 Average Heat

Mass Balance

The results for the specific scrap demand of the average heat fitted the provided plant data well. The simulation result of the new model (Figure 52) was 0.13% lower than the average value of the plant data. Since no data was provided, the specific nitrogen and argon inputs used for stirring of the metal bath were set to 0.15 and 0.09 Nm³/t steel. Other inputs were set to the average values according to plant data.

A specific solid output of 127.2 kg slag and 21.5 kg dust per ton of steel (Figure 52, left) as well as an off-gas output of 152.8 Nm³ per ton of steel at the off-gas elbow were calculated. Since there was no information on the off-gas and slag amount provided in the plant data, these simulation results for the solid outputs were compared to general reference values received from the EAF specialists at Primetals Technologies Austria GmbH (Figure 52, left).

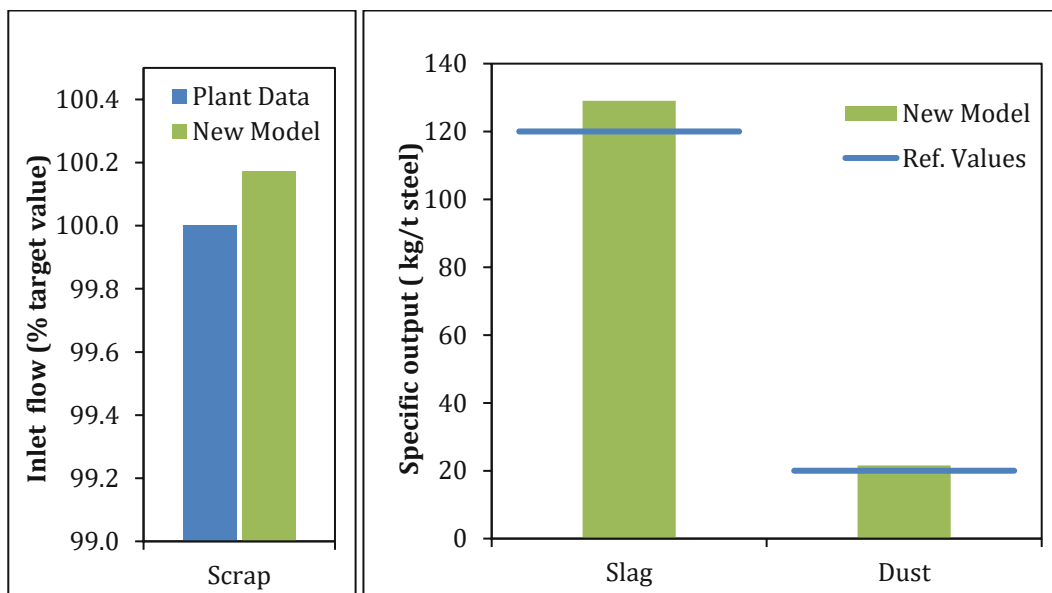


Figure 52: Scrap input (left) and solid by-products (right) for the avg. heat. New EAF process model (green) compared to the provided plant data (blue).

As discussed before, the samples for the steel and slag analysis provided in the plant data were taken at the start of tapping and since no other data was provided, the calculation results representing the steel and slag compositions at the given timepoint were used for the validation. The results are provided in Figure 53 and Figure 54.

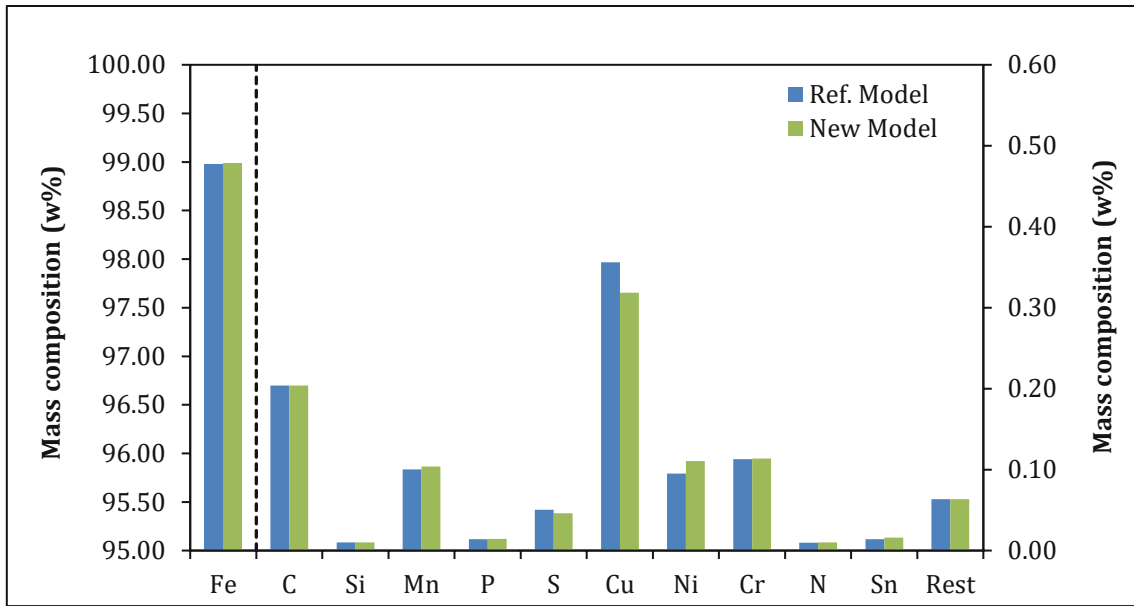


Figure 53: Steel composition simulation for the avg. heat. New EAF process model (green) compared to the provided plant data (blue). Steel temperature is 1613 °C.

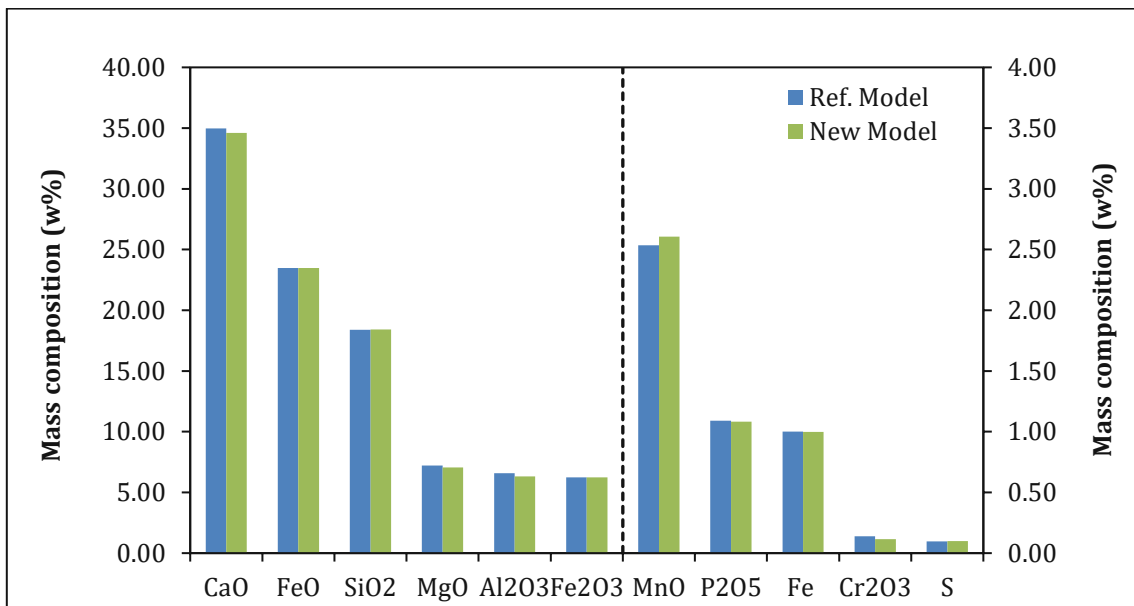


Figure 54: Slag composition simulation results for the avg. heat. New EAF process model (green) compared to the provided plant data (blue). Slag temperature is 1600 °C.

Considering the quality of the data, the results match their target values with sufficient accuracy, showing only small discrepancies. Most noticeably, the calculated steel composition includes 0.02 w% more nickel, 0.01 w% more iron and 0.046 w% less copper than the steel analysis from the plant data suggests. A possible cause for this is errors in the input analysis of the scrap. Possibly, the scrap contains, for example, more copper or less chromium than assumed. Another possibility is that the steel analysis is inaccurate. However, small deviations like this and also the small deviations for the other elements

are to be expected when dealing with real operational data and the accuracy of the model is comparable to models found in the scientific literature (e.g. [51, 52]).

The average phosphorous distribution between the steel and the slag phase ($P_{Dist} = w_{P,slag}/w_{P,steel}$, see Tab. 7) was calculated at 12.5. This low value indicates that the dephosphorisation process was not finished by the time the steel and slag samples were taken or that in this operation scenario the dephosphorisation takes place later in the ladle furnace, where the crude steel from the EAF is further refined. For comparison, the phosphorous distributions provided by the metallurgical tools (see section 4.2) was on average 56. However, it must be considered that the validation using the ref. model features a different type of EAF and different operation scenarios. The same is true for the manganese, sulphur, and chrome distributions (Tab. 30). Considering all this, the calculated slag composition fitted the provided plant data reasonably well. The off-gas composition at the off-gas elbow is shown in Figure 55.

Tab. 30: Comparison of the average element distributions between the steel and slag phase for the validation using plant data and for the validation using metallurgical tools.

	Plant Data Average	Ref. Model Case 1
P Distribution	12.50	55.60
Mn Distribution	45.57	54.99
S Distribution	1.58	3.42
Cr Distribution	12.00	19.51

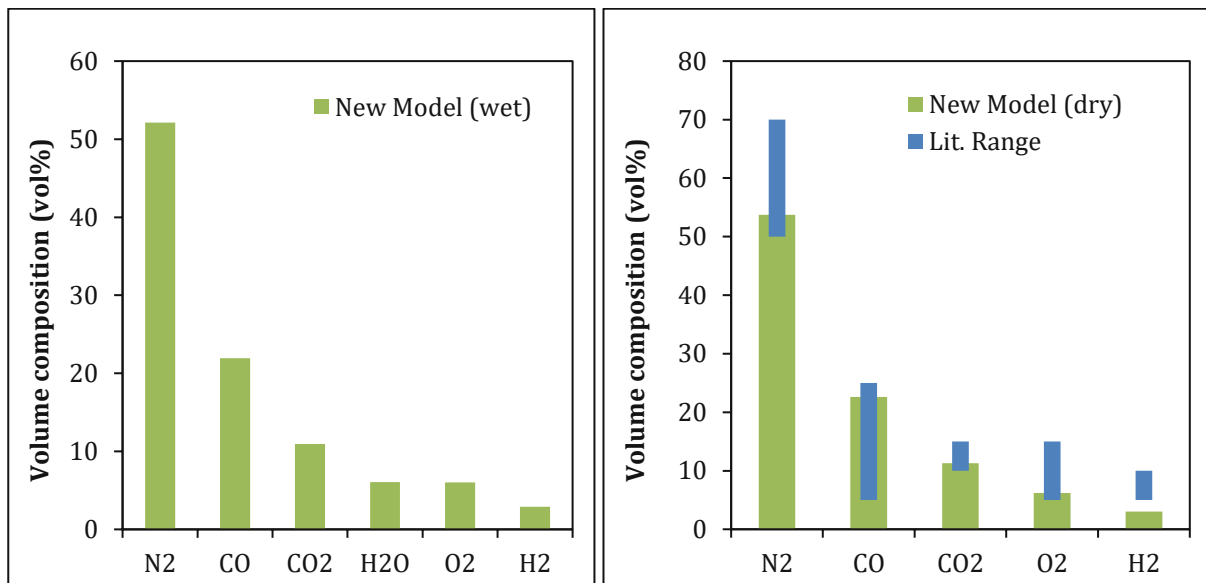


Figure 55: Off-gas composition for the avg. heat. Simulation results of the new EAF process model as calculated at the off-gas elbow (left). Comparison of the calculation results for dry off-gas to ranges from the scientific literature [13](right). Water-gas-shift enabled.

The water–gas shift reaction was simulated and equilibrium conditions were assumed. If equilibrium conditions are reached in the off-gas phase at this point is unclear. The O₂ content at the off-gas elbow was set to 6% according to data from ref. models. The off-gas temperature was set to 1600 °C and the calculated post combustion degree at the off-gas elbow was determined by the model at 42.14%. The simulation output for the average off-gas composition can be seen in Figure 55.

Because there was no off-gas analysis in the plant data, the results were compared to scientific literature, which suggest off-gas temperatures between 1200 and 1750 °C [65] and a composition of approximately 55% N₂, 30% CO, 10% CO₂ and 5% H₂ (vol%) for dry off-gas [23]. All simulation results except H₂ are inside the literature range. The reference model also suggests a H₂ content of 2.9% for case one and two. To fully validate the off-gas composition plant measurements regarding this specific operation would be necessary.

Since the quantum EAF guides the off-gas through the shaft to preheat scrap, it can be assumed a that further post combustion as well as oxidation of oils, paint and impurities in the scrap take place inside the preheating shaft. However, since there was no information available for the off-gas temperature, composition or the temperature of the preheated scrap, these phenomena cannot be validated. If more data is available in the future, a separate submodel for the preheating chamber could be implemented in the EAF process model. According to literature [25], a heat recovery efficiency of 55% can be assumed.

Energy Balance

For the validation of the energy balance, the black box model was chosen as the system boundary analogue to section 4.2. As a result, the preheating shaft of the quantum EAF where off-gas heat integration is used for scrap preheating, is not included. Instead of setting a heat loss and calculating the electrical energy demand like in the previous validation, both the heat loss and the energy demand were calculated using the statistical sub-model (section 3.4) to test its accuracy.

The black box model regards the sensible heat from the scrap preheating as an input and takes into account only the physical heat of the off-gas output and not the potential chemical energy that could be released if all the CO were combusted to CO₂. This is congruent with the heat balance used in section 4.2 and approaches found in

literature [13]. The plant data provided values for the measured specific electrical energy demand as well as a specific chemical energy input for each heat. The comparison of the results for the calculated chemical and electrical energy with their target values from the plant data is shown in Figure 56.

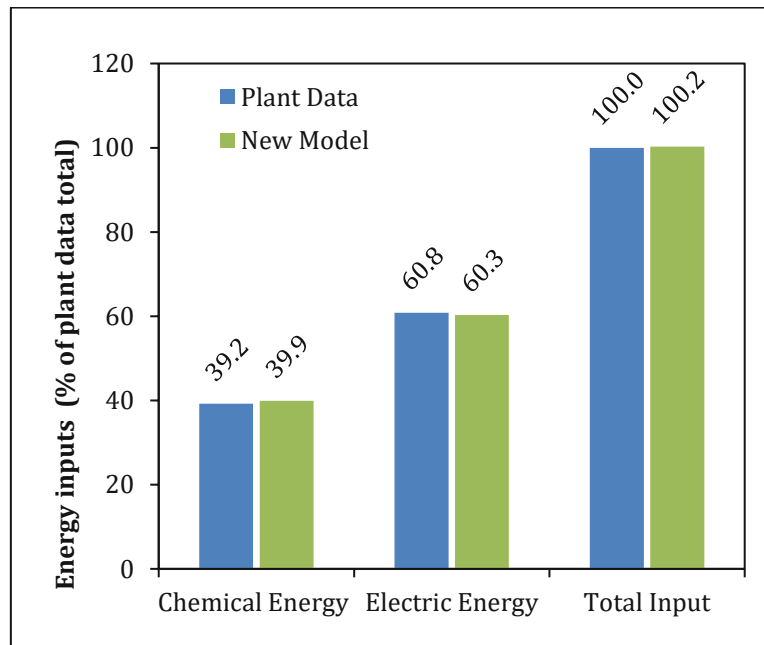


Figure 56: Comparison of the chemical, electrical and total energy inputs for the avg. heat. Simulation results of the new EAF process model (green) compared to the plant data (blue). The total input of the plant data represents 100%.

The simulation results matched the plant data well with only slight deviations. The new model overestimated the specific chemical energy demand by about 0.73% (abs.%). The specific electrical energy demand is underestimated by 0.49% (abs.%). The deviation is 0.24% (abs.%).

The value for chemical energy was calculated by It needs to be considered that the chemical energy is not measured but calculated by an internal process model of the EAF plant. According to the EAF experts who provided the data, it includes the energy of all chemical reactions inside the EAF vessel. This means the chemical energy includes exothermic reaction of the melting and refining process, formation, and dissolution energies as well as energy from the natural gas burners, but it does not include chemical energy from the post combustion in the scrap preheating chamber.

A visualisation of the energy streams is shown in Figure 57. The percent values differ from the ones given in Figure 56, since the scrap preheating temperature was not provided in

the received plant data. The calculation of the energy streams assumes a scrap temperature of 500°C after preheating to consider the sensible heat input from the scrap and to make the output better comparable to the results of the validation using ref. models.

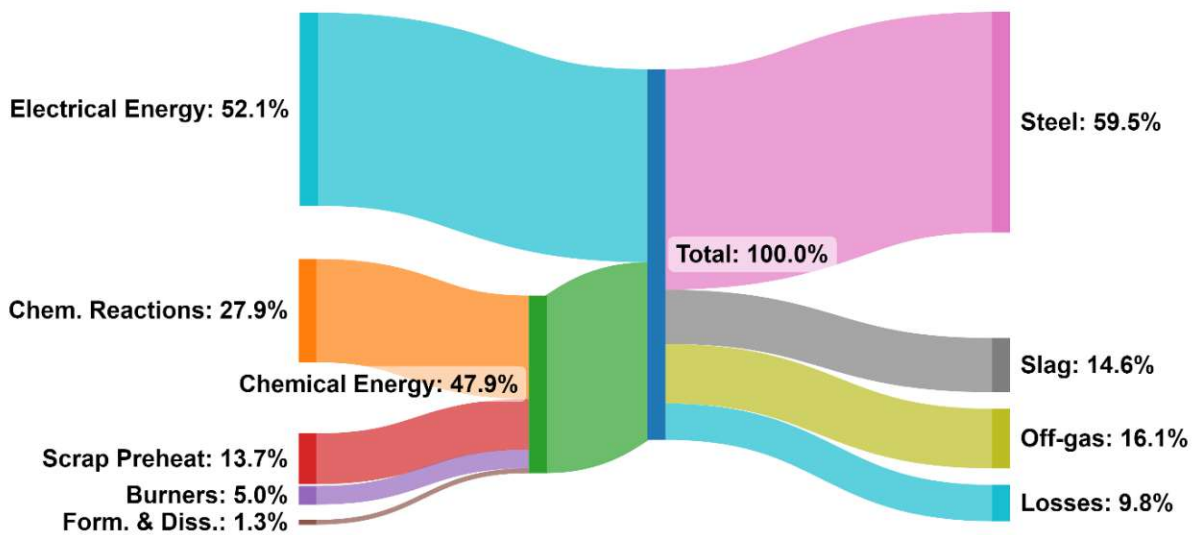


Figure 57: Simulation results of the energy flows for the avg. heat. System boundary is the black box model. Outputs include sensible heat only.

The energy input from scrap preheating was calculated at 13.7% of the total energy input. This result matches well with the scientific literature, which suggests an energy input of 14% [30] from the preheating.

According to the simulation, the electrical energy accounts for 52% of the quantum EAF's total energy input. Compared to the validation using ref. models, this value is between Case 1 of the conventional EAF with 64%, and Case 2 which only used 44% electrical energy because of the use of hot metal as input material. The usable energy output in the form of liquid steel amounts to 59%, which is equal to Case 1 and lower than Case 2 where 64% were reached.

4.3.2 Individual Heats

After the successful validation of the average heat, three randomly selected individual heats from the plant data were simulated as well. The element distributions were set to the values calculated for the average heat. Specific nitrogen and argon inputs for stirring were set to 0.15 and 0.09 Nm³/t steel. Other inputs streams and compositions were set according to the plant data. The slag temperature was set to 1600 °C and the steel temperature was set according to the plant data.

Mass Balance

The specific scrap demand of each heat was calculated based on the steel production (Figure 58, left) and compared to the corresponding target value plant data. The specific calculated output flows for slag and dust are shown in Figure 58 (right). Since there was no dust and slag amount given in the plant data, the simulation results for the solid outputs were compared to general reference values received from the EAF specialists at Primetals Technologies Austria GmbH.

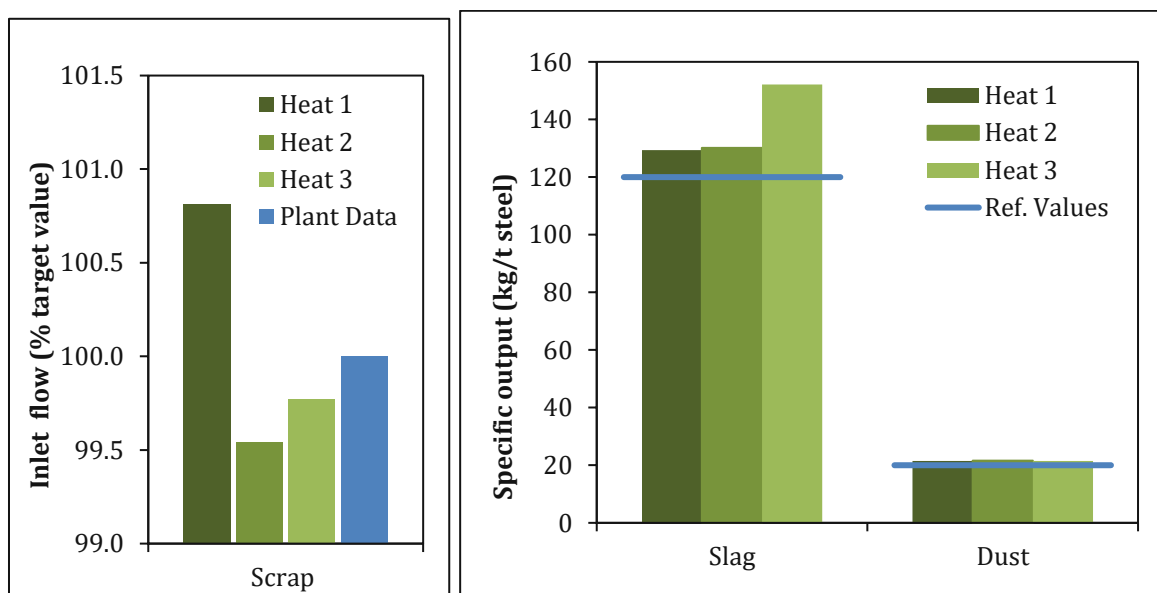


Figure 58: Scrap input (left) and solid by-products (right) for the individual heats. Simulation results (green) compared to the plant data (left, blue) and reference values (right, blue).

The absolute deviations of the calculated scrap input to the target values from the plant data were below 1% for all heats. The calculated steel and slag compositions are shown in Figure 59 and Figure 61. The deviations from the received plant data are shown in Figure 60 and Figure 62, respectively.

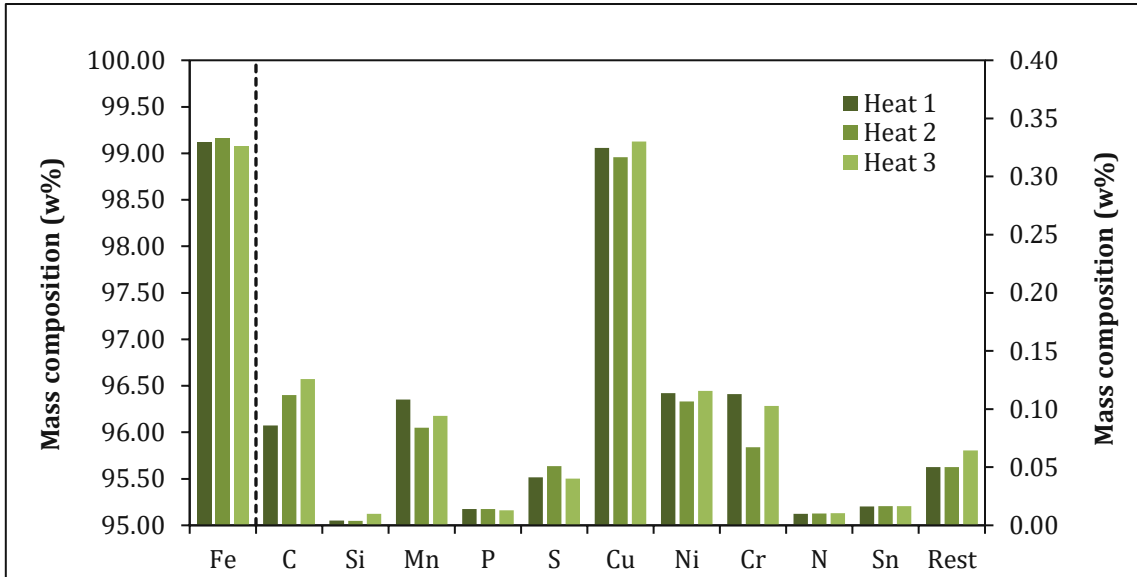


Figure 59: Steel composition for the individual heats. Simulation results of the new EAF process model. Steel temperature is between 1598 and 1649 °C.

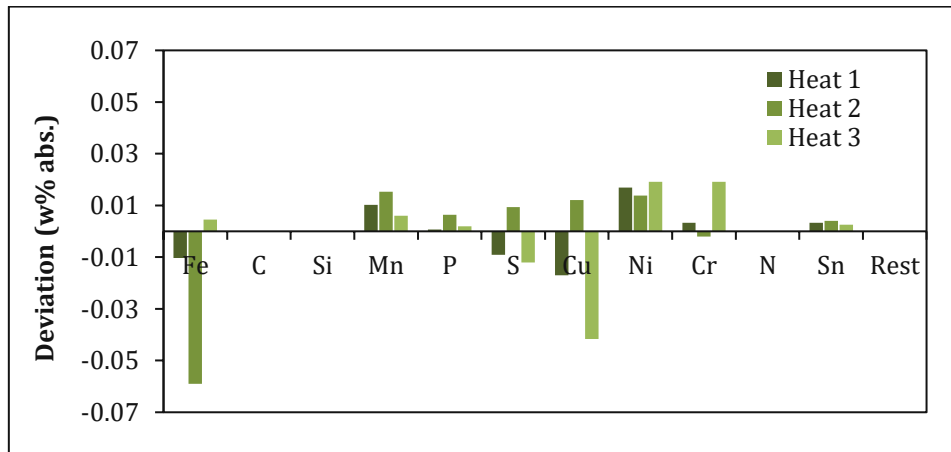


Figure 60: Deviations for the steel composition. EAF process model vs. plant data.

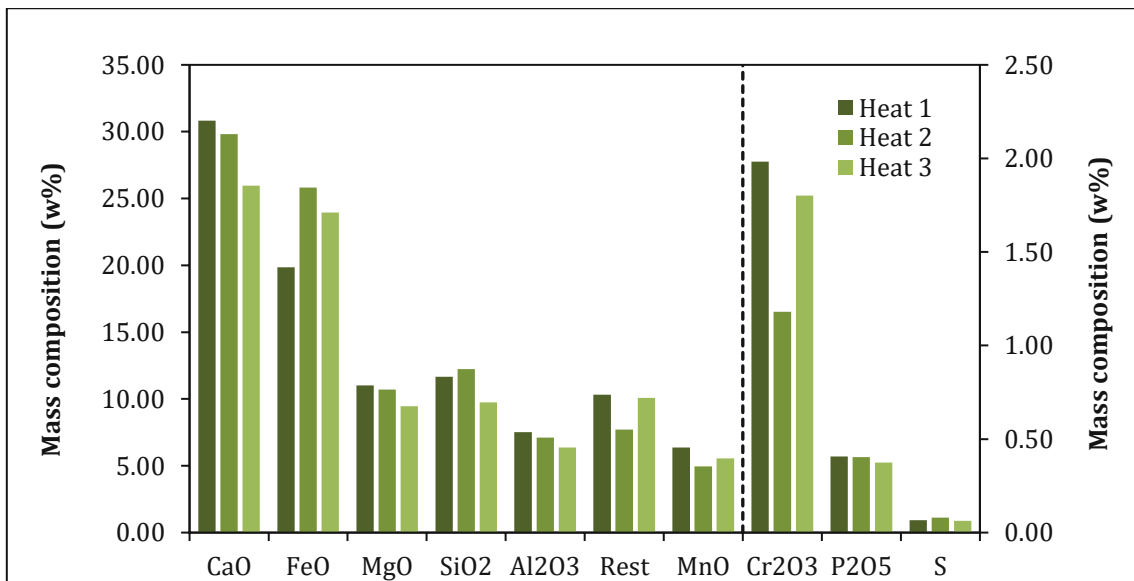


Figure 61: Slag composition for the individual heats. Simulation results of the new EAF process model. Slag temperature is 1600 °C.

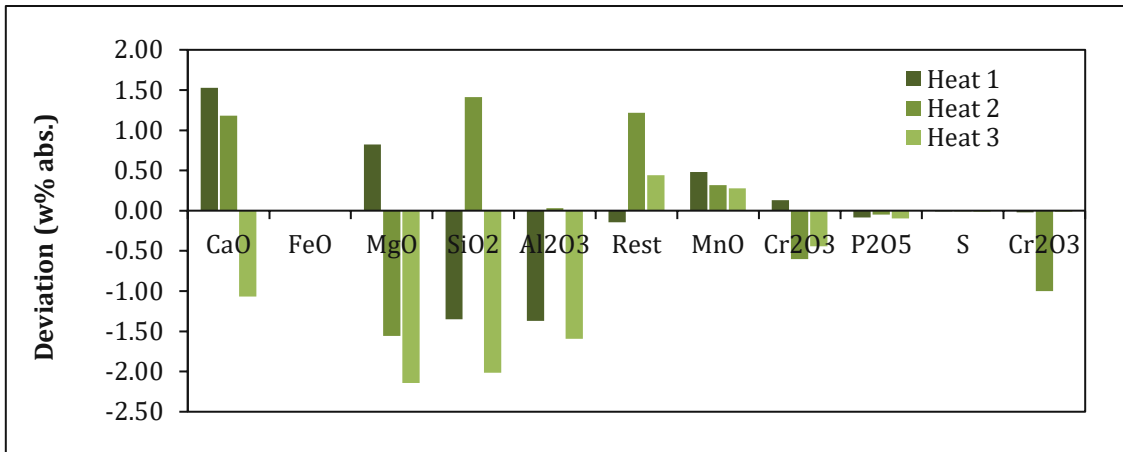


Figure 62: Deviations for the slag composition. EAF process model vs. plant data.

As expected, they show some variation as different scrap input compositions were used. For example, the scrap mix for heat 2 had a significantly lower chrome content, leading to less chrome in the slag and steel. The absolute deviations for all species were below 0.06% for the steel and below 2.5% for the slag composition. Considering the accuracy of the analysis provided in the plant data, with about 10% mass missing in the slag analysis as discussed in section 4.3.1, such inaccuracies are to be expected.

The calculated dry off-gas compositions at the off-gas elbow compared with typical ranges from the scientific literature are shown in Figure 63. The WGSR was considered in the calculation.

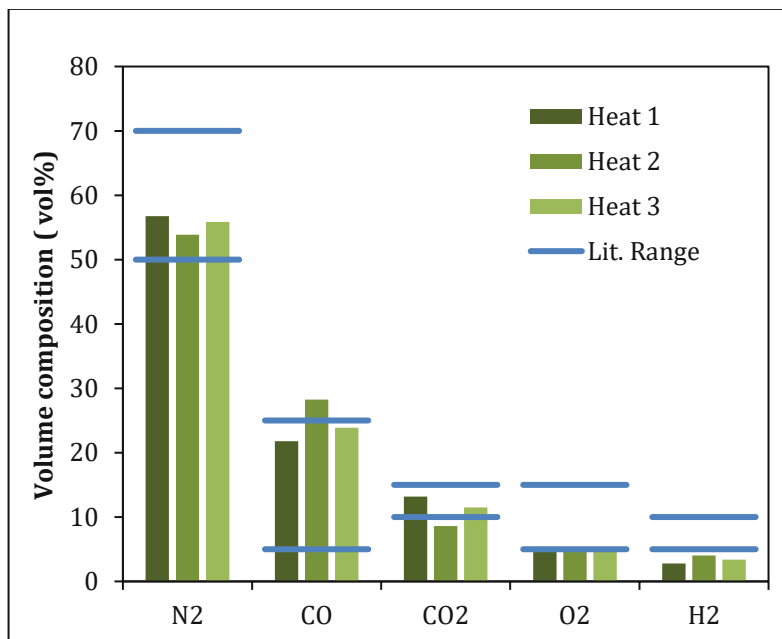


Figure 63: Composition for dry off-gas at the off-gas elbow for the individual heats. Simulation results of the new EAF process model with water-gas shift enabled (green). Literature range for comparison (blue). Off-gas temperature is 1600 °C.

The simulation results for the off-gas amount, the PCD and the off-gas composition cannot be directly compared since there is no such information available in the plant data. The O₂ content and temperature of the off-gas at the elbow were set to 6% and 1600 °C. The post combustion degree was calculated at 45% for heat 1, 30% for heat 2 and 40% for heat 3. As discussed in chapter 4.3.1, not all values are inside the given literature range [23] [65]. For a more in-dept review of the off-gas composition, plant measurements would be required.

Energy Balance

The comparison of the results for the calculated chemical and electrical energy with their target values from the plant data is shown in Figure 64. The calculations were performed analogue to the average heat.

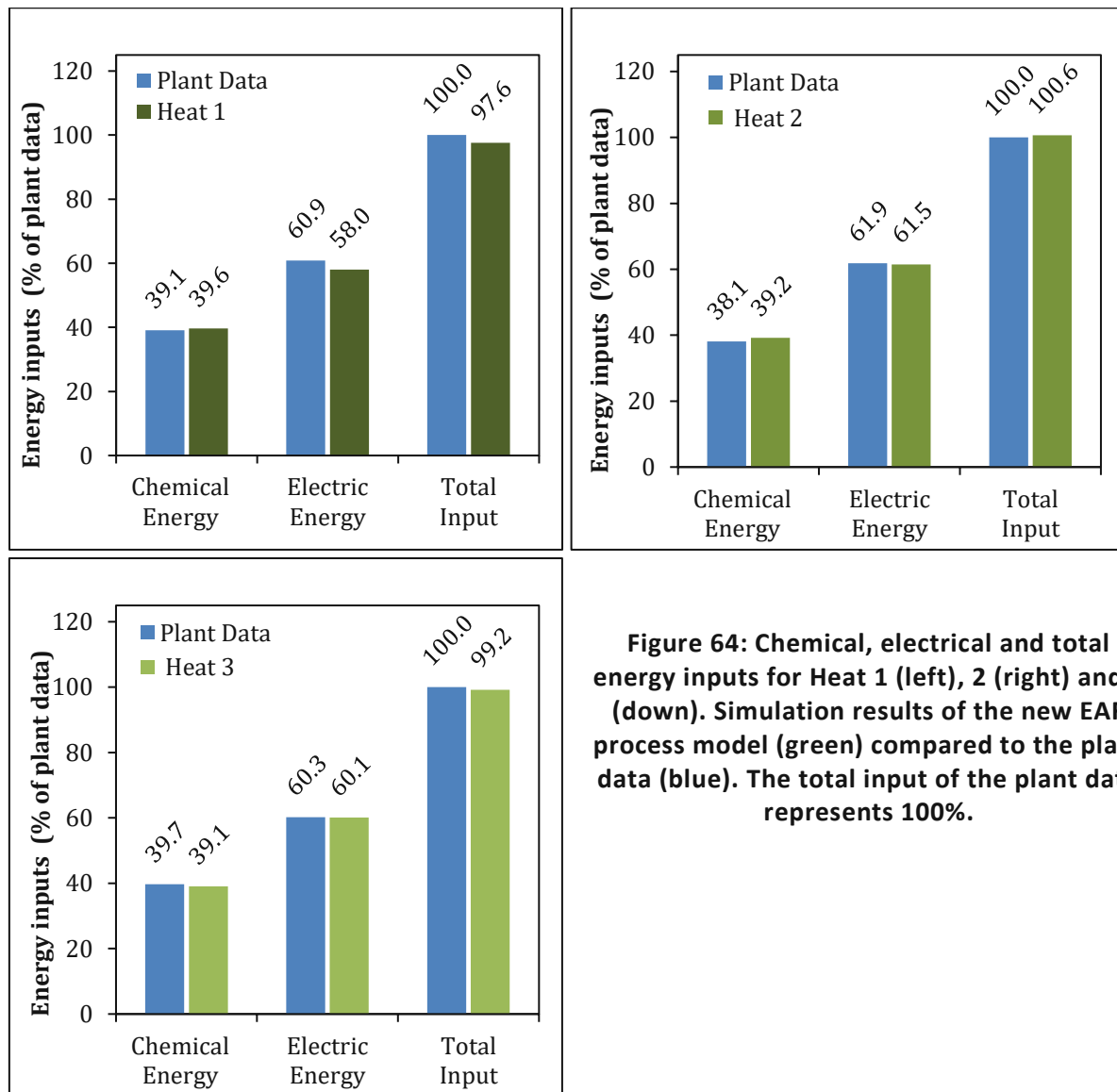


Figure 64: Chemical, electrical and total energy inputs for Heat 1 (left), 2 (right) and 3 (down). Simulation results of the new EAF process model (green) compared to the plant data (blue). The total input of the plant data represents 100%.

The simulation results matched the plant data well with deviations in the expected range. The absolute deviations were between 1.3% to 2.7% for the chemical energy, 0.3% to 4.7% for the electrical energy, and 0.6% to 2.4% for the total energy. Considering the scope of the data and all the presumptions that had to be made, this represents a satisfying result. With a calculated heat loss of about 8.6% of the total energy demand the quantum EAF's heat loss is smaller than the heat loss of the conventional EAF from the validation against ref. models. This seems credible since the conventional EAF uses continuous DRI charging through the 5th hole, which normally leads to a higher heat loss from heat escaping through the hole.

5 Summary & Outlook

Summary

While EAF steelmaking represents the most used steel recycling process in the world, it is still less well understood than oxygen steelmaking in the BOF. In this thesis an EAF process model from the iron and steelmaking model library of Primetals Technologies Austria GmbH was expanded, reworked, and validated. The biggest improvement was the development of a statistical sub-model to estimate the EAF's electrical energy demand from the input materials of the process. The expansion of the model also included the addition of a case selector for the species distributions between the steel and slag phase, reworking of the model's port structure, and initialisation procedures. Accuracy and stability of the EAF model were tested in an extensive validation using results from proven reference models and plant data, comparing mass and energy balances.

The development of the energy demand sub-model used plant data from three different steel manufacturers. The received data was processed and four different modelling approaches, based on the Köhle model and multiple linear regression, were applied and tested. The results fitted the plant data well, with the final model having a regression standard error of only 20 kWh/t, or 5% of an EAF's typical electrical energy demand.

The validation of the process model using results of proven reference models showed no significant deviation for the steel and slag amount and composition and small deviations regarding the by-products and energy balance. These minor deviations can be attributed to general differences in the modelling approaches and the use of different thermodynamic databases for the calculations. The developed EAF model proved its stability and its ability to handle different operation scenarios with scrap, DRI, and hot metal as ferrous inputs.

The model was also validated using the received plant data and results for three individual heats as well as for an eight-heat average. Despite the limited scope, and the usual uncertainties when dealing with plant data, the simulation results for the steel and slag amount and composition and for the energy balance matched their target values to a high degree. As expected, the accuracy of results when simulating averages of multiple heats is higher than the accuracy of the results for individual heats. For example, the specific electrical energy demand showed absolute deviations from the plant data of up to 5% for

individual heats and only 0.5% for the eight-heat average. Since there was no data on the off-gases, the EAF dust or the slag amount, not all model aspects could be fully validated. In conclusion, the accuracy of the new model when simulating real plant operations was proven to be comparable to other process models found in scientific literature.

In contrast to the metallurgical reference tools and most models from literature, the new EAF process model is able to reverse-calculate many input parameters and can easily be connected with other models from a comprehensive metallurgical model library. This gives the new model a significant advantage and enables it to be applied in large flowsheets of complete iron and steelmaking operations.

Outlook

While the analytical capabilities as well as the stability of the EAF model were significantly enhanced in the course of this thesis, there is still room for future improvements. A common challenge in EAF process modelling is the limited scope and availability of plant data, as many parameters are not routinely measured in day-to-day operation.

Since the dataset used for the development of the statistical energy demand sub-model was relatively small compared to other models found in the scientific literature, the used modelling approach could be applied to develop a more generally valid model, once more plant data is available. The model should then also be tested using data outside its training set.

During model validation, it was revealed that some phenomena, like steel and slag spitting, which are calculated outside the black box sub-model, are not adequately considered in the EAF's energy balance. Despite only having a small impact on the overall balance, this discrepancy could be fixed in future revisions.

Based on additional off-gases and dust measurements, the cooling stack sub-model could be expanded to better represent the complex post combustion and off-gas treatment of the EAF process. An enhanced cooling stack model could be used as a sub-model for the EAF or as a standalone model. It should then be validated in terms of solid and gaseous emissions, since they represent an important factor when comparing different steelmaking routes and assessing their environmental impact. Another future addition to the model could be a sub-model for a scrap preheating chamber, to better represent modern EAFs with heat recouperation technologies.

6 Literature

- [1] World-Steel-Association, World Steel in Figures 2022, <https://worldsteel.org/steel-topics/statistics/world-steel-in-figures-2022/>, 2022.
- [2] J. Kim, B.K. Sovacool, M. Bazilian, S. Griffiths, J. Lee, M. Yang, J. Lee, Decarbonizing the iron and steel industry: A systematic review of sociotechnical systems, technological innovations, and policy options, *Energy Research & Social Science*, 89 (2022) 102565.
- [3] A. Piemonti, A. Conforti, L. Cominoli, A. Luciano, G. Plizzari, S. Sorlini, Exploring the Potential for Steel Slags Valorisation in an Industrial Symbiosis Perspective at Meso-scale Level, *Waste and Biomass Valorization*, (2022) 1-21.
- [4] M. Anderl, S. Haider, M. Purzner, e. al., Nahzeitprognose der Österreichischen Treibhausgas-Emissionen für 2021 in, Umweltbundesamt GmbH, Wien, 2022, pp. 19.
- [5] European Commission, Directorate-General for Research Innovation, Europe's 2030 climate and energy targets : research & innovation actions, Publications Office, 2021.
- [6] World-Steel-Association, Life Cycle Inventory study report 2020 <https://worldsteel.org/publications/bookshop/life-cycle-inventory-study-report-2020-data-release/>, 2022.
- [7] J. Nühlen, M. Hiebel, Technische, ökonomische, ökologische und gesellschaftliche Faktoren von Stahlschrott, (2016).
- [8] A. Reimann, T. Hay, T. Echterhof, M. Kirschen, H. Pfeifer, Application and Evaluation of Mathematical Models for Prediction of the Electric Energy Demand Using Plant Data of Five Industrial-Size EAFs, *Metals*, 11 (2021) 1348.
- [9] T. Hay, V.-V. Visuri, M. Aula, T. Echterhof, A Review of Mathematical Process Models for the Electric Arc Furnace Process, *steel research international*, 92 (2020).
- [10] O. Almpanis-Lekkas, Model development of metallurgical unit operations for use in a process simulation tool. 2015.
- [11] A. Spanlang, Modelling of the blast furnace route in gPROMS. Wien, 2015.
- [12] F. Haiböck, Simulation and Balancing of Trace Elements in the Sinter/Blast Furnace Process Modelling of the blast furnace route in gPROMS. Wien, 2018.
- [13] Y.N. Toulouevski, I.Y. Zinurov, Innovation in electric arc furnaces, Nov. Iorque Springer, (2010).
- [14] J. Madias, Electric Arc Furnace, in: *Ironmaking and Steelmaking Processes*, 2016, pp. 267-281.
- [15] M. Karbowiczek, *Electric Arc Furnace Steelmaking*, CRC Press Book, 2021.
- [16] S. J.L., B. Christian, Eisen und Stahlmetallurgie II Montantuniversität Leoben, Chair of Metallurgy, Austria, 2014.

- [17] S.H. Anderson, Educated use of DRI/HBI improves EAF energy efficiency and yield and downstream operating results, in: 7th European Electric Steelmaking Conference & Expo, AIDM, Venice, 2002.
- [18] H. Pfeifer, M. Kirschen, Thermodynamic analysis of EAF energy efficiency and comparison with a statistical model of electric energy demand, in: 7th European Electric Steelmaking Conference, 2002, pp. 1.
- [19] P.T. Teo, Electric Arc Furnace Slag, Encyclopedia, (2020).
- [20] M. Skaf, J.M. Manso, Á. Aragón, J.A. Fuente-Alonso, V. Ortega-López, EAF slag in asphalt mixes: A brief review of its possible re-use, Resources, Conservation and Recycling, 120 (2017) 176-185.
- [21] M. Dong, Investigation on the PCDD/Fs distribution of quenched off-gas from electric arc furnace, Chemosphere, 272 (2021) 129932.
- [22] T. Havlík, B.V. e Souza, A.M. Bernardes, I.A.H. Schneider, A. Miškuřová, Hydrometallurgical processing of carbon steel EAF dust, Journal of hazardous materials, 135 (2006) 311-318.
- [23] H.J. Odenthal, A. Kemminger, F. Krause, L. Sankowski, N. Uebber, N. Vogl, Review on modeling and simulation of the electric arc furnace (EAF), steel research international, 89 (2018) 1700098.
- [24] S. Srinivas, G. Sethi, Energy efficient Technology packages For electric arc furnace, The Energy and Resources Institute, New Delhi-, 2017.
- [25] L.-z. Yang, R. Zhu, G.-h. Ma, EAF Gas Waste Heat Utilization and Discussion of the Energy Conservation and CO₂ Emissions Reduction, High Temperature Materials and Processes, 35 (2016) 195-200.
- [26] R. Safavi Nick, V. Leinonen, J. Mäyrä, J. Björkvall, Towards Greener Industry: Modelling of Slag Heat Recovery, Metals, 11 (2021) 1144.
- [27] P.J.W.K. de Buzin, N.C. Heck, A.C.F. Vilela, EAF dust: An overview on the influences of physical, chemical and mineral features in its recycling and waste incorporation routes, Journal of materials research and technology, 6 (2017) 194-202.
- [28] J. Cappel, F. Ahrenhold, M.W. Egger, H. Hiebler, J. Schenk, 70 Years of LD-Steelmaking—Quo Vadis?, Metals, 12 (2022).
- [29] A. Wanjari, Methods to optimize energy consumption in Conarc furnaces, SN Applied Sciences, 3 (2021) 1-16.
- [30] J.B. Apfel, Hannes; Winkhold, Achim, The EAF Quantum – New Electric Steelmaking, in: Proc. 8th China International Steel Congress, Primetals Technologies Germany GmbH, 2014.
- [31] P.M. Doran, Bioprocess engineering principles, Elsevier, 1995.

- [32] M. Moskal, P. Migas, M. Karbowniczek, Multi-Parameter Characteristics of Electric Arc Furnace Melting, *Materials (Basel)*, 15 (2022).
- [33] H. Pfeifer, M. Kirschen, J. Simoes, Thermodynamic analysis of EAF electrical energy demand, *EEC*, (2005) 9-11.
- [34] G. Wedler, H.-J. Freund, *Lehrbuch der physikalischen Chemie*, John Wiley & Sons, 2012.
- [35] M. Kirschen, V. Risonarta, H. Pfeifer, Energy efficiency and the influence of gas burners to the energy related carbon dioxide emissions of electric arc furnaces in steel industry, *Energy*, 34 (2009) 1065-1072.
- [36] K. Badr, M. Kirschen, J. Cappel, Chemical energy and bottom stirring systems–cost effective solutions for a better performing EAF, *METEC InSteel-Con*, (2011) 7-10.
- [37] H.-J. Bungartz, S. Zimmer, M. Buchholz, D. Pflüger, *Modellbildung und Simulation: eine anwendungsorientierte Einführung*, Springer-Verlag, 2009.
- [38] A. Friedl, M. Harasek, J. Niel, W. Wukovits, Prozesssimulation, Lecture notes WS 2021/2022, in, TU Wien, Vienna, 2022.
- [39] Siemens Process Systems Engineering, *gPROMS ModelBuilder Guide Release v7.0.9*, in, London, 2021.
- [40] M. Danish, K.B. Ansari, R.A. Aftab, M. Danish, S. Zaidi, Q.T. Trinh, gPROMS-driven modeling and simulation of fixed bed adsorption of heavy metals on a biosorbent: benchmarking and case study, *Environmental Science and Pollution Research*, (2021) 1-16.
- [41] A. Roine, *User manual HSC – Reaction Equations*, Metso Outotec, Pori, 2021.
- [42] L.S. Carlsson, P.B. Samuelsson, P.G. Jönsson, Predicting the electrical energy consumption of electric arc furnaces using statistical modeling, *Metals*, 9 (2019) 959.
- [43] M. Kirschen, K.-M. Zettl, T. Echterhof, H. Pfeifer, Models for EAF energy efficiency, *Steel Times International*, 41 (2017) 44-44.
- [44] S. Tomažič, G. Andonovski, I. Škrjanc, V. Logar, Data-Driven Modelling and Optimization of Energy Consumption in EAF, *Metals*, 12 (2022).
- [45] S. Köhle, Einflussgroessen des elektrischen Energieverbrauchs und des Elektrodenverbrauchs von Lichtbogenöfen, *Stahl und Eisen*, 112 (1992).
- [46] S. Köhle, Recent improvements in modelling energy consumption of electric arc furnaces, in: *Proc. Proc. 7th Europ. Electric Steelmaking Conf.*, Venice, Italy, 2002.
- [47] S. Köhle, B. Kleimt, R. Kühn, S. Zisser, Application of models for electrical energy consumption to improve EAF operation and dynamic control, (2005).
- [48] W. Adams, S. Alameddine, B. Bowman, N. Lugo, S. Paege, P. Stafford, Total energy consumption in arc furnaces, *Metallurgical Plant and Technology International(Germany)*, 25 (2002) 44-50.

- [49] H.-J. Odenthal, An insight into steelmaking processes by Computational Fluid Dynamics, (2017).
- [50] G. Straffelini, A. Gabos, L. Labiscsak, D. Bodino, S. Adinolfi, F. Venturi, Coupled modelling of electric arc furnace and ladle furnace processes, *Ironmaking & Steelmaking*, 37 (2013) 181-186.
- [51] R.D.M. MacRosty, C.L.E. Swartz, Dynamic modeling of an industrial electric arc furnace, *Industrial & engineering chemistry research*, 44 (2005) 8067-8083.
- [52] I. Matino, E. Alcamisi, V. Colla, S. Baragiola, P. Moni, Process modelling and simulation of electric arc furnace steelmaking to allow prognostic evaluations of process environmental and energy impacts, *Matériaux & Techniques*, 104 (2016).
- [53] W. Stahel, *Statistische Regressionsmodelle*, in, 2017.
- [54] I. Pardoe, L. Simon, D. Young, *Applied regression analysis (STAT 462) online course materials*, in, Pennsylvania State University, 2018.
- [55] P. Cohen, S.G. West, L.S. Aiken, *Applied multiple regression/correlation analysis for the behavioral sciences*, Psychology press, 2014.
- [56] L.E. Eberly, Multiple linear regression, *Topics in Biostatistics*, (2007) 165-187.
- [57] M.L. Orlov, *Multiple linear regression analysis using Microsoft Excel*, Chemistry Department, (1996).
- [58] J.W. Osborne, E. Waters, Four assumptions of multiple regression that researchers should always test, *Practical assessment, research, and evaluation*, 8 (2002) 2.
- [59] O. Almpanis-Lekkas, B. Weiss, W. Wukovits, Modelling of an ironmaking melter gasifier unit operation with multicomponent/multiphase equilibrium calculations, *Journal of Cleaner Production*, 111 (2016) 161-171.
- [60] E. Turkdogan, R. Fruehan, *Fundamentals of iron and steelmaking, The Making, Shaping and Treating of Steel, Steelmaking and Refining Volume*, 11th ed., RJ Fruehan, ed., AISE Steel Foundation, Pittsburgh, 11 (1998) 125-126.
- [61] D.S. Newsome, The water-gas shift reaction, *Catalysis Reviews Science and Engineering*, 21 (1980) 275-318.
- [62] K. Haapala, A. Catalina, M. Johnson, J. Sutherland, Development and Application of Models for Steelmaking and Casting Environmental Performance, *Journal of Manufacturing Science and Engineering*, 134 (2012) 051013.
- [63] JetBrains s.r.o; PyCharm 2022.2, <https://www.jetbrains.com/pycharm/> „ 2022.
- [64] T. Meier, K. Gandt, T. Echterhof, H. Pfeifer, Modeling and Simulation of the Off-gas in an Electric Arc Furnace, *Metallurgical and Materials Transactions B*, 48 (2017) 3329-3344.
- [65] M. Kirschen, *Energieeffizienz und Emissionen der Lichtbogenöfen in der Stahlindustrie*, Verlag Stahleisen, Düsseldorf, 2007.

List of Figures

Figure 1: Global crude steel output in million tons (left). Global share of steelmaking routes for crude steel production in 2021 (right)[1].	1
Figure 2: Schematic illustration of a conventional EAF [9].	4
Figure 3: Stages of the EAF batch process [23].	10
Figure 4: Technological development in the EAF sector [24].	12
Figure 5: Quantum EAF(left) [13] and Conarc EAF (right) [28].	14
Figure 6: Typical mass balance for a 100t-EAF using 100% scrap input [18].	15
Figure 7: System boundaries for EAF energy balances: transformer (1); secondary circuit (2); graphite electrodes (3); electric arcs (4); freeboard zone (5); metal bath (6); off-gas elbow (7); gas duct (8); heat exchanger for scrap preheating (9) [13].	17
Figure 8: Different flowsheeting simulation software and their classification by solver and time dependency [11, 38].	22
Figure 9: gPROMS ModelBuilder GUI [39].	23
Figure 10: Variable Types declared in gPROMS ModelBuilder [39].	24
Figure 11: Material connection type from the gPROMS ModelBuilder [39].	24
Figure 12: The gPROMS language tab [39].	25
Figure 13: Look-up table for enthalpies of formation.	26
Figure 14: The process entity [39].	26
Figure 15: Reaction Equations Module of HSC chemistry [41].	27
Figure 16: Parameters influencing the electrical energy demand of an EAF [43].	29
Figure 17: CFD simulation of a 120 t AC EAF, showing velocity and temperature distributions [23, 49].	31
Figure 18: Schematic of EAF model using four zones. For the slag and gas zone, equilibrium conditions are assumed [51].	32
Figure 19: Basic flowsheet including sources and sinks of the EAF process model.	38
Figure 20: Top layer topology of the Electric Arc Furnace model, simplified.	39
Figure 21: Measured EE demand from the industry data vs. EE demand results of the Köhle model for the Conarc, Quantum and conventional EAF; Energy loss is set to 0; R2= 0.83, RSE= 53.9 kWh/t; the black line represents a perfect fit.	57
Figure 22: Measured EE demand from the industry data vs. EE demand results of the Köhle model for the Conarc, Quantum and conventional EAF; Energy loss is set to 100 kWh/t;	

furnace factors Conarc=0.1, Quantum = 0, Conventional = 1; R2= 0.96, RSE = 25.2 kWh/t.
 58

Figure 23: Measured EE demand from the industry data vs. EE demand results of MLR model 1 for the Conarc, Quantum and conventional EAF, using the same descriptors as the Köhle model; Energy loss is set to 0; R2= 0.97, RSE= 22.9 kWh/t. 59

Figure 24: Histogram of the residuals for MLR model 1. The orange curve illustrates an ideal normal distribution. 61

Figure 25: Scatter plot of the residuals for MLR model 1. 61

Figure 26: Measured EE demand from the industry data vs. EE demand results of MLR model 2 for Conarc, Quantum and conventional EAF; no energy loss; R2= 0.97, RSE = 20.0 kWh/t. 62

Figure 27: Histogram of the residuals for MLR model 3. The orange curve illustrates an ideal normal distribution. 63

Figure 28: Scatter plot of the residuals for Model 2. 63

Figure 29: Clusters of the different EAF types, measured EE demand from the industry data vs. simulation results of MLR model 2 for the Conarc, Quantum and conventional EAF. 64

Figure 30: Comparison of the measured average EE demand from the industry data and the average EE demand calculated by the MLR models for the Conarc, Quantum and conventional EAF. Error bars show the regression standard error. 65

Figure 31: Deviation of the calculated and measured average EE demand for each furnace type (right). 66

Figure 32: Solid inputs for case 1. New EAF process model (green) compared to the provided ref. model (blue). Ferrous inputs are calculated based on a set steel production. Other inputs are set to target values. 69

Figure 33: Gaseous inputs for case 1. New EAF process model (green) compared to the provided ref. model (blue). All values set. 69

Figure 34: Solid by-products for case 1. New EAF process model (green) compared to the ref. model (blue). 70

Figure 35: Steel composition for case 1. New EAF process model (green) compared to the ref. model (blue). Steel temperature is 1620 °C. 71

Figure 36: Slag composition for case 1. New EAF process model (green) compared to the ref. model (blue). Slag temperature is 1600 °C. 71

Figure 37: Off-gas volume flow (left) and composition (right) at the off-gas elbow for case 1. New EAF process model (green) compared to the ref. model (blue). Water-gas shift disabled.	72
Figure 38 Off-gas composition at the off-gas elbow for case 1. New EAF process model without WGSR (green) compared to new model with WGSR (green).	72
Figure 39: Energy inputs for case 1. New EAF process model (green) compared to the ref. model (blue). Electric energy demand is calculated based on a set heat loss.	74
Figure 40: Energy outputs (left) and total energy in- and outputs (right) for case 1. New EAF process model (green) compared to the ref. model (blue); The heat loss is set to the value provided in the ref. model.	74
Figure 41: Simulation results of the energy flows for case 1. System boundary is the black box model. Outputs include sensible heat only.	75
Figure 42: Ferrous (left) and other solid inputs (right) for case 2. New EAF process model (green) compared to the ref. model (blue). Scrap and DRI inputs(left) are calculated based on a set steel production. Other values are set.	76
Figure 43: Specific gaseous inputs (left) and solid by-products (right) for case 2. New EAF process model (green) compared to the ref. model (blue). Input parameters are set and output parameter are calculated.	76
Figure 44: Steel composition for case 2. New EAF process model (green) compared to the ref. model (blue). Steel temperature is 1620 °C.	77
Figure 45: Slag composition for case 2. New EAF process model (green) compared to the ref. model (blue). Slag temperature is 1600 °C.	77
Figure 46: Off-gas volume flow (left) and composition (right) at the off-gas elbow for case 2. New EAF process model (green) compared to the results of the ref. model (blue). WGSR disabled.	78
Figure 47: Off-gas composition at the off-gas elbow for case 2. New EAF process model without WGSR (green) compared to new model with WGSR (green).	78
Figure 48: Energy inputs for case 2. New EAF process model (green) compared to the ref. model (blue). The electric energy demand is calculated based on a set heat loss.	79
Figure 49: Energy outputs for case 2. New EAF process model (green) compared to the ref. model (blue). The heat loss is set to the value provided in the ref. model.	79
Figure 50: Total energy in- and outputs for case 2. New EAF process model (green) compared to the ref. model (blue).	80

Figure 51: Simulation results of the energy flows for case 2. System boundary is the black box model. Outputs include sensible heat only. 81

Figure 52: Scrap input (left) and solid by-products (right) for the avg. heat. New EAF process model (green) compared to the provided plant data (blue). 84

Figure 53: Steel composition simulation for the avg. heat. New EAF process model (green) compared to the provided plant data (blue). Steel temperature is 1613 °C. 85

Figure 54: Slag composition simulation results for the avg. heat. New EAF process model (green) compared to the provided plant data (blue). Slag temperature is 1600 °C. 85

Figure 55: Off-gas composition for the avg. heat. Simulation results of the new EAF process model as calculated at the off-gas elbow (left). Comparison of the calculation results for dry off-gas to ranges from the scientific literature [13](right). Water-gas-shift enabled. 86

Figure 56: Comparison of the chemical, electrical and total energy inputs for the avg. heat. Simulation results of the new EAF process model (green) compared to the plant data (blue). The total input of the plant data represents 100%. 88

Figure 57: Simulation results of the energy flows for the avg. heat. System boundary is the black box model. Outputs include sensible heat only. 89

Figure 58: Scrap input (left) and solid by-products (right) for the individual heats. Simulation results (green) compared to the plant data (left, blue) and reference values (right, blue). 90

Figure 59: Steel composition for the individual heats. Simulation results of the new EAF process model. Steel temperature is between 1598 and 1649 °C. 91

Figure 60: Deviations for the steel composition. EAF process model vs. plant data. 91

Figure 61: Slag composition for the individual heats. Simulation results of the new EAF process model. Slag temperature is 1600 °C. 91

Figure 62: Deviations for the slag composition. EAF process model vs. plant data. 92

Figure 63: Composition for dry off-gas at the off-gas elbow for the individual heats. Simulation results of the new EAF process model with water-gas shift enabled (green). Literature range for comparison (blue). Off-gas temperature is 1600 °C. 92

Figure 64: Chemical, electrical and total inputs energy inputs for Heat 1 (left), 2 (right) and 3 (down). Simulation results of the new EAF process model (green) compared to the plant data (blue). The total input of the plant data represents 100%. 93

List of Tables

Tab. 1: EAF process input materials.....	6
Tab. 2: Typical terms considered in the EAF energy balance (kWh)	17
Tab. 3: Statistic Parameters for the ANOVA of the linear Regression for the regression mode. n represents the size of the sample and k the number of predictor variables, y_i is the observed value for i , \hat{y}_i is the predicted value for i , and \bar{y}_i the mean value [56].....	37
Tab. 4: Inlet flow calculation criteria of the EAF model. The formulas for the criteria can be found in Tab. 7 and Eq. (31) [10].	42
Tab. 5: Calculation procedure for the elemental assignment and distribution [10].....	43
Tab. 6: Elemental assignment for the Black Box [10].....	43
Tab. 7: Distributions and compositions specifications for of the black box model [10]..	44
Tab. 8: Distribution correlations used in the case selector [10].	45
Tab. 9: Reactions calculated separately for the model validation and their specific reaction enthalpies.	49
Tab. 10: Terms for the validation of the energy balance as calculated by the black box model. $m_{i,j}$ represents the mass flow, t_{ttt} is the tap-to-tap time and $c_{i,j}$ the mass fraction of the component i in the stream j	50
Tab. 11: Dust oxidation reaction considered in the cooling stack model.....	51
Tab. 12: Statistical sub-model GUI input parameters.	52
Tab. 13: Input parameter description for the statistical submodel. m_j is the mass input through port j in t , c_i is the mass fraction of i in the input stream. w_{GPC} is the mass fraction of natural gas used for post combustion burners.....	53
Tab. 14: Initialisation procedure of the EAF process model [10].....	54
Tab. 15: ANOVA results for MLR model 1.	60
Tab. 16: Regression results of MLR model 1.....	60
Tab. 17: Regression coefficients from MLR model 1 compared to the Köhle model.	60
Tab. 18: Selection of Key Input Variables for MLR model 2.....	62
Tab. 19: ANOVA results for MLR model 2.	62
Tab. 20: Regression results of MLR model 2.....	63
Tab. 21: Regression coefficients from MLR model 2 compared to the Köhle model.	63
Tab. 22: Comparison of results for the prediction models.....	65
Tab. 23: Provided specifications of the EAF used in the validation.....	67
Tab. 24: Ferrous input materials for case 1 and 2 of the validation.....	67

Tab. 25: Input parameters of the EAF process model used for the validation.	68
Tab. 26: Output parameters of the EAF process model used for the validation. The simulation results were compared to the target values from the ref. model.....	68
Tab. 27: Provided specifications of the Industrial EAF [30]......	83
Tab. 28: Input parameters for the model validation using plant data.	83
Tab. 29: Output parameters of the plant data and the process model.	83
Tab. 30: Comparison of the average element distributions between the steel and slag phase for the validation using plant data and for the validation using metallurgical tools.	86

List of Abbreviations and Symbols

Abbreviations

Ac	Slag acidity
AC.....	Alternating current
B.....	Slag basicity
BF	Blast furnace
BOF.....	Basic oxygen furnace
CFD.....	Computational fluid dynamics
DC.....	Direct current
DRI.....	Direct reduced iron
EAF	Electric arc furnace
EE	Electric energy
GPI	Granulated pig iron
gPROMS.....	General process modelling system
GUI.....	Graphical user interface
HBI.....	Hot briquetted iron
HBI.....	Hot briquetted iron
MLR.....	Multiple linear regression
PCD.....	Post combustion degree
PSE.....	Process system enterprise
Ref.....	Reference

VOD	Vacuum oxygen decarburisation
WGSR.....	Water-gas shift reaction
MW	Molecular weight
Statistics	
ANOVA	Analysis of variance
FDIST	F-distribution function
MS	Mean square
R ²	Coefficient of determination
RSE	Regression standard error
SS.....	Sum of squared errors
VIF	Variance inflation factor

Symbols and subscripts

$\Delta_f H_{298}^0$	Standard enthalpies of formation [J]
Δh_{sf}	Mass specific enthalpies of slag formation [J/kg]
Δh_{sol}	Mass specific enthalpies of solution [J/kg]
\dot{H}	Enthalpy stream [J/s]
h_T^0	Mass specific enthalpies of formation [J/kg]
\dot{n}	Molar flow [mol/s]
\dot{Q}	Heat flow [J/s]
C_p	Isobaric heat capacity [J/K]
Cr_{Dist}	Chrome distribution [-]
Mn_{Dist}	Manganese distribution [-]
P_{Dist}	Phosphorus distribution [-]
S_{Dist}	Sulphur distribution [-]
e_k	Specific kinetic energy [J/kg]
e_p	Specific potential energy [J/kg]
\dot{m}	Mass flow [kg/s]
\dot{n}	Molar flow [mol/s]
ΔH_{298}^0	Standard enthalpy of reaction [J]
abs%	Absolute percent [%]
c	Mass fraction [-]

E.....	Energy [J]
H.....	Enthalpy [J]
h.....	Specific enthalpy [J/kg]
m.....	Mass [kg]
P.....	Power [J/s]
p.....	Pressure [Pa]
Q.....	Heat energy [J]
T.....	Temperature [K]
t_{ttt}	Tap-to-tap time [min]
U.....	Internal energy [J]
u.....	Specific internal energy [J/kg]
v.....	Specific volume [m ³ /kg]
v%.....	Volume percent [%]
w.....	Mass fraction [-]
W.....	Work [J]
w%.....	Weight percent [%]
λ	Air fuel ratio [-]
v.....	Stoichiometric coefficient [-]